Energy Transfer Processes in Organic and Inorganic Materials for Photovoltaic Devices

Christopher Menelaou

Worcester College

University of Oxford

A thesis submitted for the degree of

Doctor of Philosophy

Trinity 2015

List of Published Papers:

- **Christopher Menelaou**, Jeroen ter Schiphorst, Amol M. Kendhale, Patrick Parkinson, Michael G. Debije, Albertus P. H. J. Schenning, and Laura M. Herz. Rapid Energy Transfer Enabling Control of Emission Polarization in Perylene Bisimide Donor-Acceptor Triads. *The Journal of Physical Chemistry Letters*, 6:1170–1176, 2015.

- Patrick Parkinson, Dmitry V. Kondratuk, **Christopher Menelaou**, Juliane Q. Gong, Harry L. Anderson, and Laura M. Herz. Chromophores in Molecular Nanorings: When Is a Ring a Ring? *The Journal of Physical Chemistry Letters*, 5:4356–4361, 2014.

- **Christopher Menelaou**, Steve Tierney, Nicolas Blouin, William Mitchell, Priti Tiwana, Ian McKerracher, Chennupati Jagadish, Miguel Carrasco, and Laura M. Herz. Effect of Nanocrystalline Domains in Photovoltaic Devices with Benzodithiophene Based Donor-Acceptor Co-Polymers. *The Journal of Physical Chemistry C*, 118:17351–17361, 2014.

- Jeroen ter Schiphorst, Amol M. Kendhale, Michael G. Debije, **Christopher Menelaou**, Laura M. Herz, and Albertus P.H.J. Schenning. Dichroic Perylene Bisimide Triad Displaying Energy Transfer in Switchable Luminescent Solar Concentrators. *Chemistry of Materials*, 26:3876–3878, 2014.

- Michael G. Debije, **Christopher Menelaou**, Laura M. Herz, and Albertus P.H.J. Schenning. Combining Positive and Negative Dichroic Fluorophores for Advanced Light Management in Luminescent Solar Concentrators. *Advanced Optical Materials*, 2:687–693, 2014.

- Giles E. Eperon, Samuel D. Stranks, **Christopher Menelaou**, Michael B. Johnston, Laura M. Herz, and Henry J. Snaith. Formamidinium Lead Trihalide: A Broadly Tunable Perovskite for Efficient Planar Heterojunction Solar Cells. *Energy & Environmental Science*, 7:982–988, 2014.

- Christian T. Weisspfennig, Derek J. Hollman, **Christopher Menelaou**, Sam D. Stranks, Hannah J. Joyce, Michael B. Johnston, Henry J. Snaith, and Laura M. Herz. Dependence of Dye Regeneration and Charge Collection on the Pore Filling Fraction in Solid State Dye Sensitized Solar Cells. *Advanced Functional Materials*, 24:668–677, 2013.

- Samuel D. Stranks, Giles E. Eperon, Giulia Grancini, **Christopher Menelaou**, Marcelo J.P. Alcocer, Tomas Leijtens, Laura M. Herz, Annamaria Petrozza, and Henry J. Snaith. Electron-Hole Diffusion Lengths Exceeding 1 Micrometer in an Organometal Trihalide Perovskite Absorber. *Science*, 342:341–344, 2013.

Abstract

This thesis is concerned with energy transport processes in a series of low-bandgap copolymers, solution processable hybrid organic-inorganic perovskite materials, and donor-acceptor triad dyes which are used in photovoltaic cells and solar concentrator devices. These processes are investigated using time-resolved photoluminescence (PL) spectroscopy techniques which allow the investigation of transport processes with sub-ps time resolution.

Two donor-acceptor-donor triad dyes composed of perylene bisimide units are compared, and rapid energy transfer ($< 2\,\mathrm{ps}$) from the donor to a central bay-substituted PBI unit is observed in both molecules. For the linear molecule, in which the transition dipole moments corresponding to the lowest singly excited state are all aligned along the molecule long-axis, such rapid energy transfer is shown to be consistent with predictions of a modified Förster model which takes into account both the delocalisation of the excitation and the short donor-acceptor separation. When the dipole moments of the donor units are perpendicular to that of the central acceptor however, this model is found to strongly underestimate the energy transfer. The energy transfer is found to arise due to a combination of both through-space (Förster type) and through-bond energy transfer, the latter of which is mediated by molecular torsions which break orthogonality and enable conjugation between the two units. This rapid energy transfer also coincides with either retention or rotation of polarisation between absorption and emission. These dyes are therefore shown to be promising candidates for use in luminescent solar concentrators (LSC), as rapid intramolecular energy transfer and control of the emission polarisation are two features which can help to reduce self-absorption and escape losses in LSC devices.

The effect of chemical structure on the morphology, energy transport properties and overall photovoltaic device efficiency is determined for a series of low-bandgap polymers comprising benzodithiophene donor and benzothiadiazole acceptor units. Photovoltaic devices incorporating polymer:fullerene blends are found to yield devices with power conversion efficiencies of up to 6%, with the highest PCE observed in devices which form films exhibiting a very low degree of crystallinity in X-ray diffraction patterns and a corresponding low surface roughness in thin films.

The influence of crystallite formation on energy transport is probed by time resolved PL quenching of polymer films on a TiO_2 quenching layer. Exciton diffusion lengths in these films are standard for low-bandgap polymers, ranging from 4 to 7.5 nm. The diffusion length is found to be higher in films with a higher degree of crystallinity, however direct PL quenching measurements on polymer:PCBM films show however that the vast majority of generated excitons are found to reach an interface and dissociate within 1 ps, showing that exciton diffusion does not present a bottle-neck for device efficiencies. From these observations it is concluded that the boundaries between crystalline and amorphous domains may impede charge extraction at the charge densities found during photovoltaic operation.

Finally, the distance over which electron-hole pairs can diffuse before decay or trapping is investigated in two organic-inorganic hybrid perovskite structures ($CH_3NH_3PbI_{3-x}Cl_x$) by monitoring the rate and degree of PL quenching in the presence of either an electron or hole acceptor material. The diffusion lengths observed in these materials are on the order of 100 nm for the triiodide perovskite ($x = 0$), and over 1 µm in the mixed halide material ($x > 0$). These diffusion lengths are extremely long compared with those observed in other solution processable materials and explain the very high power conversion efficiencies that have been reported in photovoltaic cells containing these and similar perovskite materials. The longer diffusion lengths in particular correlate with good power conversion efficiency when a planar device geometry is used. Similar cells using the triiodide material however show poor efficiencies, attributed to the smaller diffusion length in this material. Application of the PL quenching technique to determine diffusion lengths is therefore shown to be a useful and simple method by which the suitability of a given perovskite material for use in a planar PV cell can be determined.

Acknowledgements

I am deeply grateful to Prof. Laura Herz for providing me the opportunity to undertake this research as part of her group, and for the invaluable support, advice and encouragement over the last four years. I'm very grateful also to the past and present students of the group, in particular Dr. Patrick Parkinson and Dr. Chaw Keong Yong for training me up in the use of the laser system, and for discussions and advice on many occasions since, and to the other students in the group for making the department such a great atmosphere to work in.

The experiments detailed in this thesis would not have be possible were it not for the help from other students and researchers both in Oxford and from further afield. I would like to thank Merck Chemicals and my industrial supervisor Dr. Miguel Carrasco-Orozco for providing the polymers studied in Chapter 5, for sponsorship as part of the Industrial CASE Studentship with the EPSRC, and for the opportunity to present my work at the CASE student conference each year. I'd like to thank Dr. Sam Stranks and Giles Eperon for the perovskite samples and data that were used modelled in Chapter 6, Dr. Ian McKerracher from the Australian National University for kindly providing the sputtered thin films used in Chapter 5, and our collaborators from the Eindhoven University of Technology, Jeroen ter Schiphorst, Dr. Michael Debije and Prof. Albertus Schenning for providing the materials studied in Chapter 4 and for several informative discussions.

Lastly I'd also like to thank my parents, brother, and grandparents for their support over the years I've spent in Oxford, and my friends from both my time here at University and back home.

Contents

Chapter 1

Introduction

Placing a larger emphasis on renewable sources as part of total global energy production is an effective way of reducing exposure to volatile prices of oil and other fossil fuels, and will play an increasingly important role in meeting the target of limiting the rise in global average temperatures to 2°C as agreed in the United Nations Framework Convention on Climate Change.[217] Of all available renewable energy sources, solar energy stands out as one of the most promising when considering that the total solar energy incident on the Earth's surface is approximately 885 million TWh annually.[3] This is an amount far in excess of the $\sim$ 10.4 TWh of energy used globally in 2012.[106]

Although the total global solar capacity exceeded 150 GW in early 2014, solar energy only contributes a very small fraction to total global energy production. This is in part due to the prohibitively high cost of solar energy as compared to other energy sources; grid parity was reached in several countries in 2013 but further work in developing and refining new and current technology is needed to reduce the cost of solar energy globally.[3]

Since the development of the first silicon solar cell at Bell labs in 1954,[41] the power conversion efficiency (PCE) of silicon-PV devices has increased from the 6% initially reported to over 25%,[86] and a number of alternative materials and structures for solar energy conversion have been reported. These can generally be categorised as either silicon-wafer based "first generation" cells; thin-film inorganic "second generation" PV using amorphous silicon, CdTe or CIGS; or "third generation" cells incorporating organic molecules. This latter category includes dye sensitised solar cells (DSSC, including both solid hole transporters and liquid electrolytes), all-organic small molecule or polymer solar cells, and perovskite cells. Despite the wide range of technologies available the vast majority of PVs in use are silicon based, accounting

for 90% of all PV modules.[78]

The third generation solar cells, in particular organic photovoltaics, have many attractive features compared to first or second generation inorganic cells as they are solution processable and can therefore be prepared at low-temperature by continuous printing processes. In addition, these devices have the potential to be flexible or semi-transparent, easily scalable, and can offer significant cost-savings as compared to first or second generation cells.[28;122]

All organic polymer-fullerene devices have increased steadily in efficiency[86] since the development of the bulk-heterojunction,[240] as the primary excitation in these devices is an exciton which is relatively strongly bound and requires transfer of the electron to a second material in order to promote dissociation into free charges.[29]

A relatively new solar cell device, the perovskite solar cell, was first introduced in 2009 as a variation on DSSC[121] but has become a separate class of solar cell with reported power conversion efficiencies increasing rapidly from the originally reported 3.8% to over 20%.[86] Device architectures for efficient PV are not limited to those containing a mesoporous metal-oxide scaffold, as in DSSC, or the BHJ as in polymer-fullerene cells, as evidenced by a 15.4% PCE in planar cells prepared by vacuum deposition.[143] One of the reasons for this high performance is the exceptionally long distances over which energy transport occurs in films of perovskite material as is discussed in Chapter 6.

Aside from developing low-cost PV devices based on solution processable materials, another route toward cost effective solar power is to reduce the required active area of a photovoltaic device. This can be achieved through the use of solar concentrators to focus incident sunlight onto a small area but high-quality cell. Optical concentrators using mirrors or lenses can reduce the amount of PV material required by focussing a large amount of sunlight onto a small area cell, and active tracking mechanisms can be used to ensure continuous energy generation. The major disadvantage of these devices are that active tracking components constitute a large portion (approx. 60-70%) of the total (concentrator + PV cell) device cost.[70;78] Additionally, they are unable to function well in diffuse light conditions.

One technology which is able to circumvent these issues is the luminescent solar concentrator (LSC).[227] This device consists of organic dyes or inorganic luminescent species embedded in a transparent waveguide. Emission from the embedded dyes occurs with high quantum yield and is transmitted to the edges of the waveguide

by total internal reflection. Although the edge to surface ratio of LSC devices can be very high, the concentration factors such ratios should provide are not often realised.[55] Two major loss sources in LSC devices are self-absorption by the embedded luminophore,[55] and escape losses from the surface of the waveguide, both of which can be reduced by energy transfer from the absorber to a lower energy emitter with control of the polarisation.

All of the above mentioned energy transport processes occur on time scales ranging from ultra-fast (sub-picosecond) to several hundred nanoseconds and are investigated in this thesis by time resolved photoluminescence measurements with short time resolution.

Chapter 2 gives a brief overview of the background theory relevant to the later chapters in this thesis. As the main theme of the thesis is on energy transfer in materials for use in third generation photovoltaic devices, a discussion of the basic excitations in organic semiconductor materials is given. The optical spectra of small molecules and polymers are discussed as absorption and fluorescence spectroscopy are some of the most commonly used methods of probing excited state properties of conjugated organic materials and are the main techniques used in this thesis. The exciton model developed by Kasha[112] is discussed to describe intermolecular interactions between single small molecules and polymers, and is extended to bulk disordered systems. A description of the evolution of excited state species (excitons) following excitation of bulk organics is given, including the mechanisms of energy transfer in the case of weak intermolecular-coupling. The operation mechanism and methods of optimising materials for use in organic photovoltaics is also described in this chapter.

In Chapter 3 the experimental techniques used to probe energy transfer in the later chapters are discussed. A description of the time correlated single photon counting (TCSPC) and photoluminescence upconversion (PLUC) techniques is given, along with a summary of the techniques used to generate ultra-short pulsed radiation which is crucial for time resolved photoluminescence measurements. Experimental details of the apparatus, along with a description of the system calibration method and data analysis techniques conclude this chapter.

The experimental results of this thesis constitute Chapters 4 to 6 as follows:
In chapter 4 a discussion is given of energy transfer in two donor-acceptor-donor triads based on perylene bisimides, which show promise for use in LSC. The donor and

acceptor groups are bound together such that the dipole moments, aligned along the long axis of the perylene bisimide units, are either collinear or orthogonal. Following selective excitation of the donor units, rapid and efficient energy transfer and retention (or rotation for the orthogonal trimer) of polarisation is observed on a time scale of $\sim 2\,\mathrm{ps}$. The energy transfer is modelled with a distributed-dipole Förster model which predicts the energy transfer rate for the linearly arranged triad but severely underestimates it for the orthogonal case. The energy transfer is attributed to a combination of through-space transfer through-bond coupling of the donor and acceptor units.

In Chapter 5, a series of five donor-acceptor low bandgap polymers based on benzodithiophene donor and a benzothiadiazole acceptor are compared. Such polymers are of vital importance to OPV devices as the lower band-gap of the materials allows a higher fraction of incident photons to be absorbed, increasing the current that can be produced. The morphology of films of each of the five materials are studied by atomic force microscopy and x-ray scattering, and those polymers which form the most amorphous films with the smallest number of ordered aggregates yield devices with the highest power conversion efficiencies.

The influence of these aggregate domains on PV device operation is probed by time resolved photoluminescence measurements of both the intrinsic exciton diffusion length, and the model used is to determine these diffusion lengths is fully described. The photoluminescence quenching when the polymers are blended with the electron acceptor PCBM is also directly measured. The efficiency of exciton diffusion to, and dissociation at the polymer-fullerene interface is high, occurring within $\sim 1\,\mathrm{ps}$ for all materials in the series. Hence, the presence of crystalline domains is found to hinder the migration of charges to the electrodes.

In Chapter 6, the model described in Chapter 5 is applied to determine the average diffusion length of electrons (holes) in films of methylammonium lead halide perovskites, and the results from films of a triiodide perovskite, $MAPbI_3$, and a mixed halide perovskite, $MAPbCl_xI_{3-x}$ are shown. It was found that the diffusion length of both electrons and holes in the mixed halide were greater than $1\,\mu\mathrm{m}$, and around $100\,\mathrm{nm}$ in the triiodide. These remarkably long diffusion lengths at room temperature explain the high efficiencies that have been observed in photovoltaic devices with these materials as an active layer, even in a planar configuration.

In Chapter 7, the findings from the experimental chapters are summarised and potential avenues for future research are discussed.

Chapter 2

Background Theory

2.1 Excitations in Conjugated Polymers

The vast number of possible molecular structures based on carbon stems from the flexibility of carbon atoms in bonding. The $2s$ and $2p$ orbitals can combine to form hybrid orbitals consisting of the $2s$ and $n = 1$, 2 or 3 of the p orbitals, resulting in $(n + 1)$ equivalent sp^n orbitals, and $(3 - n)$ free p orbitals. The hybrid orbitals on adjacent carbon atoms interact strongly to form orbitals with σ symmetry which define the backbone of the molecule, while the orthogonal p orbitals interact more weakly to form π orbitals around the σ bonds. Molecules containing no π orbitals are referred to as saturated, while unsaturated molecules contain at least one π bond. Conjugated materials are those in which the π system extends over several atoms.

The simplest description of bonding in conjugated molecules is given by the Hückel model,[10] in which the σ and π systems are considered independent of one another, and individual atomic p orbitals interact only with their nearest neighbours to form molecular orbitals which are delocalised over the entire conjugated system. The molecular orbitals are filled pair-wise according to Hund's rule. The lowest energy transition in such a molecule is then the difference between the energies of the highest occupied (HOMO) and lowest unoccupied (LUMO) molecular orbitals. Although this model completely neglects electron-electron interactions and π-electron interactions with the nuclear framework, it is useful for a qualitative description of electronic structure. More accurate ab-initio and semi-empirical methods for calculating electronic structure are described in many quantum chemistry textbooks.[135;211]

Applying the Hückel model to an extended conjugated system of atoms is equivalent to the tight-binding approximation from solid-state physics and predicts a continuous band of energy levels. The simplest conjugated molecule, trans-polyacetylene,

is a linear chain of carbon atoms with one electron in one p-orbital per carbon atom. This system would be expected to be metallic in character, by the Hückel model, with no gap between occupied and vacant energy levels. 1-D metallic systems however are predicted and found to be unstable with respect to a distortion of the lattice, such that the bonds between atoms alternate, one longer, the next shorter than the bonds in the undistorted system. This doubles the repeat length of the lattice and opens up a band gap at $k = \pi/2a$, where a is the undistorted bond length.

Whether the bond length alternation is written as $(-\mathrm{C}{=}\mathrm{C}{-}\mathrm{C}{=}\mathrm{C}{-})_\mathrm{n}$ (A-phase) or $(=\mathrm{C}{-}\mathrm{C}{=}\mathrm{C}{-}\mathrm{C}{=})_\mathrm{n}$ (B-phase) has no effect on the energy of a trans-polyacetylene chain, the configurations are degenerate. Application of the model developed by Su, Schrieffer and Heeger predicts that, as a result of this degeneracy, the lowest energy stable excitation is a localised transition between the two phases, referred to as a soliton (S).[206;205] Both theory and measurements show that for each soliton present there is a single state at the centre of the band gap which can hold (0, 1, or 2) electrons and has charge (+e, 0, -e) and has spin (0, 1/2, 0) depending on the occupancy. These excitations are calculated to span approximately 14 carbon atoms and are mobile due to the low effective mass of $\sim 6m_e$. In general, absorption of a photon by trans-PA results in the promotion of an electron to the conduction band, followed by rapid relaxation to form a charged soliton–anti-soliton pair ($S\overline{S}$), which, in the absence of any electron-electron interactions separate within 10^{-13} s.[94]

Although it was the first material in which conductivity of organic polymers was observed and has been intensively studied as a prototype material, trans-PA exhibits photophysics almost unique to this system; the majority of conjugated polymers which are of interest for use in photovoltaics, including those described in this thesis, do not have a degenerate ground state like trans-PA.[16] In these systems, separated solitons are no longer stable excitations, as increasing separation between $S\overline{S}$ pairs forms long sections of the higher energy phase and increases the overall energy. Instead, polarons, or bound $S\overline{S}$ pairs, are the general excited state species as they create a localised distortion of the lattice without changing the conjugation phase.[25;71] The presence of a polaron results in two states at energy $E = \pm\omega_0$ in the band gap corresponding to the in and out of phase combination of the soliton and anti-soliton states. These states can be filled with 0, 1 2, 3 or 4 electrons.[94] A single electron in the lower level is a positive polaron (cation radical), while the negative polaron (anion radical) has a filled lower level and a single charge in the upper level. Positive and

negative bipolarons are formed when both levels are either empty or full respectively, while a filled lower level is a neutral polaron. The various excitations in conjugated polymers discussed here are summarised graphically in Figure 2.1.

The above description includes interaction between π-electrons and the nuclear positions (the electron-lattice interaction) but completely neglects any interaction between the π-electrons. In general for conjugated polymers this is not a realistic description as the electron-electron interaction strengths are comparable to the electron-lattice interaction,[16] and must be included in order to reproduce features in absorption and luminescence spectra.[177;38;37] When these contributions are included, the primary excitation is found to be an exciton, a bound polaron-pair which has no overall charge.

The exciton binding energy, defined as the difference in energy between an exciton relative to a pair of fully separated polarons,[30] are generally reported to be around 0.3 to 0.6 eV[30;7;49;118], although values ranging from < 0.2 eV[238;161] to 0.9 eV[38] have been reported. The binding energy is much larger than $kT \sim 26$ meV at room temperature and, while direct generation of polarons following photoexcitation[8] has been found to occur with 10–20% efficiency,[156;180] dissociation of excitons without any external stimulus is not observed.[160] This has important consequences for organic photovoltaics as will be discussed in later sections.

2.2 Interaction of Organic Molecules with Light

As discussed above, the generation of excitons, solitons and polarons in organic molecules occurs after photoexcitation of an electron from a bonding π orbital to an antibonding π^* orbital. The energy required is equal to the gap between HOMO and LUMO levels, which for many large organic molecules is between 1 and 4 eV, in the visible range of the electromagnetic spectrum.

When a molecule is exposed to radiation oscillating at frequency ω_{fi}, transitions between the initial ground state, $|i\rangle$, and a final excited state, $|f\rangle$, separated by energy $E_{fi} = E_f - E_i = \hbar\omega_{fi}$ occur at a rate[77]

$$W_{f \leftarrow i} = \frac{2\pi}{\hbar} |\boldsymbol{\mu}_{fi}|^2 E_0^2 \rho(E_{fi}), \tag{2.1}$$

where $\rho_{rad}(E_{fi})$ is the density of final states at the energy E_{fi}, E_0 is the electric field amplitude, and

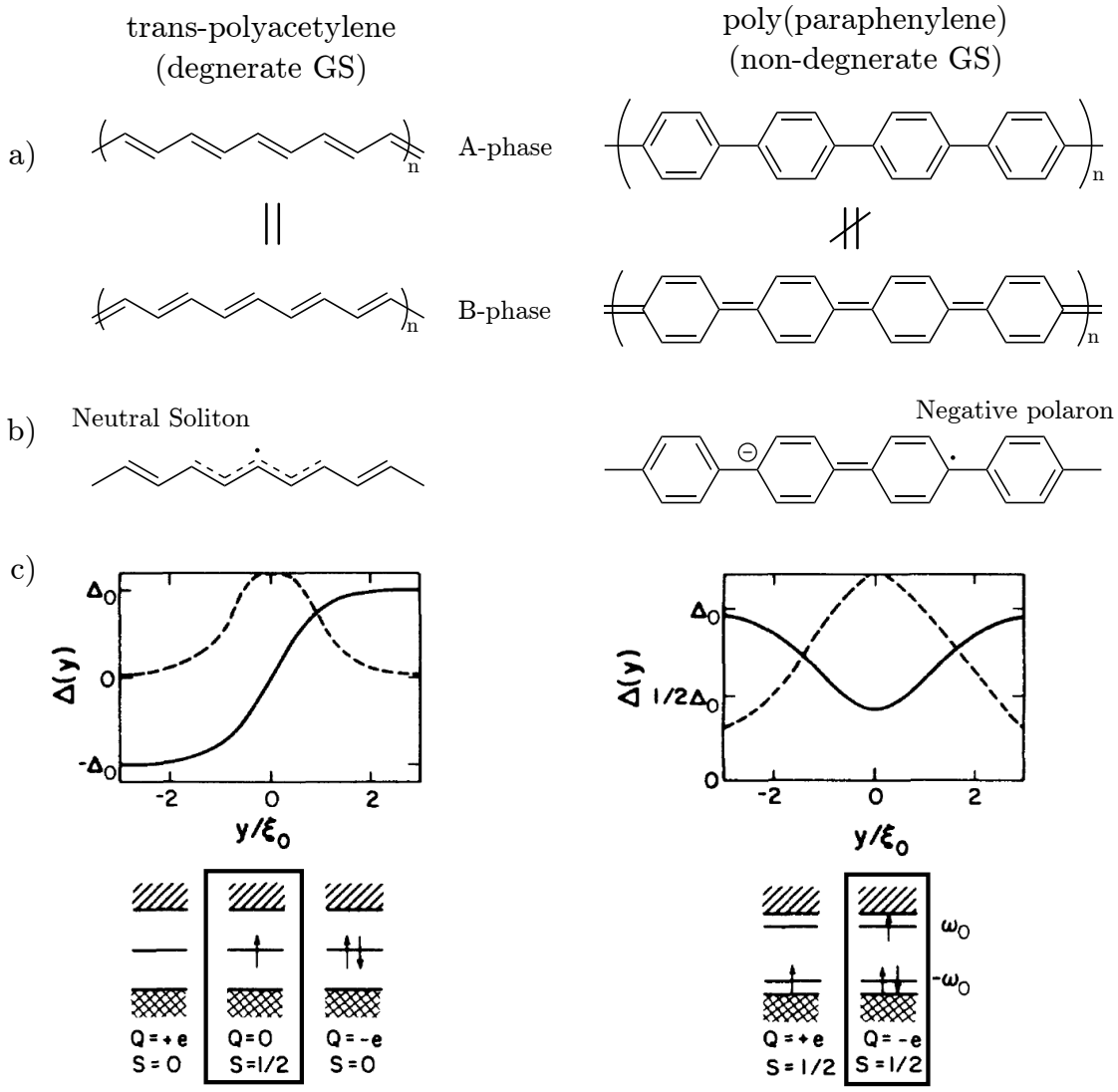

Figure 2.1: Summary of soliton and polaron excitations in trans-polyacetylene, left, and poly(paraphenylene), right. a) The molecular structure of the A-phase and B-phase bond length variations. The A and B phases of trans-PA are identical whereas those of PPP are not. b) Chemical picture of the major excitation (PA - soliton, PPP - polaron) in each material. The soliton results in a phase change from one side to the other whereas the polaron does not. c) Graphs show the lattice displacement (solid line) and electron densities (dashed line), $\Delta(y)$ against position. Band diagrams show the conduction and valence bands, and the relative position of the soliton and polaron energy levels. Q is the total charge and s is the total spin. For each, the configuration corresponding to the diagram in part b) is enclosed in a black box. (Part (c) adapted from: Fesser et al., 1983)

$$|\boldsymbol{\mu}_{fi}|^2 = |\langle f|\,\boldsymbol{\mu}\,|i\rangle|^2 \tag{2.2}$$

is the transition dipole moment for the electron dipole operator $\boldsymbol{\mu}$, which is a function of both the electron and nuclear positions,[10]

$$\boldsymbol{\mu} = -e\sum_i \mathbf{r}_i + e\sum_j \mathbf{R}_j. \tag{2.3}$$

In general the overall wavefunction depends on both the nuclear and electronic degrees of freedom, and calculating the dipole moments is difficult. The calculation can be simplified by means of the Born-Oppenheimer approximation, which states that as a result of the vastly different masses of the electrons and nuclei, the total wavefunction can be split into the product of the electronic and nuclear wavefunctions, and that the the solutions to the electronic part of the Schödinger equation depend parametrically on the nuclear co-ordinates.[16] This difference in mass between nuclei and electrons, and hence the difference in speed between electronic and nuclear transitions also forms the basis of the Frank-Condon principle, which is used to describe vibronic transitions in optical spectroscopy.

2.2.1 Franck-Condon Principle

The time scale for the electronic transition $f \leftarrow i$ is on the order of 10^{-15} s while nuclear motions occur on the order of 10^{-13} s (e.g. a C−C stretching mode). The electronic transition will therefore take place without any significant change in the position of the nuclei, and only once the electrons have settled in the final distribution will the nuclei adjust to the new field. Since the transition involves removing an electron from a π bonding orbital and adding it to an antibonding π^* orbital, the equilibrium geometry of the upper state will be different to that of the ground state. The rapid shift from ground state to excited state therefore ends with the nuclei in positions corresponding to a vibrationally excited mode. This is described graphically in Figure 2.2.

Mathematically, the effect of the widely differing time scales for electronic and nuclear motion allows for separation of the overall wavefunction into the product of the electronic (ϵ) and vibrational (ν) wavefunctions:

$$|\psi_i(\mathbf{r},\mathbf{R})\rangle \approx |\epsilon_i(\mathbf{r})\rangle\,|\nu_i(\mathbf{R})\rangle \tag{2.4}$$

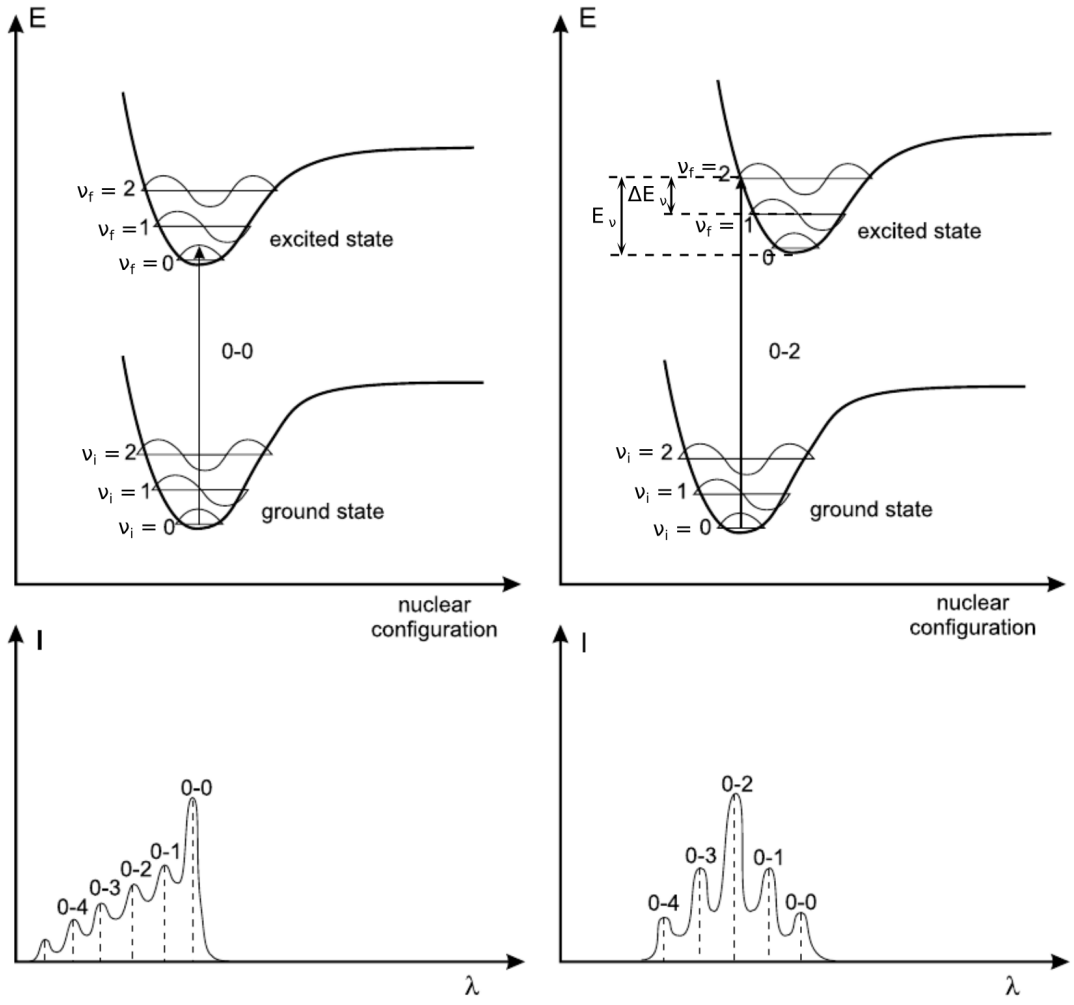

Figure 2.2: Pictorial description of the Franck-Condon principle. The top two plots show total system energy against nuclear coordinate for a system with identical equilibrium geometry in the ground and excited state (Left hand side), and one with different geometry (Right hand side). The bottom two plots show the absorption spectra for the two systems. When the excited state and ground state equilibrium geometries are the same, the 0-0 transition is the strongest, whereas when the geometries are offset, excitation into a higher vibrational state is favoured. Adapted from: Valeur and Berberan-Santos, 2012

The transition dipole moment then reduces to the product of the electronic transition dipole moment and the vibrational wavefunction overlap, with nuclear position equal to the ground state equilibrium geometry $\mathbf{R}_0$,

$$\langle\psi_f|\,\boldsymbol{\mu}\,|\psi_i\rangle \approx \langle\epsilon_i(\mathbf{r};\mathbf{R}_0)|\,\boldsymbol{\mu}_\mathbf{e}\,|\epsilon_i(\mathbf{r};\mathbf{R}_0)\rangle\,\langle\nu_f(\mathbf{R}_0)|\nu_i(\mathbf{R}_0)\rangle\,. \tag{2.5}$$

Although the plots of energy against nuclear co-ordinates in Figure 2.2 show only the 0-0 and 0-2 transitions for equal and unequal ground and excited state geometries, the value of the vibrational wavefunction overlap is non-zero for several 0-n combinations, leading to the progression plotted in the lower plots. The square of the overlap $|\,\langle 0|\nu\rangle\,|^2$ is referred to as the Franck-Condon factor and is parametrised by the Huang-Rhys parameter, such that

$$F_{FC} = |\,\langle 0|\nu\rangle\,|^2 = \frac{S^\nu}{\mathrm{e}^S\nu!}, \tag{2.6}$$

S can be determined experimentally by taking the ratio of the 0-0 and 0-1 transition peak intensities and describes the average excess vibrational energy given to the molecule,

$$E_\nu = S\Delta E_\nu = (\nu + 1/2)\Delta E_\nu, \tag{2.7}$$

where E_ν and ΔE_ν are the excess energy and energy separation between vibrational levels are as described in Figure 2.2. A parameter of $S = 0$ corresponds to a pure 0-0 transition while non-zero values lead to a peak progression.

2.2.2 Excited State Processes

Following excitation, rapid relaxation to the $\nu = 0$ level of the lowest singlet excited state occurs on a time scale of picoseconds. In an isolated molecule, there are three possible mechanisms for decay from this state, either by radiative decay back down to the ground state (fluorescence), non-radiative decay to the ground state by direct coupling of the two states (internal conversion, IC), or conversion from a singlet exciton a triplet exciton (intersystem crossing, ISC). These processes are summarised in the Jablonski diagram (Figure 2.3). Additional processes reducing the populations of the S_1 state in real systems are energy or charge transfer to a neighbouring molecule. These will be discussed in later sections.

For many conjugated molecules internal conversion is inefficient because the energy gap between the ground and excited states is large. Fluorescence is the major decay route when emission from the lowest singlet excited state is allowed according to the

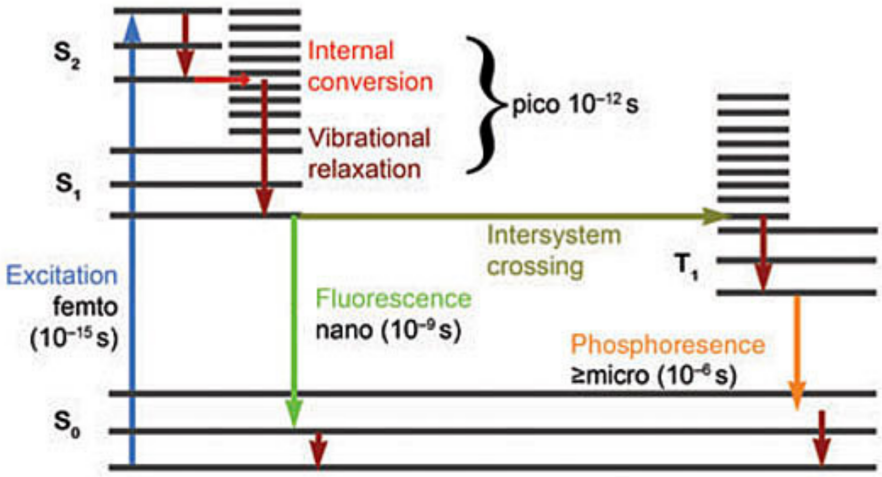

Figure 2.3: The Jablonski diagram – each block of multiple lines represents an electronic state, and the lines within each band are the associated vibrational states. Those on the left hand side are the singlet states, and those on the right are the triplet states. In this diagram, a representation of a single molecule being excited to the second singlet state S_2 is shown, followed by rapid internal conversion to the lowest vibrational level of the S_1 state. From here, arrows showing fluorescence, internal conversion, and intersystem crossing are shown. The average times that each step takes are included in this figure. (Taken from: Lichtman and Conchello, 2005)

selection rules. This is the case for many phenyl-containing polymers which are useful in electroluminescent and photovoltaic devices, a typical example of which is MEH-PPV.[33] (cf. PA discussed in section 2.1 which does not fluoresce as the lowest state has $2^1A_g^+$ symmetry which is not accessible by radiative transitions, in contrast to the $1^1B_u^-$ state which is the lowest excited state in phenyl-based polymers.[16]).

The third decay pathway is by conversion from the lowest lying singlet (S_1) state to the lowest lying triplet (T_1) state. This process occurs most efficiently in materials containing heavy atoms, as the rate of the ISC process is proportional to the fourth power of the atomic number. Triplet excitations can then decay by phosphorescence, a radiative decay process which occurs on a time scale of micro- to milli-seconds as emission from triplet states is spin-forbidden. The reverse ISC process in which singlet excitons are regained is a thermally activated process and leads to delayed fluorescence. Singlet excitons can also be regained as a product of triplet-triplet annihilation. These processes are not included in Figure 2.3 and are not observed within the time scales and excitation densities of the experiments reported in this thesis.

2.3 Factors Affecting Absorption and Photoluminescence Spectra

2.3.1 Stokes Shift and Solvent Relaxation

Stokes Shift

In a fully conjugated, isolated molecule, the energy of the 0-0 transition will be identical in energy whether photons are absorbed or emitted, and the 0-0 peaks in the absorption and fluorescence spectrum would be expected to overlap. When the Huang-Rhys parameter $S < 1$, this will lead to a zero Stokes shift, that is, the difference in energy between the band maximum in absorption and fluorescence is zero. In real systems however, various mechanisms exist which drive the two apart and increase the overall Stokes shift.

Solvent Relaxation

If a molecule is well dissolved in a polar solvent then before excitation the solvent molecules are arranged to minimise the overall energy of the system. This has the effect of lowering the energy of the ground state relative to the same but isolated molecule. When excitation occurs, the electron distribution is different to that of the ground state, and so the energy of the S_1 state is destabilised. The solvent molecules react by re-organising over $\sim 100\,\text{ps}$ to stabilise the excited state,[126] in turn destabilising the ground state. When fluorescence occurs, now from the excited state equilibrium geometry, emission is at a lower energy than absorption as the gap between the two levels has decreased. This is summarised in Figure 2.4. If fluorescence measurements are taken with high enough temporal resolution, the shift in emission wavelength can be observed.

2.3.2 Effective Conjugation Length

For small conjugated molecules and oligomers in which the entire molecule is fully conjugated, the excitation energy scales linearly with the inverse number of repeat units, $1/N$. For molecules with more than a certain number of units the decrease in excitation energy reaches a limit corresponding to the effective conjugation length. This has been measured to be between 7 and 20 units[152] and varies depending on the structure of the polymer. The effective conjugation length is a combination of

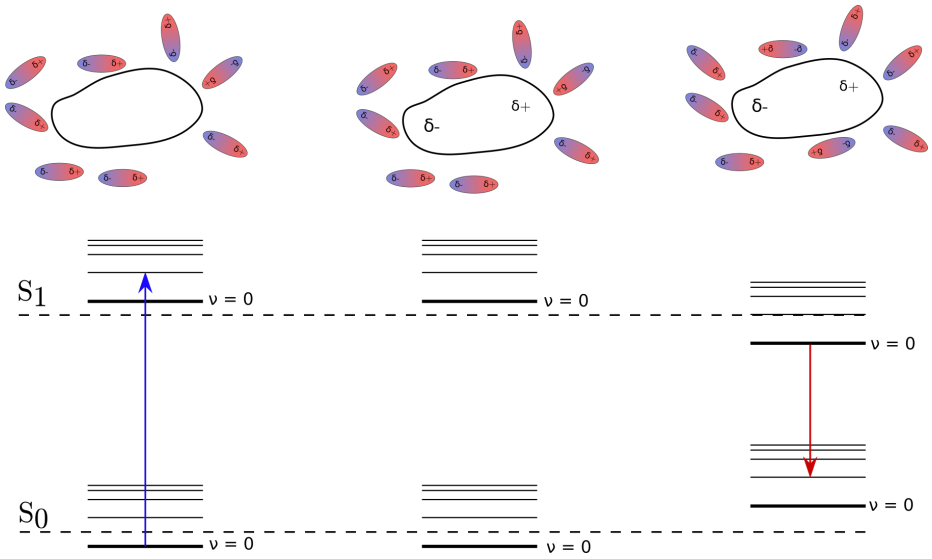

Figure 2.4: Contribution to the stokes shift for molecules in solution. The energy of the S_1 and S_0 levels for the isolated molecule are given by the dashed line while the energy levels in solution are the solid lines. Absorption takes place at higher energy (blue arrow) than emission (red arrow) as the solvent molecules reorganise to stabilise the new charge distribution in the molecule.

exciton self-localisation,[110] and the effect of non-zero torsional angles reducing the coupling strength and breaking conjugation between subunits on the same chain.[39]

2.3.3 Aggregate Formation

Since π-conjugated molecules have a wide, planar backbone structure, aggregation of molecules in the absence of strong steric hindrance often results in the formation of a stack along the line perpendicular to the conjugated plane of the molecule. This arrangement is referred to as π-stacking. The overall driving force favouring aggregate formation over fully solvated isolated molecules is a combination of factors, including electrostatic interactions between molecules with permanent dipoles, dispersion forces due to the large surface-volume ratio of extended conjugated systems, and solvophobic effects.[102]

The formation of a π-stacked aggregate can be described as a sequence of equilib-

ria,[44]

$$\begin{aligned} \mathrm{M} + \mathrm{M} &\rightleftharpoons \mathrm{M}_2 & c_2 &= Kc_1 \\ \mathrm{M}_2 + \mathrm{M} &\rightleftharpoons \mathrm{M}_3 & c_3 &= Kc_2 \\ &\cdots & &\cdots \\ \mathrm{M}_{N-1} + \mathrm{M} &\rightleftharpoons \mathrm{M}_N & c_{N-1} &= Kc_N \end{aligned} \tag{2.8}$$

where the index N is the number of molecules in the aggregate, and c_N is the total concentration of aggregates with N molecules. The equilibrium constant K for addition of an extra monomer to the growing aggregate is assumed to be the same for all equilibria in the Isodesmic Model[44] and is determined by the Gibbs free energy for the reaction (at standard temperature and pressure),[11]

$$\Delta G = -RT\log(K), \qquad \Delta G = \Delta H - T\Delta S. \tag{2.9}$$

According to Equations 2.8 and 2.9, aggregate formation is favoured for high concentrations, low temperatures, or in solutions with poor solvents. Large spectral shifts and variations in fluorescence intensity are commonly observed as a result of the electronic interaction between molecules which are held at close proximity and with specific relative orientation in an aggregate, as described by the exciton model.[111;113]

The energies of a pair of molecules in the ground and exited states are modified by an electrostatic interaction between the two molecules. Both the ground state and excited states of a dimer aggregate are lowered in energy by dispersion forces relative to the isolated molecules, while the upper level is split in two by an interaction due to energy transfer between the two molecules. In the dipole approximation, this is given by[113],

$$E = \frac{\mathbf{M}_1\mathbf{M}_2}{r^3} - \frac{(\mathbf{M}_1.\mathbf{r})(\mathbf{M}_2.\mathbf{r})}{r^5} = \frac{\mathbf{M}_1\mathbf{M}_2}{r_{12}^3}(\cos\theta_{12} - 3\cos\theta_1\cos\theta_2), \tag{2.10}$$

where $\mathbf{M}_x$ is the transition dipole moment for molecule 1, r_{12} is the distance between the molecule centres, θ_{12} is the angle between the two dipole moments and θ_x is the angle between the dipole moment on molecule x and the line connecting the two centres.

When the molecules are aligned head to tail, the in phase combination of the dipole moments leads to electrostatic attraction and a lowering in the energy of the system, while the out of phase (head to head) alignment is higher in energy. For the in phase combination, the dipole transition moments add constructively and the total

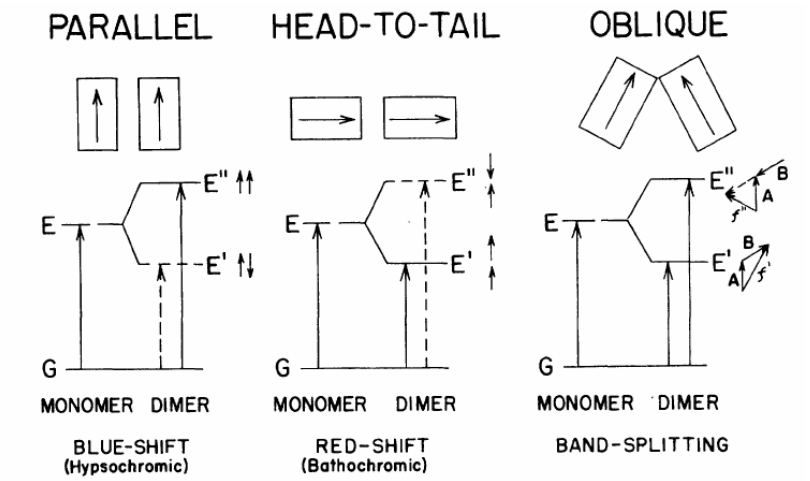

Figure 2.5: A graphical summary of the exciton model for various arrangements of the two molecules in dimers. The energy levels to which transitions are allowed are drawn with a solid line, which inaccessible states are drawn with a dashed line. (Taken from: Kasha, 1963)

oscillator strength of this state is larger than the isolated molecule. Radiative transitions between this and the ground state are therefore fully allowed. In comparison, radiative transitions from the higher energy state are forbidden as the total transition strength is zero. Such an arrangement of molecules is referred to as a J-aggregate, and results in both superradiance and a red-shift of the absorption and emission bands.

When the transition dipole moments are arranged parallel rather than collinear the situation is reversed. The in phase combination of dipole moments results in electrostatic repulsion between the two molecules and is higher in energy than the out of phase combination. Only the higher energy in-phase state can be coupled to the ground state by the electric dipole operator however. This arrangement is referred to as a H-aggregate and results in a reduction of radiative emission from the aggregate, along with a shift of the transition to higher energies.

An intermediate arrangement (oblique, Figure 2.5) is possible which is characterised by a splitting of the upper energy level into two levels, both of which are able to decay radiatively to the ground state. It should be noted that the PL suppression effects are only observed in the limit of weak intermolecular coupling for the 0-0 transition.[196] Thus, in J-aggregates, the ratio of the intensities of the I_{0-0}/I_{0-1} increased while this ratio is decreased in H-aggregates.

The situation for polymers is more complicated than the situation described by the exciton model due to the large number of repeat units per molecule. Relative

to the monomer, spectral features of polymer aggregates can be viewed as resulting from a combination of J-aggregate type interactions [1] between neighbouring units along the polymer chain, and H-aggregate type interactions between units on adjacent chains.[31;234] It should be noted that spectral shifts, in particular hypsochromic shifts which are signatures of H-aggregate formation, are not a reliable measure of the degree of aggregation. The formation of closely packed structures hinders rotation between subunits on a polymer chain and has the effect of increasing the effective conjugation length. This lowers the excitation energy relative to an isolated molecule, even in the case of H-aggregate formation. It is more reliable to compare the ratio of the 0-0 and 0-1 transition intensities.

The degree of aggregation and whether intra (J-type) or inter molecular (H-type) interaction features dominate the PL and absorption spectra of a polymer film or solution depends on the chemical structure of the material, molecular weight of the polymer and the environmental conditions such as temperature, concentration and solvent quality.[105;185;168] In the case of P3HT, Hellmann *et al.* found that the predominant coupling mechanism can be tuned from H-type through to J-type by blending P3HT polymer of increasing molecular weight with a polar polymer poly(ethylene oxide),[96] while Niles *et al.* observed the same by forming nanofibres in poor solvent prior to thin film casting.[168]

When aggregate effects are present in a sample, the absorption and luminescence spectra are no longer mirror images of one another. The absorption spectrum is determined by transition dipole moment to and the number of states at an energy ϵ. The variation of energy of states in a solid is caused by differences in local environment and intramolecular configuration, and for a a disordered organic solid, the density of states (DOS) is described by a Gaussian function[120]

$$g(\epsilon) = \frac{1}{\sqrt{2\pi\sigma}} \exp\left(\frac{-(\epsilon - \epsilon_0)^2}{2\sigma^2}\right), \tag{2.11}$$

where σ is the standard deviation of site energies about the central mean value ϵ_0 and is referred to as the disorder parameter.

[1] These interactions are referred to as J-type interactions because of the similarity of the spectral features observed with those predicted by the exciton model. The origin of these interactions are completely different however; those described in the exciton model arise from electrostatic coupling between two neighbouring molecules,[112] while these are related to the overlap of molecular orbitals on adjacent subunits in the polymer chain.[197]

While the degree of disorder can be seen in the absorption spectrum, this is not the case for photoluminescence, as photon emission does not occur immediately after excitation. During the time delay between absorption and emisson, vibrational relaxation and migration of excitons to a subset of sites with lower energy can occur.[177] This has the effect of narrowing the PL spectrum relative to the absorption spectrum.[109]

Khan *et al.* observed that for films of polyfluorene 44% of all PL emission was observed to originate from low energy sites caused by aggregation induced planarisation of the polymer, even when these sites constituted no more than between 1% and 5% of all sites in the film. This discrepancy was due to rapid energy transfer from high-energy distorted chromophores to low-energy planar sites complete within several picoseconds.[115] This type of migration is an additional contribution to the Stokes shift discussed previously.

Along with the emission spectrum, the radiative emission rate is affected strongly by the mode and strength of aggregation. For an aggregate consisting of N interacting molecules, a band of states will be formed by the interaction of exciton states on each molecule. In the case of a J-aggregate, the lowest level is the one with all transition moments in phase, and so the total transition moment is given by $N^{1/2}\boldsymbol{\mu}$. Since the spontaneous emission rate is proportional to the square of the dipole moment, under low excitation fluence when nonlinear processes such as exciton-exciton annihilation do not occur, the rate of transition is expected to scale as $k_f \propto N|\boldsymbol{\mu}_{21}|^2$.[6] This simple relation breaks down when disorder is introduced into the aggregate as either displacement of the molecules along the aggregation axis, or variation in angle between adjacent units. This disorder has the effect of reducing the observed rate to $k_f \propto N_{eff}|\boldsymbol{\mu}_{21}|^2$, where $N_{eff} \sim T^{-1/3}$ is the effective aggregate size.[198]

In the case of H-aggregates, the reduced total dipole intensity results in a decrease in the radiative emission rate from the lowest level. In practice this is not easily observed as non-radiative decay mechanisms dominate the decay dynamics and lead to a reduction in both excited state lifetime and PL emission. This is the case for 3,3-diethylthiadicarbocyanine[209] and porphyrin[223] aggregates. If, however, aggregation suppresses the main non-radiative recombination pathway the increase in lifetime can be observed. Such a situation was found to occur in dimers of a merocyanine dye by Rosch *et al.* The major non-radiative decay mechanism in isolated merocyanine dyes occurs via torsions within the molecule, leading to a 0.5 ps lifetime. This increases

to 4.4 ps when the molecule planarises and rigidifies on formation of a H-aggregate. Radiative transitions are partially allowed as imperfect alignment of the two molecules breaks the symmetry of the system.[178]

As is the case for small molecules, both the total quantum yield and the radiative lifetime are often strongly quenched in thin films of conjugated polymers as compared to a solution in which each molecule is well solvated and aggregates are not formed. Although the intrinsic radiative lifetime is extended in H-aggregates in the film,[147] the observed emission lifetime is reduced due to increasing non-radiative decay rates.[236;181;147;50;14]

In addition to H- and J-aggregates, complexes can be formed between one molecule in the excited state and a second molecule in the ground state. When the two molecules in the complex are identical the complex is referred to as an excimer and when the two molecules are different the complex is termed an exciplex. These are distinct from H- and J-aggregates as the complex is non-bonding in the ground state and therefore does not alter the absorption spectrum of the molecules involved. Emission from an excimer state has been observed in films of MEH-PPV deposited by spin coating from a tetrahydrofuran solution with, with this excimer emission accounting for 40% of the total emission at longer times.[108] Excimer emission is broad and strongly red-shifted compared to the peak emission from an individual molecule.

2.4 Energy Transfer Processes

As discussed above, rapid energy transfer along and between molecules to sites lower in energy results in temporal evolution of the photoluminescence spectrum observed in conjugated polymer systems. This process occurs within several picoseconds after excitation.[115] This energy transfer is the cause of the excitation dependence of the peak emission energy and PL anisotropy, r, observed by Rauscher *et al.* in PPV films.[177] The value of r here is given by

$$r = \frac{I_{\parallel} - I_{\perp}}{I_{\parallel} + 2I_{\perp}}, \tag{2.12}$$

where $I_{\parallel}$ is the intensity of the PL with polarisation parallel to the excitation pulse, and $I_{\perp}$ is the intensity of the PL polarised perpendicular to the excitation beam.

In disordered systems, energy transfer is incoherent and occurs by a series of hops between sites, with vibrational or torsional relaxation occurring before transfer can

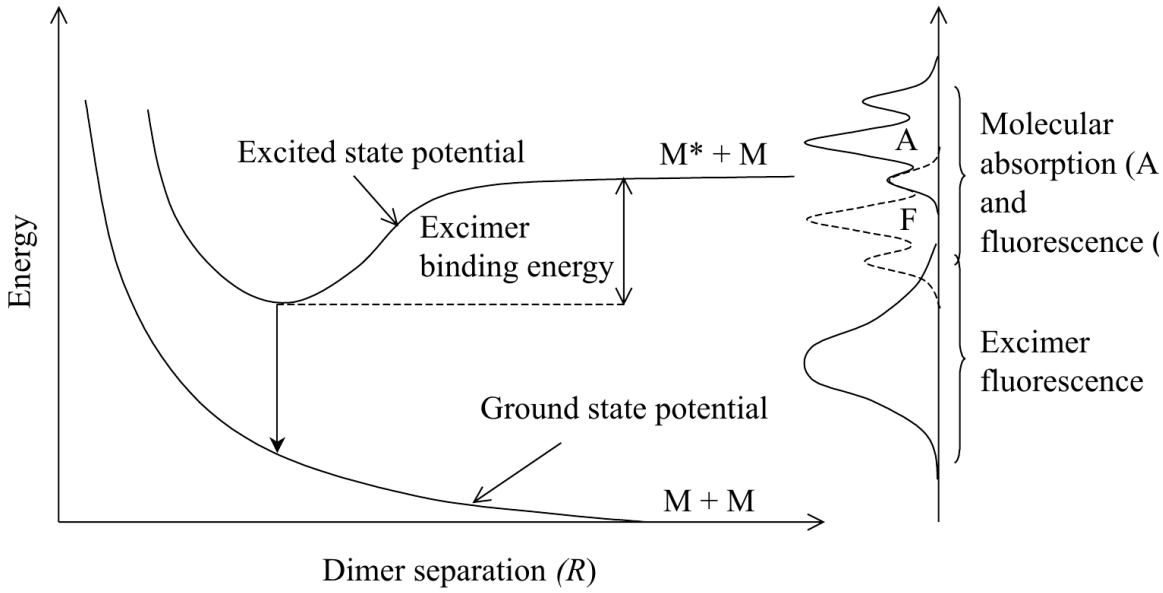

Figure 2.6: The potential energy surfaces for the lowest excited state and ground state of an excimer as a function of the intermolecular separation (left), and the absorption and emission spectra of the isolated molecules and excimer (right). (Taken from: Barford, 2005).

take place.[16] The transfer rate between donor, D, and acceptor, A, sites is given by the Fermi Golden Rule

$$k_{ET} = \frac{2\pi}{\hbar} |\langle \Psi_f | H' | \Psi_i \rangle|^2 \rho_{DA} \tag{2.13}$$

where ρ_{DA} is related to the overlap between the emission spectrum of D and the absorption spectrum of A.

When the initial and final wavefunctions are given by[120]

$$|\Psi_i\rangle = \frac{1}{\sqrt{2}} (\Psi_D^*(1)\Psi_A(2) - \Psi_D^*(2)\Psi_A(1)) \tag{2.14}$$

$$|\Psi_i\rangle = \frac{1}{\sqrt{2}} (\Psi_D(1)\Psi_A^*(2) - \Psi_D(2)\Psi_A^*(1)) \tag{2.15}$$

The integral in 2.13 becomes

$$\langle \Psi_f | H' | \Psi_i \rangle = \langle \Psi_D(1)\Psi_A^*(2) | H' | \Psi_D^*(1)\Psi_A(2) \rangle - \langle \Psi_D(1)\Psi_A^*(2) | H' | \Psi_D^*(2)\Psi_A(1) \rangle \tag{2.16}$$

2.4.1 Förster Resonant Energy Transfer (FRET)

The first term in Equation 2.16 describes a transition in which electrons 1 and 2 stay on their respective sites, and the excitation moves from the donor to the acceptor,

while the second term describes energy transfer by a swap of the electrons between the donor and acceptor. The first of these two integrals is the Coulomb mediated coupling and its contribution to the overall energy transfer rate was described by Förster in 1948.[74;75]

By making the approximation that the transition moment on each molecule involved in energy transfer can be assumed to be a dipole, and taking into account the distribution of orientations and energy levels in condensed phases, Förster showed that energy transfer mediated by the Coulomb term occurs at a rate,

$$k_{FRET} = \frac{9000\log(10)\Phi_D\kappa^2}{128\pi^5 N_A n^4 \tau_D R^6} J \tag{2.17}$$

where Φ_D and τ_D are the photoluminescence quantum yield and total lifetime (radiative and non-radiative) of the donor in the absence of any acceptor. N_A is Avogadro's number, n is the refractive index of the solvent and R is the separation between donor and acceptor. The crucial element of the theory, the overlap factor J is given by

$$J = \int_0^\infty \epsilon_A(\lambda) f_D(\lambda) \lambda^4 \mathrm{d}\lambda, \tag{2.18}$$

where λ is the wavelength, ϵ_A is the extinction coefficient of the acceptor in solution, and f_D is the emission spectrum of the donor, normalised such that $\int f_D(\lambda)\mathrm{d}\lambda = 1$.

The value of κ describes the relative orientation of the absorbing and emitting dipoles,

$$\kappa = \hat{\boldsymbol{\mu}}_D \cdot \hat{\boldsymbol{\mu}}_A - 3(\hat{\boldsymbol{\mu}}_D \cdot \hat{\mathbf{R}})(\hat{\boldsymbol{\mu}}_A \cdot \hat{\mathbf{R}}), \tag{2.19}$$

with the vectors $\hat{\boldsymbol{\mu}}_D$ and $\hat{\boldsymbol{\mu}}_A$, and $\hat{\mathbf{R}}$ in the above equation are the unit vectors in the direction of the dipole moments on D and A, and of the vector connecting the centre points of the two molecules. The constants, κ, and J can be combined to give a recast version of Equation 2.17

$$k_{FRET} = \frac{1}{\tau_D}\left(\frac{R_0}{R}\right)^6 \tag{2.20}$$

where R_0 is the Förster radius, defined as the separation at which the rate of energy transfer is equal to the total rate of decay from the excited state by either radiative or non-radiative pathway in the absence of any acceptor.[46]

The dipole approximation used by Förster in deriving this equation requires that the relative size of the molecules involved in the transition be much smaller than the separation between the two. At small distances such as separations between π-stacks

of polymer chains in a H-aggregate, the dipole approximation breaks down. Modified versions of the Förster theory including the line-dipole,[229] distributed monopole,[97] or transition density cube models[125] can be used in this situation.

2.4.2 Dexter Transfer

The second term in Equation 2.16 is mediated by the exchange interaction and involves exchange of two electrons, one in the upper singly occupied molecular orbital (SOMO) of the excited donor and one from the HOMO of the acceptor. As such, this energy transfer mechanism, first proposed by Dexter in 1953,[60] requires orbital overlap between the two chromophores. The energy transfer rate by this process is given by

$$k_D = A \exp(-2R/L) J, \tag{2.21}$$

where R is the separation between the two chromophores, L the effective average radius of the chromophores involved in the transition, and A is a constant. $J = \int E_A(\lambda) F_D(\lambda) \lambda^4 \mathrm{d}\lambda$ here is the spectral overlap of the donor emission (F_D) and acceptor absorption (E_A), however unlike the term J in the Förster model, both spectra are normalised such that[16]

$$J = \int E_A(\lambda) F_D(\lambda) \mathrm{d}\lambda \tag{2.22}$$

$$F_D(\lambda) = \frac{\lambda^3 f_D(\lambda)}{\int \lambda^3 f_D(\lambda) \mathrm{d}\lambda} \tag{2.23}$$

$$E_A(\lambda) = \frac{\lambda^3 \sigma_A(\lambda)}{\int \lambda^3 \sigma_A(\lambda) \mathrm{d}\lambda} \tag{2.24}$$

The Förster transfer mechanism is applicable only to transfer of singlet excitations, while Dexter transport is a possible mechanism for both singlet and triplet energy transfer, and at very short separation both mechanisms contribute to the total energy transfer rate.[190] However, as the Dexter transport mechanism requires the donor and acceptor chromophores to be at extremely close range, transport for D-A pairs separated by more than $\sim 5\,\text{Å}$ is dominated by the Förster type transport. The strong exponential dependence of the transfer rate on the separation between donor and acceptor units can be relaxed in systems in which the two units are covalently bound by a bridging unit. This can be either a conjugated bridge,[5] or an rigid saturated bridge.[191] The effect of the bridging units is to replace the distance dependence in the exponent $2R/L$ with βR, where β is a system dependent parameter that can take

values between $0.1\,\text{Å}^{-1}$ and $1.33\,\text{Å}^{-1}$ depending on the bridging unit and the energy gap between donor and bridge units.[189;65] (cf. $2/L = 1.2$ to $2.0\,\text{Å}^{-1}$ [189])

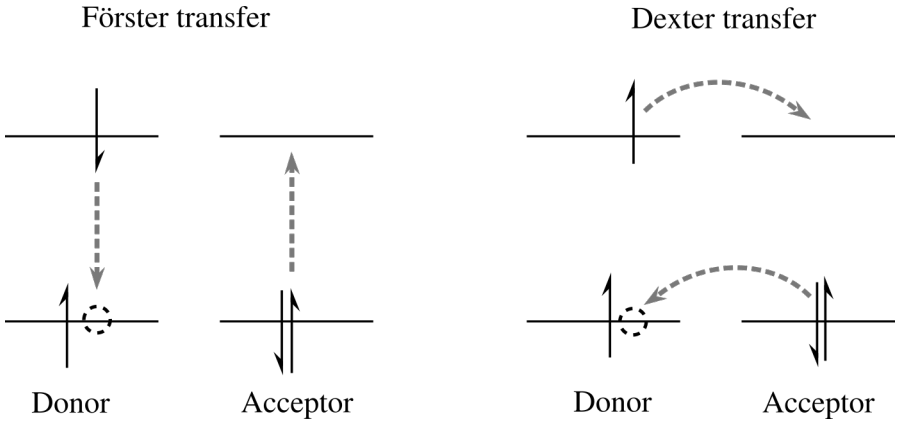

Figure 2.7: Representation of the Förster and Dexter energy transfer mechanisms. The Förster mechanism is equivalent to transfer of the excitation by simultaneous absorption and emission of a virtual photon from the donor and acceptor while the Dexter mechanism occurs by two-electron transfer and requires orbital overlap.

2.4.3 Exciton Transport in Bulk

Over time a photogenerated exciton will migrate to sites of decreasing energy and will eventually become trapped when sites of equal or lower energy are separated by a distance greater than the Förster radius. This process can be modelled with Monte Carlo simulations[18;186] in which an excitation is generated on a single lattice point corresponding to one conjugated section of a polymer. The energy of each site in the lattice is assigned according to a Gaussian distribution, and the rate of energy transfer to another site is determined by the Förster (for singlet excitons) and Dexter type (for triplets or free charges) coupling if the new site is of lower energy, or is multiplied by a Boltzman factor if the new site is higher in energy. Due to the close proximity of acceptor sites to any given site occupied by an exciton, migration in the solid state is dominated by transfer between chains rather than migration along on chain,[24] and most of this transport is completed within a few picoseconds following creation of the exciton. When polymer chains are isolated in solution[24] or by incorporation into a host matrix, migration along the chain can be observed on a time scale of several hundred picoseconds or nanoseconds, *i.e.* at a similar rate to radiative decay.[166]

The average length that an exciton can diffuse along and between polymer chains before becoming trapped and decaying either radiatively or non-radiatively is given

by $L_D = \sqrt{aD\tau}$, where a =1, 2 or 3 is a dimensionality constant, D is the diffusion coefficient exciton and τ is the lifetime. In particularly well ordered systems, such as single crystals of rubrene[163] and tetracene,[4] diffusion lengths of $\sim$ 5 µm have been observed. These extremely long diffusion lengths are associated with long lived triplet excitons which are produced with high efficiency by singlet fission in polycyclic hydrocarbons such as tetracene.[194] By comparison, triplet excitons in polymers are produced in much lower yield by intersystem crossing between the S_1 and higher lying triplet states T_n ($n > 1$) by σ-π mixing or at heavy atoms, eg. S sites in polymers with thiophene units.[23;34]

Unlike in organic crystals, diffusion lengths in conjugated polymer films are generally observed to lie in the range 5 to 15 nm.[150;193;140] These values are similar despite the different chemical structure and film morphologies of the materials measured. An explanation for the small range of reported L_D values was proposed by Markov *et al.*,[150] who measured the diffusion coefficient and DOS of a series of PPV based polymers. They observed that while excitons do show increasing diffusivity with decreasing disorder, this gain is offset by the more mobile excitons reaching non-radiative quenching and trap sites more quickly than in disordered films.[150] Such sites may be those at which intersystem crossing is promoted, low energy aggregates, or chemical defects which act as electron trapping sites. Chemical defects can either be sites on polymer chains, such as carbonyl groups which are formed by photo-oxidation of vinyl bonds in MEH-PPV,[235] or impurities left over from the polymer synthesis.[153]

2.5 Organic Photovoltaics

Polymer solar cells make use of conjugated polymers as the major absorbing layer and have the advantage of being easily processable from solution unlike inorganic solar cells based on a p-n junction. A consequence of the relatively large exciton binding energy (0.2–1 eV) in conjugated polymers discussed above is that separation of a bound electron hole-pair into free charges is an inefficient process in neat polymer films without any external driving force.[180] Polymer solar cells incorporate a junction between two different molecules with staggered energy levels (type-II heterojunction) such that electron transfer from the majority absorbing material (the donor) to an acceptor is energetically favoured with respect to a neutral exciton on either the donor or the acceptor. At the heterojunction, electron transfer from the LUMO of the donor to the LUMO of the acceptor occurs. This often results in a bound charge

transfer exciton, which then dissociates, forming polarons in the donor (positively charged) and acceptor (negatively charged). These charges then migrate through the donor/acceptor to the electrodes where they can be extracted. This is represented graphically in Figure 2.9.

The efficiency of this process per photon incident on the device is referred to as the external quantum efficiency,

$$\mathrm{EQE}(\lambda) = \eta_{\mathrm{A}}(\lambda) \times \eta_{\mathrm{ED}}(\lambda) \times \eta_{\mathrm{CT}}(\lambda) \times \eta_{\mathrm{CC}}(\lambda) \tag{2.25}$$

where $\eta_{\mathrm{A}}(\lambda)$ is the fraction of incident photons with wavelength λ that are absorbed by the device, η_{ED} is the fraction of excitons which can successfully diffuse through the donor material and reach an interface, η_{CT} is the efficiency with which excitons dissociate at the interface and form free charges, and η_{CC} is the efficiency with which the free charges migrate to and are collected at the electrodes.

When the two electrodes are connected through an external circuit with no applied voltage, the Fermi levels of the two materials equalise as electrons are free to flow through the system. If two electrodes are materials with different work functions are used (e.g. indium tin oxide, ITO, and aluminium, Al), a field develops and is spread evenly through the device.[120] Free charges which are generated at the interface following absorption of a photon and dissociation of an exciton then drift in this electric field to the electrodes. The net current measured under these conditions is referred to as the short circuit current of the device, J_{sc}. This point appears on a plot of the measured current against applied voltage of the solar cell device as the point which crosses the y-axis at $V = 0\,\mathrm{V}$, as shown in Figure 2.8. As a forward voltage is applied across the device, a point is reached at which the current flow stops completely as the built in field is canceled out by the applied field. This point is referred to as the open circuit voltage point, V_{OC}.

As there is no net current at V_{OC}, and no voltage at J_{sc}, a solar cell under irradiation at either of these points produces no electrical power. The maximum possible power output of the cell lies between these two points. The voltage and current produced at this maximum power point (MPP) are V_{MPP} and J_{MPP} respectively. In an ideal solar cell, these values will correspond to the open circuit voltage and short circuit current, however in a real cell this is never realised as low built in fields and charge recombination competing with charge extraction.[120] The deviation from ideality is described by the fill-factor,

$$FF = \frac{V_{\mathrm{mpp}} \cdot J_{\mathrm{mpp}}}{V_{\mathrm{OC}} \cdot J_{\mathrm{SC}}}. \tag{2.26}$$

This is the ratio of the ideal and maximum measured power output, or the ratio of the areas of the two grey rectangles in the current-voltage curve given in Figure 2.8.

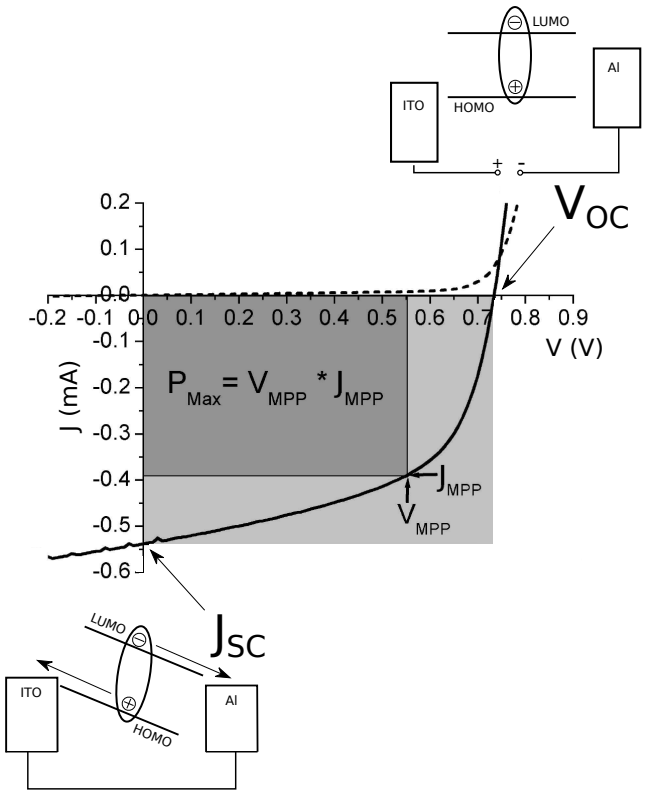

Figure 2.8: A current-voltage (J-V) curve (centre) of an organic solar cell, and metal-insulator-metal picture diagrams showing the relative positions of ITO and Al electrode Fermi levels and donor/acceptor HOMO/LUMO energy levels in short-circuit (bottom) and open-circuit (top) conditions. The solid line in the JV-curve shows the response of the cell under illumination and the dashed line shows the dark response. The short circuit current, J_{SC}, open circuit voltage, V_{OC}, and both the current and voltage at the maximum power point are shown, and the fill-factor of the device is represented as the ratio between the dark grey (real power) and light grey (ideal cell power) rectangles. (Adapted from: Hoppe and Sariciftci, 2011).

In comparing different solar cell devices, it is useful to determine the power conversion efficiency of the cell, which is given by

$$\eta_{\mathrm{PCE}} = \frac{\text{Electrical power out}}{\text{Incident light power}} = \frac{\mathrm{FF} \cdot J_{\mathrm{SC}} \cdot V_{\mathrm{OC}}}{I}, \tag{2.27}$$

where J_{SC}, V_{OC}, and FF are the short circuit current, open circuit voltage, and fill factor as described above, and I is the irradiance incident on the cell.

The electrical parameters V_{OC} and J_{SC}, which are easily determined from the current-voltage curve, are also directly related to the EQE and the energy levels of

the donor and acceptor materials. Scharber *et al.*[184] determined empirically that the V_{OC} is directly related to the difference in energy between the HOMO and LUMO energy levels of the donor and acceptor units, such that

$$V_{\mathrm{OC}} = (1/e)(|E^{\mathrm{D}}_{\mathrm{HOMO}}| - |E^{\mathrm{A}}_{\mathrm{LUMO}}|) - 0.3\,\mathrm{V}. \tag{2.28}$$

The short circuit current is directly related to the EQE by

$$J_{\mathrm{SC}} = EQE \times e \times \Phi_{\mathrm{ph}}, \tag{2.29}$$

where e is the charge of one electron and Φ_{ph} is the photon flux incident on the device.

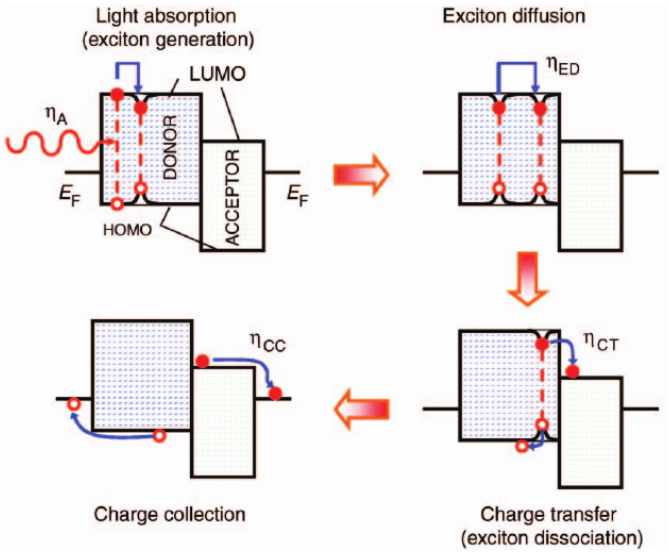

Figure 2.9: Mechanism of photocurrent generation in polymer photovoltaics. The horizontal lines to the left and right of each illustration are the Fermi energies of the anode and cathode respectively. Starting from the top left and going clockwise, an exciton is first generated by absorption of an incident photon with energy $E > E(LUMO) - E(HOMO)$, the total absorption efficiency is given by η_A. Next, exciton migration to a donor molecule at the heterojunction takes place, over a distance equal or less than the diffusion length L_D. The fraction of excitons reaching the interface is given by η_{ED}. Charge transfer from the LUMO of the donor to the LUMO of the acceptor, followed by separation of the charge transter (CT) state then occurs with efficiency η_{CT}, and migration to and extraction at the electrodes takes place with efficiency η_{CC}. (Taken from: Forrest, 2011).

Improving the photovoltaic device performance therefore requires increasing each of the three parameters: J_{SC}, V_{OC}, and FF. While there are strategies to improve the photocurrent and open circuit voltage, maximising the fill factor is difficult as it

depends on too many factors, but is essentially governed by the number of charges which are collected instead of recombining in the cell. The photocurrent can be increased by maximising each of the four ηs in Equation 2.25, and the V_{OC} can be increased by maximising the difference between the donor HOMO and acceptor LUMO energies, while retaining a large enough offset between donor and acceptor LUMOs to promote efficient charge transfer at the interface.

The extinction coefficient for absorption in the visible range of many organic polymers is high, around 10^4–$10^5\,\mathrm{cm}^{-1}$ [68] as the π–π^* transition is an allowed transition. These high extinction coefficients allow for strong absorption over a wide range of the visible spectrum with energy greater than the polymer band gap. These large extinction coefficients give up to 90% absorption at peak wavelengths on a single pass through a 200 nm thick film. The first term in Equation 2.25, η_{A}, can therefore be increased by either increasing the thickness of the active layer, or by reducing the band gap of the polymer, thereby pushing the absorption onset further toward the near infra-red and enabling absorption over a wider range of the solar spectrum. One synthetic strategy to achieve this is to incorporate electron-rich donor and electron-poor acceptor units on the same chain.[61] These types of low band-gap polymers have been used almost exclusively in devices which exhibit power conversion efficiencies beyond those of the benchmark polymer P3HT.[89;92;52]

There is a trade-off however between increasing J_{SC} by utilising a larger fraction of incident photons, and the necessity for a large V_{OC}, as determined by the donor-HOMO–acceptor-LUMO gap. By considering this balance, Scharber *et al.* calculated that maximum device efficiencies should be attainable when the band gap of the polymer is between $1.35 < E_g < 1.65\,\mathrm{eV}$, assuming the LUMO of the polymer is well aligned energetically with that of the PCBM acceptor.[184]

The second term in Equation 2.25 is the fraction of photogenerated excitons which can reach the heterojunction before recombination or trapping occurs. In simple bilayer structure devices, this value is extremely low for polymer film thicknesses much greater than the exciton diffusion length, L_D. η_{ED} efficiencies approaching unity are achieved whenever a heterojunction is located within $2L_D$ from any point in a polymer domain. This can be achieved by use of a bulk heterojunction,[240] formed through either co-deposition of the two materials to form a single mixed layer with separate donor and acceptor domains produced by spontaneous phase separation, or gradually varying mixture of the two materials formed by sequential deposition of donor and

acceptor, followed by thermal annealing to promote diffusion of the fullerene acceptor into the donor layer.[145]

While the development of low-bandgap co-polymers and the BHJ have aided the optimisation of η_A and η_{ED}, similar breakthroughs for η_{CT} and η_{CC} have not yet occurred. When the exciton reaches the D/A interface, extremely rapid and efficient charge transfer takes place from the donor LUMO to the acceptor LUMO.[183] The electron on the acceptor and hole on the donor are still subject to a strong attractive force however, even though they reside on neighbouring molecules, and together form a bound charge-transfer state.

The binding energy of the CT state relative to separated polarons has been determined experimentally by Gélinas *et al.* to be $\geq$250 meV.[80] This value is an order of magnitude larger than thermal energy at room temperature, and hence bound CT states do not generally dissociate spontaneously. Instead, they have been observed to decay radiatively to the ground state following relaxation,[144;159] can reform donor excitons via an endothermic process,[159] or form triplet excitons in either the donor or acceptor material, depending on the relative energies of the CT, $^{D}T_1$ and $^{A}T_1$ states.[170]

The formation of free charges in high yield is required for efficient PV operation, however details of the mechanism by which this crucial process occurs is still unclear and remains the subject of debate, and there have been numerous comprehensive reviews written on this topic.[79;72;45]

It has been observed by several groups that a fraction of photogenerated excitons near the interface in BHJ films form free charges within 50–100 fs,[93;85] with the population of short-lived delocalised band states on the polymer material[12] and PCBM aggregates[81] playing a crucial role in facilitating the efficient formation of free charges. Excitations which do not dissociate on this timescale form the bound CT state, and the mechanism by which this state dissociates is not clear. In particular, whether excess excitonic energy in the form of higher lying (S_2 or higher) exciton states[85] or relaxed (S_1) donor excitons are required to populate hot (vibrationally excited) CT states which rapidly dissociate,[171;12;81] or whether separation occurs from the relaxed CT state,[221] remains to be determined. In the case of dissociation occurring from the relaxed state, the driving force for separation in this case is also unclear,[79] however a range of factors have been reported to influence the efficiency

of charge separation. These include variations in morphology and film crystallinity, charge mobility, electric field strength, and charge delocalisation.[45;120;79]

The last of the terms in Equation 2.25 is the charge collection efficiency, η_{CC}. This is determined by the competition between recombination in the bulk, and charge migration to followed by extraction at the electrodes. The two major recombination pathways in OPV are bimolecular recombination at the heterojunction, proceeding via reformation of the bound CT state described above, or monomolecular recombination of a mobile charge with a trapped charge of opposite polarity.[176] One method of increasing η_{CC} is by optimising the nanoscale morphology and increasing phase separation in order to minimise recombination while maintaining a high fraction of exciton dissociation at the interface. This is commonly achieved by post-processing steps including solvent treatment[247] and thermal annealing.[173] Additionally, high hole mobility polymers will reduce the time required for charge extraction, minimising the amount of possible recombination.[93]

Chapter 3

Experimental Methods

This thesis is primarily concerned with the energy transfer processes in π-conjugated polymers, dye molecules and direct band-gap organic-inorganic hybrid materials as applied in excitonic photovoltaic devices. The photophysics of luminescent materials such as these can be probed by monitoring the polarisation and wavelength of emission from photoexcited species in solution or solid state as a function of time after excitation. Information on the timescales of solvent and vibrational relaxation processes, energy transfer processes, molecular orientation, the degree of aggregate formation and the persistence of excitation can be determined by monitoring the photoluminescence (PL) emission. Each of these processes occur on timescales ranging from between 10^{-12} s and 10^{-10} s for vibrational and solvent relaxation processes. Energy transfer can occur over timescales ranging from anywhere between 10^{-15} s and 10^{-9} s depending on the strength and mechanism of interaction between the chromophores involved.[112] Exciton lifetimes in many organic conjugated materials are around 10^{-9} s,[126] increasing up to the hundreds of nanoseconds for hybrid organic-inorganic materials.

The measurement of time-resolved PL requires generation of pulsed radiation with a pulse duration which is short compared to the timescale of the processes being studied. Two methods of producing short laser pulses are the active mode-locking in solid-state lasers and gain switching in semiconductor diode lasers. These two processes are described in Sections 3.1.1 and 3.1.2.

The two detection methods used in this thesis, photoluminescence upconversion (PLUC) and time correlated single photon counting (TCSPC) are described in Sections 3.2.1 and 3.2.2. In PLUC, sub-ps time resolution is made possible by the short (100 fs) pulse width of the laser limiting the sum-frequency generation process occur-

ring at a crystal with nonlinear optical properties. The overall resolution is limited by both the width of the gate pulse and dispersion effects in the crystal. For a sample with short optical path length relative to the pulse width, the time resolution of the system described in this thesis is approx 300 fs as determined by cross-correlation of the gate beam and laser light scattered from a roughened glass disc held at the sample position.

The sub-ps resolution of the UC measurement is useful for probing fluctuations in PL emission at short times after excitation, but can only be used over a window of approx 1 ns. This is because probing the sample PL intensity at different times requires adding additional path length to the gate beam, which is limited by the length of available delay stages and issues with beam divergence. In comparison, TCSPC can be used to measure the PL intensity over a time frame determined by the repetition rate of the laser, which can be long as $\sim 10\,\mu s$ for gain-switched diode lasers. The time resolution of TCSPC is lower than that of the PLUC experiment at 35 ps, and is limited by the speed of the detection equipment used. Together, the two techniques allow time resolved PL measurement over the range 10^{-13} to 10^{-7} s.

The experimental set-up for the PLUC and TCSPC is described in Section 3.3. The calibration procedure for establishing the phase-matching condition of the SFG process and determining the spectral response of the system is described in Sections 3.4. In order to accurately determine lifetimes of processes, the temporal response of the system must be taken into account when analysing experimental data and methods by which this can be achieved are described in Section 3.5.

3.1 Ultrashort Pulse Generation

Central to all time-resolved photoluminescence techniques is the generation of pulses which are temporally short relative to the processes under investigation. PL decay lifetimes of organic molecules in solution and film can range from 100 ps to several nanoseconds, while energy transfer processes can range from < 1 ps to ~ 10 ps, depending on the transfer mechanism.[112] For the work described in this thesis two different laser sources were used in time resolved photoluminescence measurements. The Spectra Physics MaiTai is a mode-locked Ti:Sapphire laser with 100 fs pulse duration and 80 MHz repetition rate and was used for PLUC and some TCSPC measurements. The other was a pulsed diode laser with ~ 180 ps pulse duration, used for

TCSPC measurements on samples with PL lifetime longer than the 12.5 ns window imposed by the cavity length of the Ti:Sapphire laser.

3.1.1 Mode-Locked Ti:Sapphire Laser

In the laser cavity of length d many longitudinal modes operate concurrently, and the total electric field (for a linear cavity and linearly polarised light) is given by [59]

$$E(t,z) = \sum_{m=-(N-1)/2}^{(N-1)/2} \Re[E_0 \mathrm{e}^{-i((\omega_0+m\Delta\omega)t-k_m z)+\phi_m)}] \tag{3.1}$$

where $\Delta\omega = c\pi/d$, $k_m = \frac{(\omega_0+m\Delta\omega)}{c}$ and $\omega_0 - m\Delta\omega \leq \omega \leq \omega_0 + m\Delta\omega$ lies within the range of frequencies $2\pi\Delta f$ for which laser gain is above threshold.

If the $N = 2m+1$ modes have a random phase relation ϕ_m between one another, the total intensity fluctuates around a mean value $\sim N|E_0|^2$ and these fluctuations are periodic with a time constant $T = 2d/c$ as shown in Figure 3.1. If all the modes can be locked together with the same phase, the modes will all interfere constructively

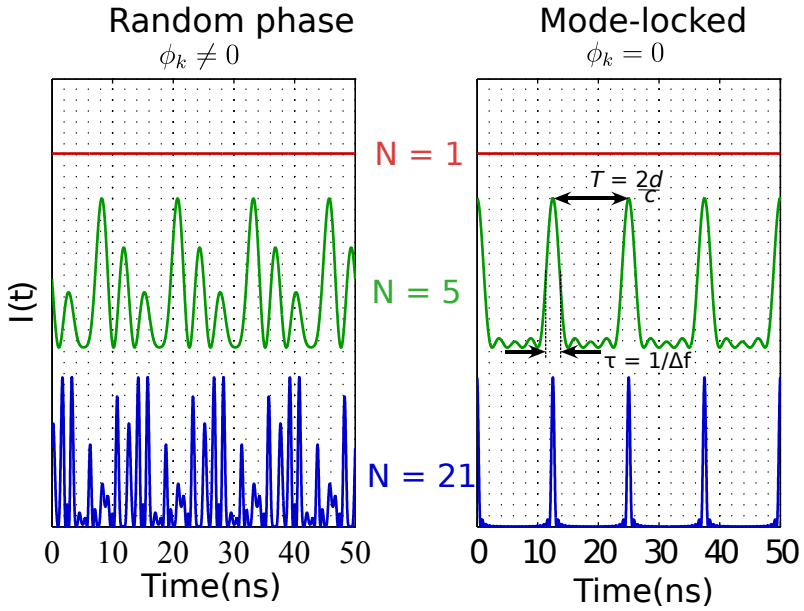

Figure 3.1: Simulated output intensity for a cavity of length $d = 1.87$ m with $N = 1, 5$ or 21 active modes. Left - no mode-locking mechanism active, right - active mode-locking. When no mode locking is present, the output is sequence of peaks repeating at intervals of $T = 2d/c$. When active mode-locking is switched on, the phase difference between each mode is zero and constructive interference occurs once per round-trip. Output pulses repeat at intervals of $T = 2d/c$ and the pulse width decreases with increasing number of modes.

at one point per round-trip of the cavity forming one pulse, and Equation 3.1 reduces to

$$
\begin{aligned}
E(t,0) &= \sum_{m=-(N-1)/2}^{(N-1)/2} E_0 \mathrm{e}^{-i(\omega_0 + m\Delta\omega)t} \\
&= E_0 \cos(\omega_0 t)[1 + 2 \sum_{m=1}^{(N-1)/2} \cos(m\Delta\omega t)] \qquad (3.2) \\
&= E_0 \frac{\sin(\frac{N\Delta\omega t}{2})}{\sin(\frac{\Delta\omega t}{2})} \cos(\omega_0 t) \qquad (3.3) \\
&. \qquad (3.4)
\end{aligned}
$$

This results in pulses separated by

$$T = \frac{2d}{c} = \frac{2\pi}{\Delta\omega} \qquad (3.5)$$

with pulse width given by

$$\tau = \frac{2\pi}{N\Delta\omega} = \frac{1}{\Delta f}. \qquad (3.6)$$

Phase matching can be achieved by various techniques including active mode-locking, passive mode-locking with saturable absorbers, and Kerr-lens mode-locking.[91] Active mode-locking involves modulating the electric field amplitude at a set frequency Ω, usually with an acousto-optic modulator (AOM). When acting on the central mode with frequency ω_0, this produces side-bands in the frequency domain at $\omega_0 \pm \Omega$. If $2\Omega = c\pi/d$, the spacing between the central and side bands will be equal to the neighbouring modes ω_{+1} and ω_{-1}. In this way, the relative phases between all active modes in the laser are locked together. In the MaiTai, a fast-photodiode measures the period of mode beating in the CW output (Figure 3.1, LHS) in order to determine the correct frequency for the AOM. This variant of active mode-locking is termed regenerative mode-locking and allows for compensation of the modulator frequency following a minor change in the cavity, thus increasing laser stability.

($Ti^{3+}Al_2O_3$) has a working range of 650 – 1100 nm ($\sim$ 180 THz), and, since the minimum attainable pulse width is inversely proportional to the spectral range of the laser, it is an ideal material for sub-ps pulsed systems. Pulse durations of as short as 5 fs are achievable with Kerr-lens mode-locking. Such short pulse widths are spectrally broad and cannot be achieved by active mode-locking methods. The regenerative mode-locked MaiTai used in this thesis has a pulse duration of 100 fs, bandwidth of 10 THz ($\sim$ 20 nm at 700 nm) and repetition rate $T = 80$ MHz.

3.1.2 Pulsed Diode Laser

As the resonant cavity of semiconductor lasers is the semiconductor material itself, addition of a saturable absorber or AOM for passive/active mode-locking is not possible. Pulsed operation in these lasers is instead achieved by Gain Switching. If a strong pump current is switched on, a large number of charge carriers are rapidly injected into the semiconductor material, raising the number of carriers well above the threshold level. PL from the diode changes from predominantly spontaneous to stimulated emission and excess charge is rapidly depleted. The photon and charge densities are described by a system of coupled rate equations [58]

$$\frac{dN}{dt} = \frac{J(t)}{ed} - \frac{N}{\tau_s} - \alpha(N - N_0)S \tag{3.7}$$

$$\frac{dS}{dt} = \Gamma\alpha(N - N_0)S - \frac{S}{\tau_{phon}} + \Gamma k\frac{N}{\tau_s} \tag{3.8}$$

The terms on the right hand side of Equation 3.7 are : *(i)* the generation rate by charge injection ($J(t)$ is the time dependent pump current, e is the electronic charge, d is the layer thickness of the semiconductor material); *(ii)* the reduction of charge carriers by spontaneous recombination (N is the charge carrier density and τ_s is the lifetime for spontaneous recombination); *(iii)* the depletion/formation of charge carriers by stimulated emission/absorption (α is the gain coefficient, S is the photon density and $N - N_0$ determines whether SE or absorption occurs).

Equation 3.8 is a rate equation for the photon density, with terms describing: *(i)* the number of SE photons exiting the device (Γ is the optical confinement factor); *(ii)* photon depletion by interaction with phonons (τ_{phon} is the phonon lifetime); *(iii)* photon creation by spontaneous recombination. A solution for these equations for an AlGaAs stripe-geometry heterostructure diode laser is shown in Figure 3.2. [58]

If the current applied to the laser is turned off as the emission intensity peaks, carriers will be depleted to below threshold and only a single pulse of light is emitted, whereas a series of peaks with decreasing amplitude would be produced if the high pump current were maintained. [210] Pulses produced by this method are in general between 50–130 ps in duration (FWHM) and span a wavelength range from 375–1600 nm as a wide variety of semiconductor materials and device architectures can be used to make diode lasers. Since the pulse generation process is electronically controlled the repetition rate of these lasers are completely tunable between 2.5 MHz and 80 MHz.

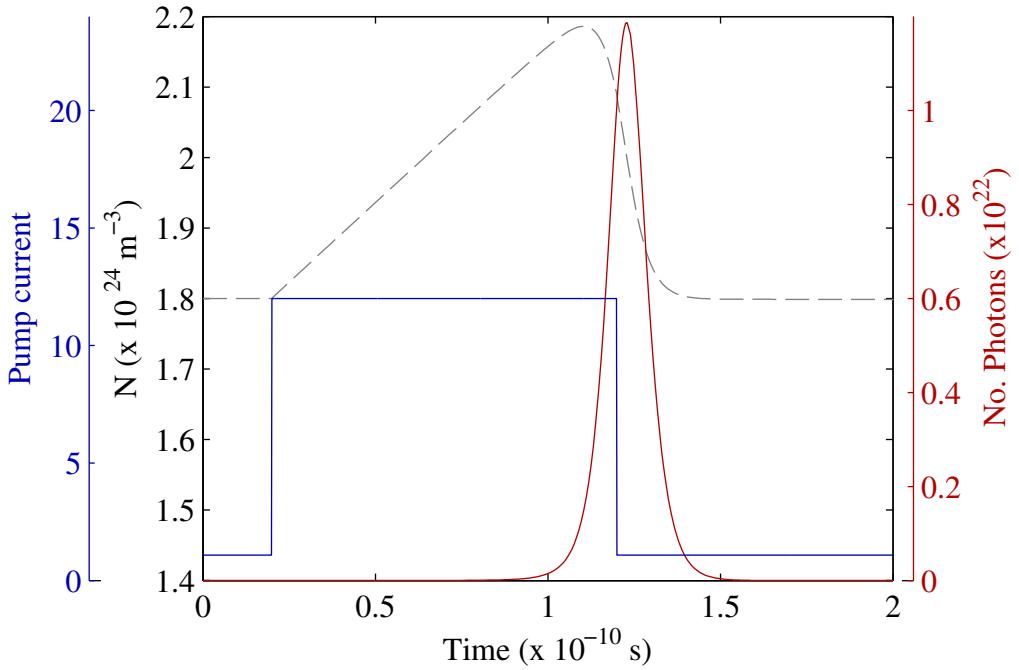

Figure 3.2: Simulation of gain-switching a semiconductor diode laser as described by Equations 3.7 and 3.8. The pump current (blue line) is the sum of a continuous background current and a temporary extra burst of current switched on whenever a pulse is required. The extra current injects extra charge carriers (dashed black line) which decay radiatively. When above the threshold concentration, stimulated emission occurs, rapidly decreasing the number of charge carriers and increasing the photon flux. If the pump pulse is switched off, carriers are depleted to below threshold and only one pulse is produced.

3.2 Time-Resolved Photoluminescence

3.2.1 Photoluminescence Up-conversion

The polarisation of a medium by monochromatic light waves with frequency ω can be expressed by a series[27;201]

$$\begin{aligned} \mathbf{P} &= P^{(1)} + P^{(2)} + P^{(3)} + \dots \\ &= \epsilon_0(\chi^{(1)}\mathbf{E} + \chi^{(2)}\mathbf{E}^2 + \chi^{(3)}\mathbf{E}^3 + \dots) \end{aligned} \tag{3.9}$$

where the first and second terms are the referred to as the linear and second order contributions to the total polarisability respectively.

If a beam consisting of two monochromatic components with frequencies ω_1 and

ω_2,

$$E(r,t) = E_1 e^{-i\omega_1 t} + E_2 e^{-i\omega_2 t} + c.c \tag{3.10}$$

$$= A_1 e^{ik_1 r - i\omega_1 t} + A_2 e^{ik_2 r - i\omega_2 t} + c.c. \tag{3.11}$$

is incident on a crystal with nonlinear optical properties, the contribution to the total polarisation from the second order component is given by

$$P^{(2)}(t) = \chi^{(2)}[\underbrace{E_1^2 e^{-2i\omega_1 t}}_{\text{i) SHG}} + \underbrace{E_2^2 e^{-2i\omega_2 t}}_{\text{ii) SHG}} + \underbrace{2E_1 E_2 e^{-i(\omega_1+\omega_2)t}}_{\text{iii) SFG}} \tag{3.12}$$

$$+ \underbrace{2E_1 E_2 e^{-i(\omega_1-\omega_2)t}}_{\text{iv) DFG}} + c.c.] + 2\chi^{(2)}[\underbrace{E_1 E_1^* + E_2 E_2^*}_{\text{v) OR}}] \tag{3.13}$$

The first two terms oscillate at a frequencies of $2\omega_1$ and $2\omega_2$. These result in generation of radiation at frequencies twice that of the input waves, termed second harmonic generation (SHG). The third term produces radiation of frequency $\omega_1 + \omega_2$, referred to as sum-frequency Generation (SFG). The fourth term results in a wave of frequency $|\omega_2 - \omega_1|$ difference frequency generation (DFG), and the final two terms which have no time dependence correspond to optical rectification (OR).

For the case of sum-frequency generation, the polarisation component oscillating at frequency $\omega_3 = \omega_1 + \omega_2$ results in production of a third wave

$$E_3 = A_3 e^{ik_3 z - i\omega_3 t}, \tag{3.14}$$

the amplitude of which is described by the equation

$$\frac{dA_3}{dz} = \frac{2i\chi^{(2)}\omega_3^2 A_1 A_2}{k_3 c^2} e^{i(\Delta k)z}, \text{ where } \Delta k = k_3 - k_1 - k_2, \tag{3.15}$$

providing the amplitudes of the input beams A_1 and A_2 change only by a negligible amount, and that generation rate of A_3 is slow. After travelling through a nonlinear material of thickness L, the total intensity of the SFG beam is given by

$$I_3(L) = K^2 L^2 \frac{\sin^2(\Delta k L/2)}{(\Delta k L/2)^2}, \text{ with } K^2 = \frac{8(\chi^{(2)})^2 \omega_3^2 I_1 I_2}{n_1 n_2 n_3 \epsilon_0 c^2}, \tag{3.16}$$

where I_i is the intensity of beam i and n_i is the corresponding refractive index.[27]

The amplitude of the SFG signal is maximised when $\Delta k = 0$, ie. $n_3 k_3 = n_1 k_1 + n_2 k_2$. This is known as the phase matching condition and can be achieved in crystals with birefringent properties. For the case of a negative uniaxial crystal such as β-barium borate (BBO) used in this thesis, type I phase matching is achieved when the

high frequency component has extraordinary polarisation, while the two input beams have ordinary polarisation. The angle of the crystal can be varied until $\Delta k = 0$.

The photoluminescence upconversion experiment is effectively an optically gated photodetection system. The photons detected are those produced by the SFG process in the nonlinear crystal, and since the SFG process can only occur when the short (100 fs) laser pulse is present at the same time as the PL signal pulse, the crystal effectively acts as an optical gate which is open when the laser (gate) pulse is present, and closed when the gate pulse is absent.

As the intensity of the output pulse is proportional to the intensity of each of the input pulses, the time-profile of the entire PL pulse (at a frequency ω_2) can be mapped by measuring the intensity of the SFG product as a function of the time-delay between sample PL and laser pulses. This is shown schematically in Figure 3.3. Spectral resolution is afforded by the phase-matching condition, and the frequency spectrum of the PL pulse at any given time-delay can be measured by synchronously scanning the nonlinear crystal and detection wavelength.

The time resolution of the upconversion experiment is limited by the width of the gate pulse and dispersion effects in the nonlinear crystal. For the system described here, the time resolution is approx 300 fs when a 1 mm thick BBO crystal is used. Sharper time-resolution can be achieved by using thinner BBO crystals, however the signal-to-noise ratio of the experiment will be reduced.

Although high time-resolution is advantageous, because each additional 1 m in beam path length corresponds to $\sim$3 ns delay, the measurement of long (> 1.5 ns) signal pulses is difficult to realise. The TCSPC technique is an electronically gated process which is suitable for measurement of PL over these longer time frames.

3.2.2 Time Correlated Single Photon Counting

The TCSPC technique is an indirect method of measuring the temporal shape of a photoluminescence pulse signal by detecting a single photon, measuring the detection time and building up a statistical representation of the pulse shape. The output from a pulsed laser consisting of a regularly spaced train of pulses is split into two beams, one of which is detected by a fast photodiode and acts as a reference signal for timing, and the other used to excite the sample. Photoluminescence is collected and detected by a single photon counting device, in this thesis either a photomultiplier tube (PMT) or an avalanche photo-diode (APD). The power of the beam exciting the sample is

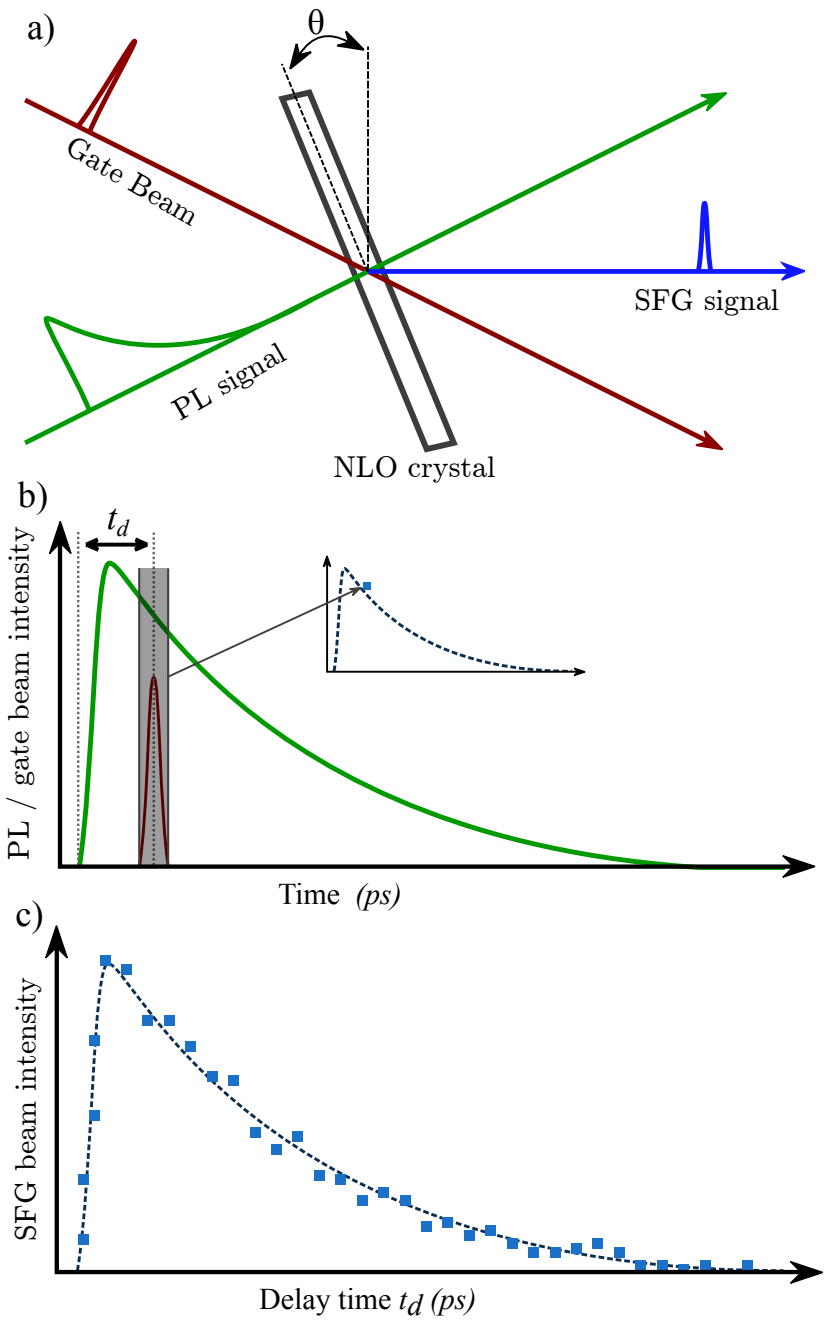

Figure 3.3: Schematic description of the upconversion measurement. a) The gate beam and PL beams are focussed onto the centre of a nonlinear crystal (BBO), and a third beam of SFG photons is produced. The angle of the crystal θ is varied in order to meet the phase-matching condition. b) As the gate pulse (red) is much shorter in duration than the PL pulse, the output generated at any given delay t_d will be proportional to a small part of the total PL pulse. c) Varying the time delay between the two pulses allows the entire PL pulse to be mapped out. The light blue squares are the integrated SFG beam intensity at various time delays, and the dashed blue curve is the original PL pulse.

set low in the TCSPC experiment, such that the probability of a single photon being detected per pump-decay cycle is $\ll 1$, and therefore the signal out from the APD is a series of randomly and widely spaced pulses, while the photodiode measures a regular series of pulses straight from the laser. The output from both of the photodiode and APD detectors are sent to a TCSPC counting card (Becker & Hickl SPC400) in a computer.

In the case of a photon being detected, the detection time t_d is determined relative to the previous reference pulse and a single count is added to a memory bin allocated to a window in which t_d lies. If no photon is detected in any given cycle, the next reference pulse resets the timer. Since the detection probability is proportional to the PL intensity at any given time, after many repetitions a distribution of counts versus detection time is built up, corresponding to the real PL pulse shape. This is shown graphically in Figure 3.4. As the counter is reset each time two reference pulses are detected without any photon being detected, the maximum time window for measuring a PL pulse is determined by the laser repetition rate. For the 80 MHz mode-locked MaiTai, this corresponds to a 12.5 ns time window. The use of a pulse picker or alternative lasers with a lower repetition rate, eg. gain switched diode lasers described in Section 3.1.2 are two methods of extending the measurable range.

Since the detection time is determined by the arrival time of the PMT/APD output pulse rather than the output pulse width, time resolution is determined by the variation in time between photon absorption and output pulse rather than the actual pulse width of the detector. The former is generally shorter than the latter, and can be as low as 35 ps for avalanche photodiodes such as the Single-Photon Avalanche Photodiode (SPAD) from Micro-Photon Devices (MPD) used for the work described in this thesis.

The signal to noise ratio of the TCSPC experiment is good, scaling as $\sqrt{N}$ where N is the peak count number. This is due to the fact that a single count is added to the memory bin per photon detection event, and is independent of the signal amplitude from the PMT/APD detector.

As mentioned above, the probability of a single photon being counted per pump-decay cycle needs to be $\ll 1$ for the TCSPC experiment. This is required in order to avoid error in measured intensities and distortions of the measured decay curve. This restriction is imposed on the photon count rate by two effects: the dead-time of the system and pile-up effects.[20] The dead-time of the system is a time window following

each photon detection event in which no further photons can be detected, and arises due to the method by which the time between a photon detection event and the next reference pulse is converted into a digital signal. This results in a discrepancy between the real and measured signal intensity. Pile-up effects arise from the fact that only one photon can be detected per cycle, and hence the measured fluorescence lifetime is artificially shortened as the signal intensity increases, as only those photons detected early in the pump-decay cycle are recorded. Both of these effects can be avoided by restricting the photon count rate to around 0.1 % of the reference count rate. For the Ti:Sapphire laser system used in this thesis, this corresponds to a count rate of approximately 10^5 cps.

3.3 PLUC/TCSPC System

The system used for most of the PL upconversion and TCSPC measurements described in Chapters 4 and 5 is shown in Figure 3.5. The output of the pulsed MaiTai laser can be used to excite the sample and gate the PL directly, or if a pump energy outside the range 690–1040 nm (345–520 nm by frequency doubling), the output from an optical parametric oscillator (OPO, Spectra Physics Inspire 100) can be used instead.

For operation without the OPO, the output beam from the laser is adjusted to the table working height (20 cm) by a periscope and then split into two parts by a polarising beam-splitter cube. The ratio of power in each beam is adjusted by the achromatic $\lambda/2$ waveplate positioned directly before the beamsplitter cube. The undiverted beam is directed via two mirrors mounted on an automated translation stage. The final starred mirror in the gate beam path is removed for the upconversion experiment, such that the beam continues along path A and is directed and focussed by a single mirror and lens onto a BBO crystal mounted on an automatic rotation stage. The detection optics are kept inside a black box in order to minimise detection of stray room light. For the TCSPC measurement, the final mirror is replaced and the beam travels along path B to a fast photodiode. The output from this photodiode is relayed to the TCSPC counting card and is the reference pulse train described in Section 3.2.2.

The diverted beam is condensed onto a second BBO crystal tuned to maximise second harmonic generation from the input beam. Any residual long-wavelength laser light is removed by a second Glan-Thomson polariser and short-pass absorptive

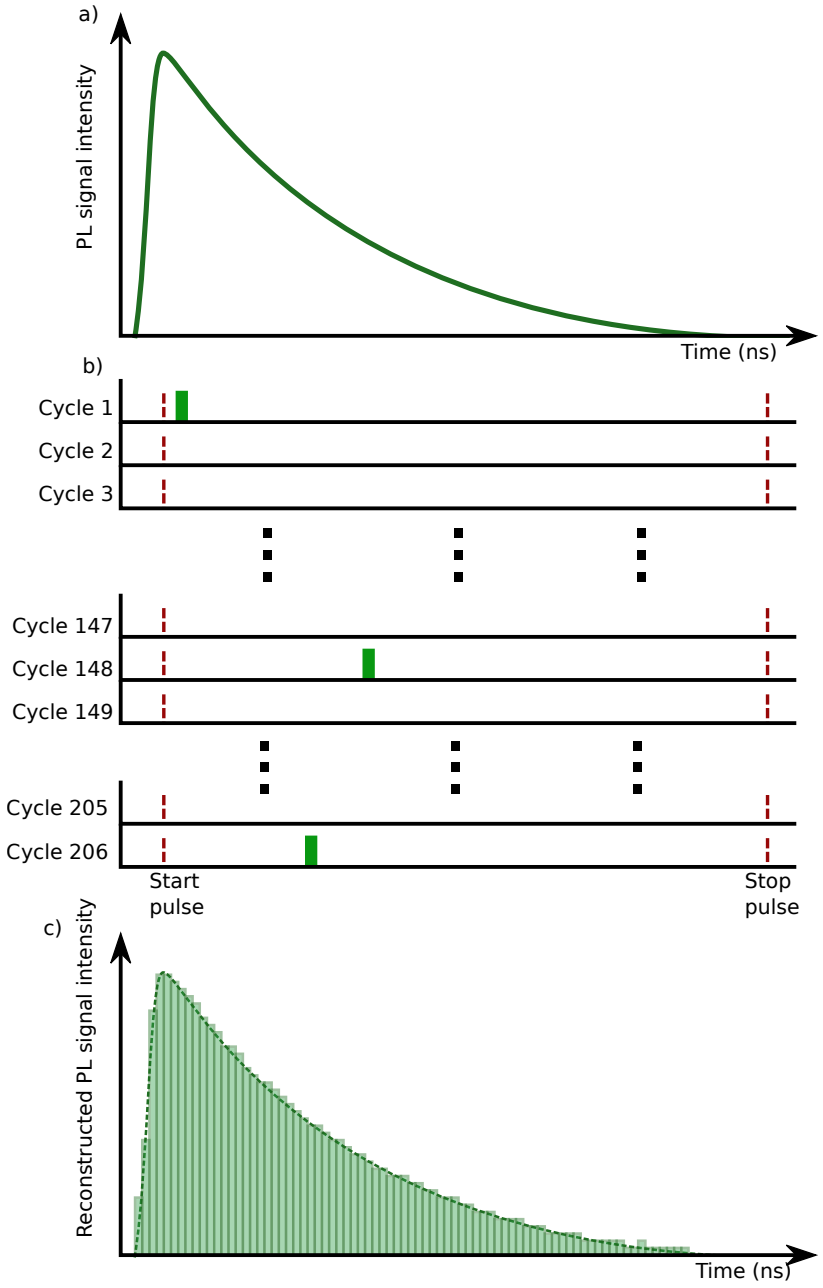

Figure 3.4: Description of the time correlated single photon counting technique. a) The real sample PL pulse shape. b) The time after excitation (measured relative to the gate pulses incident on the photodiode) are different each cycle, and in many cycles, no PL photons are detected whatsoever, in order to reduce pile-up effects described in Section 3.2.2. c) After many cycles, a distribution of counts versus detection time is built up, replicating the signal PL shape (dashed line).

filter (Schott Glass BG39). This pump beam is then directed toward the sample position via a $\lambda/2$ waveplate and a third Glan-Thomson polariser in order to set the polarisation of the pump beam and control the average power. It is focussed by a 25 mm focal length lens onto the sample position. The emitted PL is collected and focussed onto the BBO crystal by two off-axis parabolic mirrors. These are used rather than glass optics to minimise chirp of the PL pulse. Scatter of the pump beam from the sample and its holder is removed by a long-pass filter in front of the box. For the upconversion experiment, the angle of the BBO crystal is adjusted to maximise upconversion efficiency of the PL at the required frequency. The SFG photons are collected, collimated and focussed onto the entrance slit of a monochromator (Jobin-Yvon Triax) and measured on a liquid nitrogen cooled CCD (Symphony). A pinhole and band-pass filter (Schott glass UG11 or UG1) are used to block unconverted PL, gate beam photons, and light at twice the gate beam frequency generated by SHG in the BBO crystal.

For the TCSPC measurement, the BBO crystal is replaced with a polariser, and the output from the monochromator is directed onto either a large-area photomultiplier tube (Hamamatsu PMC-100-20, 230 ps instrument response) or small-area silicon avalanche photodiode (Micro Photon Devices SPD-050-CTE, 35 ps instrument response).

If the excitation wavelength required lies outside of the range accessible with the laser alone, the OPO can be used. The MaiTai is tuned to 820 nm output and the mirror between the laser and OPO removed. Additional mirrors (marked with stars) are added or removed to direct the OPO depleted fundamental beam and signal, SHG or idler output along the gate and pump beam paths respectively.

3.4 Crystal Angle Calibration

The efficiency of the SFG process depends critically on the angle of the crystal axes relative to the polarisation and propagation direction of the input gate and sample PL beam. For a time resolved measurement at a single PL wavelength, this can be optimised by rotating the crystal until the integrated CCD signal is maximised, with the monochromator central wavelength set to λ_{det}, where $1/\lambda_{\mathrm{det}} = 1/\lambda_{\mathrm{PL}} + 1/\lambda_{\mathrm{gate}}$. Measurement over a range of wavelength values requires calibration of the rotation stage angle over the range of interest and will differ according to the gate beam wavelength and crystal cut angle. This is done by replacing the sample PL with

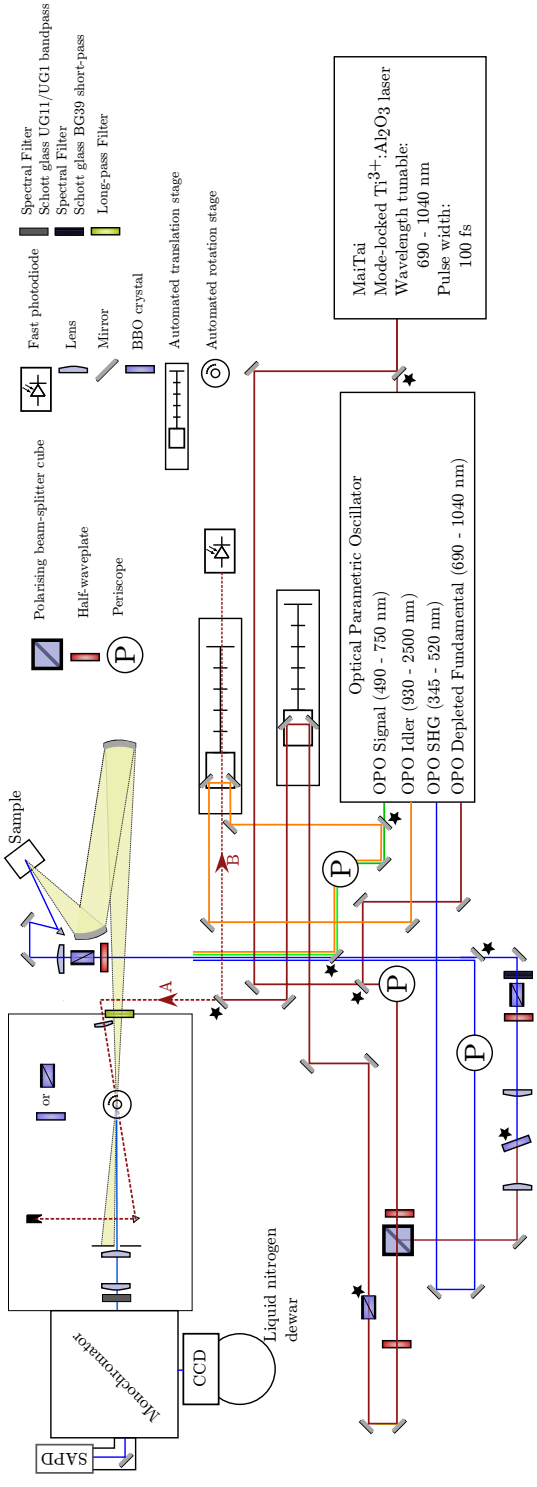

Figure 3.5: Experimental set-up for photoluminescence upconversion spectroscopy and TCSPC. The beam paths A and B are those taken by the gate beam for the PLUC and TCSPC experiments respectively. Optics marked with a star are secured with removable magnetic bases to allow for quick conversion between experiments using either the OPO or the MaiTai as the laser source.

white light from an incandescent bulb with known irradiance. The monochromator is tuned to the appropriate wavelengths for SFG over the range of interest at $\sim 25\,\text{nm}$ intervals and for each wavelength the integrated CCD counts versus crystal angle are measured. The centre point θ_E of each distribution can be determined by fitting the data points with a Gaussian curve. The crystal angle for any given input PL wavelength for a fixed gate pulse energy is then determined by fitting the points with a polynomial. An example of the calibration for a gate wavelength of 900 nm and BBO crystal cut at $\theta = 30°$, $\phi = 0°$ is shown in Figure 3.6.

$$\theta(E_{PL}) = P_0 + P_1 E_{PL} + P_2 E_{PL}^2 + P_3 E_{PL}^3 \tag{3.17}$$

For time resolved PL spectra, the measured spectrum is a product of the real PL spectrum $f(\lambda)$ modified by the spectral resonse of the system

$$I_{obs}(\lambda) = f(\lambda) * g_{UC}(\lambda), \tag{3.18}$$

where $g(\lambda)$ depends on the crystal angle, absorption profile of the long pass filter and band pass filters used, and the spectral response of the monochromator and CCD. The measured upconversion spectrum is given by

$$I_0 * g_{UC} = I_{obs} - I_{gate} - I_{bulb} + I_{dark}, \tag{3.19}$$

where I_0 is the known spectral irradiance, I_{obs} is the measured upconversion spectrum, I_{gate} is the background signal when the white light source is turned blocked and only the gate beam is present, I_{bulb} is the white light source alone, and I_{dark} is the background with both beams blocked. Similarly, for time integrated photoluminescence spectra and time resolved spectra obtained by TCSPC, the spectral response of the system can be calculated by

$$I_0 * g = I_{obs} - I_{dark}. \tag{3.20}$$

3.5 Data Analysis – IRF Deconvolution

For any time resolved PL detection method, the measured trace is always broadened by the finite width of the pump pulse and the resolution of the detection method. For a general decay process $g(t)$, the observed decay curve is a convolution of $g(t)$ with the Instrument Response Function (IRF) $f(t)$, such that

$$f_{obs}(t) = (f * g)(t) = \int_0^t f(t')g(t - t')dt'. \tag{3.21}$$

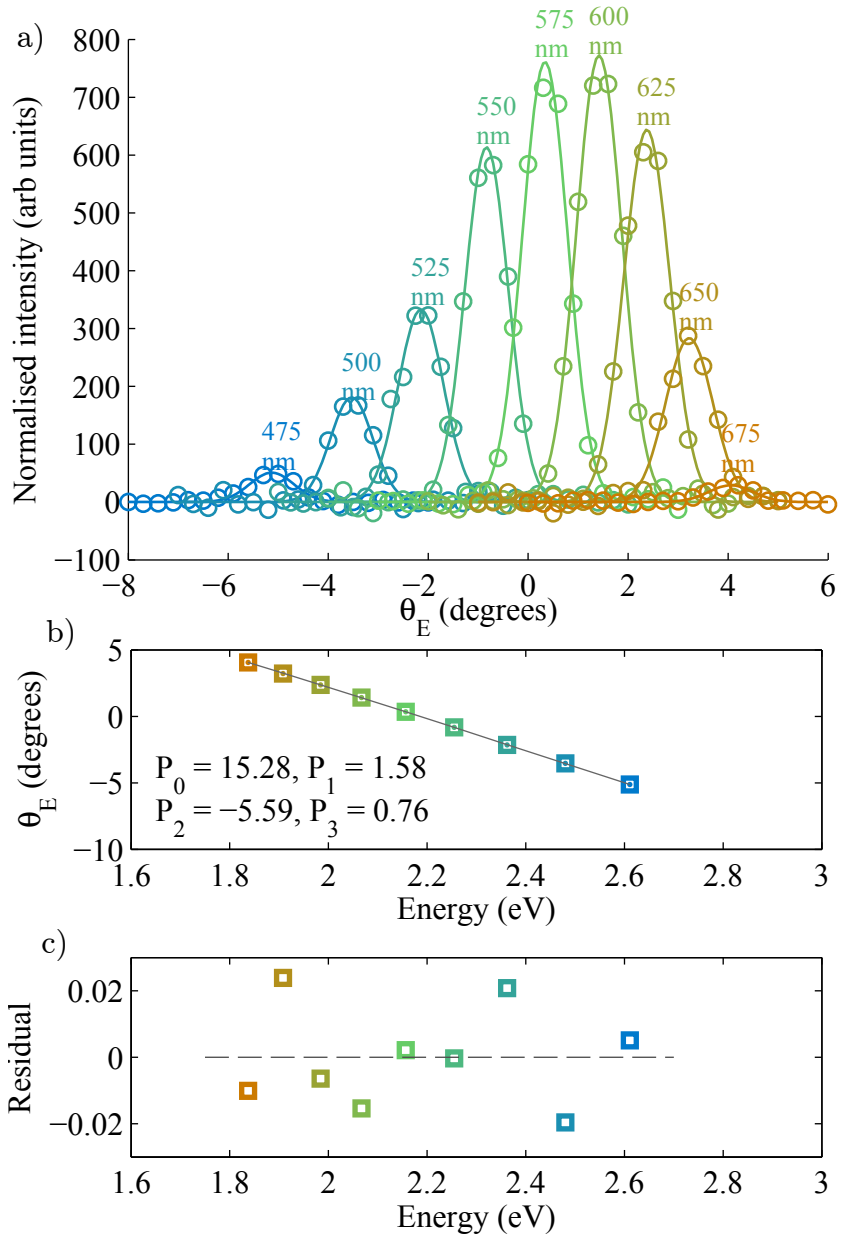

Figure 3.6: Crystal calibration routine: a) Measurement of upconversion intensity versus crystal angle for input PL wavelength between 450 nm and 675 nm with 900 nm wavelength gate beam and fitting each with a Gaussian curve to find the crystal angle at the peak. b, c) Fitting the peak energy versus crystal angle (Eq. 3.17 and residuals.)

For the results presented in this thesis, when fitting time resolved data the general form of the function $g(t)$ is known and the fit parameters are determined by iterative reconvolution using a non-linear regression fitting routine. For each iteration of the fitting algorithm, the convolution of an experimentally determined IRF and the function $g(t)$ is calculated and compared with the data. The parameters x of $g(t)$ are varied in order to minimise the sum of the squares of the difference between the function and data points

$$S = \sum_{i=1}^{N} [f_{obs;i}(x,t) - y_i]^2. \tag{3.22}$$

The IRF is measured by by replacing the sample with a blank, roughened substrate and tuning the output of the laser or OPO to the sample PL wavelength. The long pass filter in the sample PL beam path is replaced with a neutral density filter and a TCSPC trace measured. The filter ensures the count rate of the scattered photons is at least three orders of magnitude lower than the laser repetition rate in order to avoid pile-up effects.

The observed function can be obtained from the measured IRF and model function by

$$f_{PL}(t) = F^{-1}[F(f(t))F(g(t))], \tag{3.23}$$

where $F(f(t))$ and $F(g(t))$ are the discrete Fourier transforms of the experimental IRF and model function respectively, or by replacing the integral in Equation 3.21 with a sum and evaluating f_{PL} directly. The use of the fast Fourier transform algorithm to calculate f_{PL} is much quicker than direct computation, but depends strongly on the level of noise in the measured IRF.

Chapter 4

Rapid Intramolecular Energy Tranfer in D–A–D Triad Dyes

4.1 Introduction

Luminescent solar concentrators (LSC)[227;82;136] are a separate class of concentrator devices based on a luminescent material embedded in a transparent lightguide. Incident light is absorbed and then re-emitted at longer wavelengths, with a large proportion of the re-emitted light carried to the edges of the guide by total internal reflection where it is coupled out to PV cells distributed around the edges.[19] In general, the intensity of light at the edges relative to that incident on the front surface is much smaller than the surface to edge ratio of the device. This is a result of the many loss sources associated with LSC, summarised in Figure 4.1.[55] Of these, three of the largest loss mechanisms are incomplete absorption across the solar spectrum by the luminescent material (5a), self absorption losses during transit from the original absorber and the lightguide edge (2), and escape from the front surface which is not internally reflected (1).

Attempts to address the first of these issues have been made by using stacks of multiple layers, each absorbing over a different part of the spectrum,[82] or multiple dyes in the same film.[82;13] In order to direct photoluminescence away from the surface, an anisotropic distribution of luminophores is crucial.[56;151] Anisotropic dye distribution results in a larger fraction of the emitted photoluminescence (PL) being directed toward the edges of the lightguide and away from the surface, reducing escape losses,[222;162] while energy transfer between donor and acceptor units on the same molecule reduces self-absorption losses as has been recently shown.[214] A donor-acceptor-donor triad dye with two unsubstituted perylene bisimide (PBI) donors and

one bay-substituted PBI acceptor in a collinear arrangement was incorporated into a switchable liquid crystal (LC) host. The elongated shape of the triad molecule enabled facile alignment with the LC host, while the 2:1 ratio of donors to acceptors means that self absorption effects could be minimised without compromising on incident light absorption.

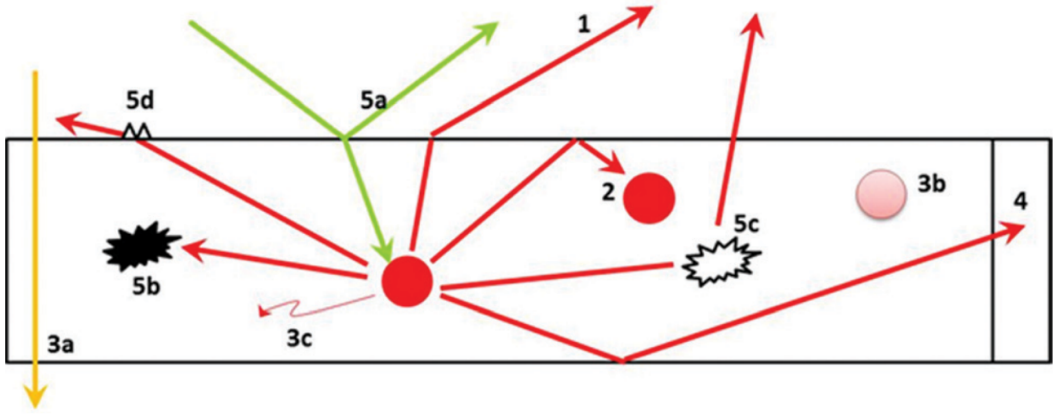

Figure 4.1: The mechanism of operation of a Luminescent Solar Concentrator. In ideal device, all incident photons (green ray) will be absorbed by the luminophores (red circles), and all emission will be directed to the coupled photovoltaic unit. Loss sources in real devices are: 1) Light emission outside of capture cone, not reflected internally; 2) Re-absorption of photons during transit; 3a) Incomplete absorption by embedded luminophores; 3b) Deactivation of embedded luminophores; 3c) Non-unity quantum efficiency of luminophores; 4) Photovoltaic cell losses; 5a) Reflection from the waveguide surface; 5b) Parasitic absorption by the waveguide; 5c) Scattering by waveguide defects; 5d) Surface scattering. (Taken from: Debije and Verbunt, 2012)

In PBI the dipole moment of the S_1 transition is aligned along the long axis of the perylene unit.[182;43] Thus when the linear triad dyes are all aligned with the LC host there is very little absorption of light polarized perpendicular to the long molecular axis. Incorporating a second dye which shows the same efficient intramolecular energy transfer from donor to acceptor units but has orthogonal donor and acceptor S_1 transition dipole moments would enable more complete absorption of incident light with any polarization, while further lowering self-absorption losses. Such an arrangement, however, would be expected to show very low energy transfer rates from a simple Förster model.

In this chapter, a triad dye is studied, in which switching of photoluminescence polarization along with exceptionally fast excitation energy transfer (EET) is observed, in contrast to predictions of the Förster model. The photophysics of the D–A–D triad

in which D/A dipole moments are orthogonal are compared with those of a triad in which the dipole moments are collinear. Rapid energy transfer ($\tau \approx 1\,\text{ps}$) and strong PL anisotropy was observed in both molecules when the donor units are selectively excited. The broad absorption across much of the visible spectrum of these two dyes, along with the efficient energy transfer and PL polarization switching makes these dyes ideally suited to use in LSC devices.

4.2 Experimental

For time-resolved photoluminescence measurements, solutions of the dyes **TH**, **TL** and **A** (see Figure 4.2) were prepared by dissolving the purified dye powder in chloroform solvent at concentrations of around $1 \times 10^{-4}\,\text{M}$ in a quartz cuvette with path length 1 mm. Energy transfer rates and time resolved spectra were measured using the fluorescence upconversion technique described in Chapter 3. The MaiTai laser was tuned to 900 nm, 100 fs pulse duration. The laser fundamental was used as the gate beam in the upconversion experiment, and the sample solutions were excited by the frequency doubled beam. Dilute solutions with optical density at the maximum absorbance of < 0.1 OD steady state photoluminescence measurements in order to minimise distortion of the emission spectrum by self-absorption effects. Steady state PL spectra were measured using a spectrally calibrated fluorimeter (Horiba Florolog). Time resolved PL decays ($\sim$ns timescales) were measured with a PicoQuant Pico Harp 300 commercial TCSPC system. Samples were excited with the pulsed output of a 450 nm diode laser (LDH-P-C-450) powered by a picosecond pulsed diode laser driver (PDL 820) with pulse duration of 200 ps FWHM and a repetition rate of 16 MHz.

The *Photoluminescence Quantum Yield* of the triad dyes **TH** and **TL**, and the three reference dyes **DH**, **DL** and **A** was recorded using an integrating sphere (Newport 70682NS) with the technique described by Mello *et al.*[54] Solutions of each dye in chloroform were excited with the attenuated tunable output of an optical parametric oscillator (Inspire HF 100). PL emission and pump intensities were measured with a spectrally calibrated CCD and spectrometer which was fibre coupled to the exit port of the integrating sphere. Absolute quantum yield values of the dyes were cross checked against a solution of known quantum efficiency, cresyl violet in ethanol.[146]

DFT calculations were performed with the NWChem 6.3 package[220] for Linux on a computer with an Intel Core i7-3770 CPU and 32 GB RAM. Ground state ge-

ometries were optimized at the B3LYP/6-31G* level. Calculations were carried out to assess the extent and energies of the frontier molecular orbitals. In order to reduce computation time, only one donor and the central acceptor unit of the triad dye **TH** were included, as the donor units at either end of the triads are idential, and it is the degree of direct electronic interaction between D/A units which is of primary interest. The phenoxy groups at the bay positions of the acceptor unit were replaced with methoxy groups and the alkyl chains attached to the carboximide N atoms were replaced with methyl groups in order to further reduce computation time. The ground state geometry was optimized at the B3LYP/6-31G* level for the both the "flat" and "twisted" molecules and the extent and energy of the frontier molecular orbitals were then calculated.

4.3 Results and Discussion

4.3.1 Steady State PL Spectroscopy

The dyes reported in this chapter are based on a central bay-substituted perylene bisimide, directly linked to either two benzoperylene tris-imides[127] or two unsubstituted perylene bisimide units. Bay substitution lowers the energy of the $S_{1\leftarrow 0}$ transition relative to the unsubstituted dye (see **A** as compared to **DL** in Figures 4.3 and 4.4), allowing the central unit to act as an acceptor and the outer two units as donors in energy transfer processes and minimising re-absorption by the donor units of any PL emitted by the acceptor in the LSC. In addition, bay substitution increases solubility and ease with which these and similar dyes can be incorporated into a host matrix, making them promising for use in LSC.[114;57;53] The molecular structures of the two triads (**TH**, **TL**) are shown in Figure 4.2, along with the structures of the donor and acceptor reference molecules (**DH**, **DL**, **A**).

Since for each of the donors and the acceptor the lowest lying optically active transition has a dipole moment polarized along the long (N–N) axis of the perylene bisimide backbone,[182;43] the dye with benzoperylene donors is referred to as the H-shaped triad (**TH**) due to the orthogonal arrangement of these transition dipoles, while the triad with collinear transition moments is referred to as the linear triad (**TL**).

Figure 4.3 shows the optical absorption spectra of **TH** and **TL** triad dyes in solution. The lowest energy 0–0 peaks located at 465 nm (**TH**, **DH**), 527 nm (**DH**)

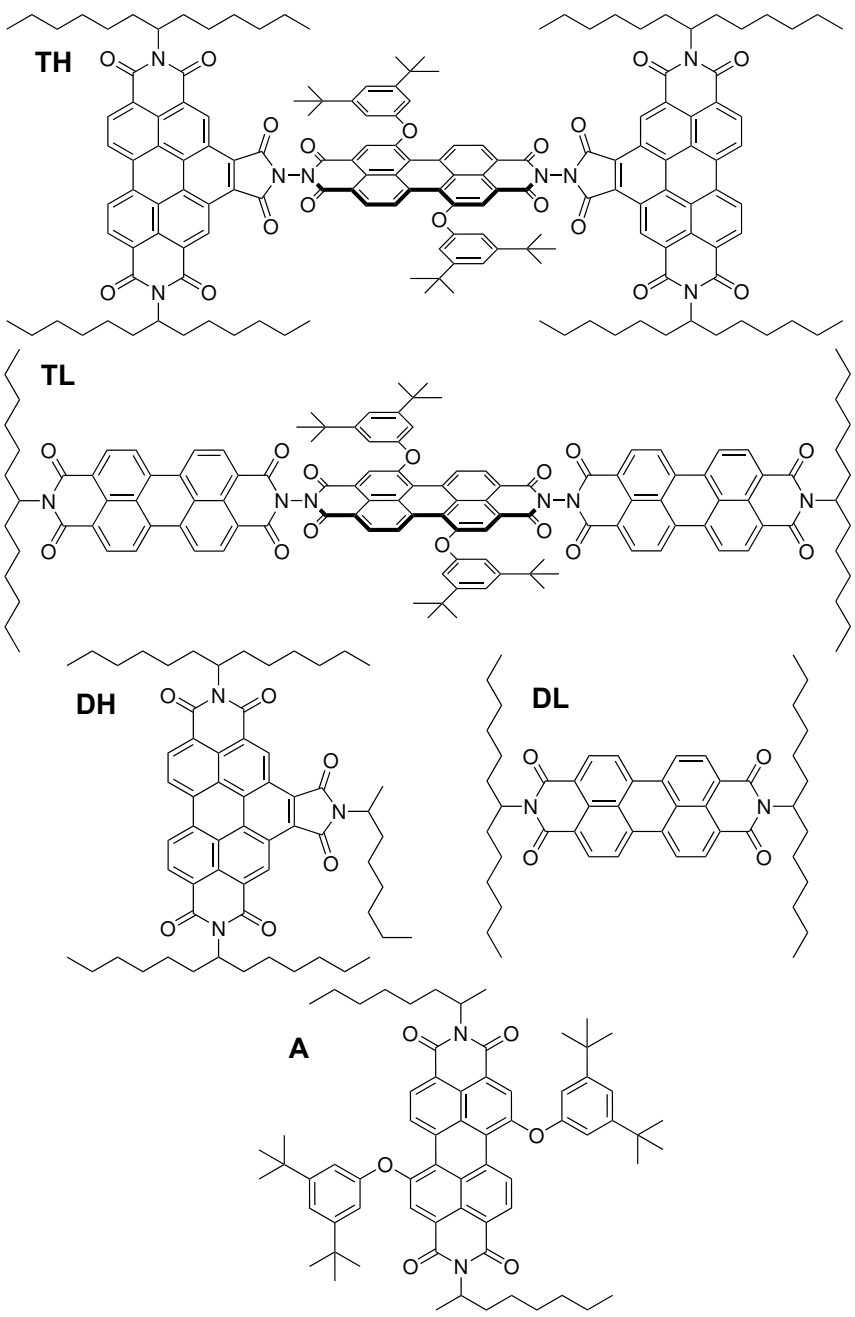

Figure 4.2: The chemical structures of the 5 dyes used in this chapter. Dyes **TH** and **TL** are the H-shaped and linear donor-acceptor dye triads, dyes **DH** and **DL** are their respective donor moieties, and dye **A** is the acceptor perylene bisimide common to both. *Materials synthesised and purified by J. ter Schiphorst.*

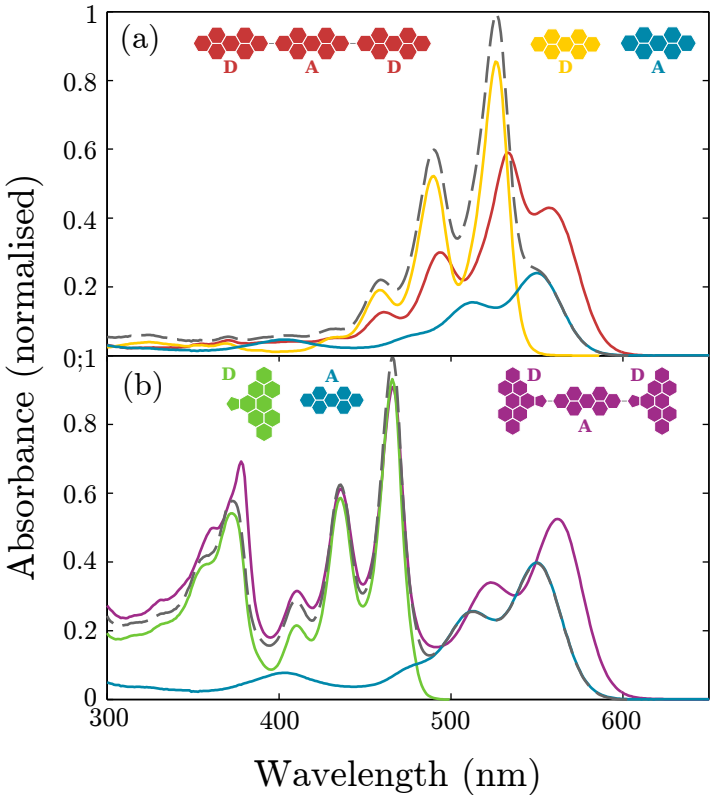

Figure 4.3: Absorption spectra of a) dyes **TL**, **DL**, and **A**; b) dyes **TH**, **DH** and **A** in $CHCl_3$, normalised to the sum of the donor and acceptor absorbance. Solutions of triad dyes **TH** and **TL**, and **A** had a concentration of 10 µM whereas **DH** and **DL** were at 20 µM. Spectra were recorded with a Perkin Elmer Lambda 1050 spectrophotometer. The solid lines are the experimentally measured data and the dashed grey line in each case is the linear combination of the individual dye and acceptor spectra.

and 550 nm (**A**) correspond to $S_{1\leftarrow 0}$ transitions with dipole moment along the long axis of the perylene bisimide unit.[182;43] Higher energy transitions located around 375 nm in **TH** and **DH** have an associated transition dipole moment perpendicular to the PBI long axis, and involve the attached benzene and bisimide functional groups of the donor unit.[2]

For these absorption measurements, solutions of the triad dyes and acceptor monomer were prepared at a concentration of 10 µM, and those of the donor monomers at 20 µM. Therefore, the overall concentration of donor and acceptor units was the same in all cases, whether they were part of a triad or free in solution. As a result, the linear sums of the donor and acceptor spectra as shown in Figure 4.3 by the grey dashed lines would be expected to match the spectra of the triad dyes in the absence of any direct electronic coupling between subunits. In reality however, a strong de-

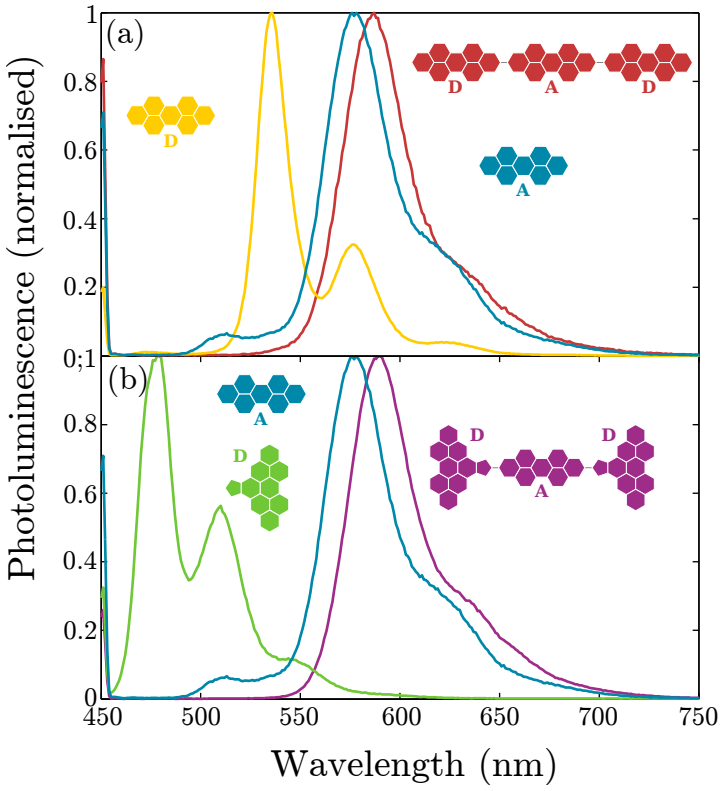

Figure 4.4: Normalised time-integrated photoluminescence spectra of a) dyes **TL**, **DL**, and **A**; b) dyes **TH**, **DH** and **A** in dilute $CHCl_3$ solution. Spectra were recorded with a spectrally calibrated Horiba Florolog, with CW excitation of wavelength 450 nm.

gree of coupling between subunits is observed; both donor and acceptor absorption peaks are red-shifted relative to those of the isolated molecules. In particular, the peaks corresponding to $S_{1\leftarrow 0}$ transitions of the donor and acceptor units in the **TL** are red-shifted by approximately 43 meV and 30 meV respectively, compared to the reference molecules **DL** and **A**. In the H- shaped triad **TH**, the donor $S_{2\leftarrow 0}$ and acceptor $S_{1\leftarrow 0}$ transitions are red-shifted by 36 meV and 51 meV, while the donor $S_{1\leftarrow 0}$ peak remains unchanged. A strong degree of electronic coupling is also evident in the steady-state photoluminescence spectra (Figure 4.4) as the emission peak of the acceptor incorporated into the triads **TL** (**TH**) is red-shifted by 31 (42) meV relative to the isolated acceptor.

4.3.2 Time Resolved PL Spectroscopy - Spectra

The rate of energy transfer occurring in the triads was investigated by probing both the donor and acceptor emission intensity after selective excitation of the donor sub-

unit. Time- and polarization-resolved photoluminescence spectra and transients were recorded with sub-picosecond resolution using the photoluminescence upconversion technique as described in Chapter 3. Concentrated solutions (4×10^{-4} M) of dyes **TH** and **TL** were each excited with the frequency doubled output of a Ti:sapphire laser at 450 nm. The high solution concentration was required in order to maximise the temporal resolution of the system, and avoid broadening of the PL signal by the finite path length (1 mm, corresponding to 6.6 ps) of the cuvette. The excitation wavelength was set to 450 nm as there is a minimum in the acceptor unit absorption spectrum at this wavelength allowing for preferential excitation of the donor subunits (at 450 nm, the total donor absorption is 5.4 and 3.2 times that of the acceptor in dyes **TH** and **TL** respectively, see Fig 4.3). Figure 4.5 shows the normalised time-resolved PL spectra for both triads at times ranging from 0.1 to 100 ps after excitation, while the insets show the unscaled PL data.

For **TH**, emission from the donor unit centred at 510 nm can be observed immediately after excitation which rapidly decays while the acceptor emission increases. Even at short times (0.1 ps) after initial excitation there is considerable acceptor emission, which may arise from ultrafast energy transfer or some residual direct acceptor excitation. The red-shift of the main acceptor PL peak during and after the decay of the donor emission is assigned to solvent reorientation and relaxation processes.[126] A lowering in energy of the peak emission by 50 meV over the same 100 ps window is also observed in the isolated acceptor in solution (see Figure 4.5c and Figure 4.6). Similar trends are observed for **TL**, although here the donor emission is spectrally not as well resolved as it occurs closer in energy to that of the acceptor unit and hence appears as a shoulder on the blue-end of the peak. Visual inspection however suggests that energy transfer is even faster for **TL**.

4.3.3 Time Resolved PL Spectroscopy - Transients

The rate of excitation energy transfer can be determined by following the emission intensity after excitation at a wavelength specific to either the donor or the acceptor. Figure 4.8a shows the decay of the PL from donor and acceptor units following preferential excitation of the donors at 450 nm. For each of the two triads, rapid quenching of the donor emission is observed, resulting from efficient EET with a rate of $k_1 = 8.3 \times 10^{11}\,\mathrm{s}^{-1}$ ($\tau_1 = 1.2$ ps) for **TH** (a similar transfer rate was reported in related D-A dyad molecules[164]) and a faster rate of $k_2 = 1.6 \times 10^{12}\,\mathrm{s}^{-1}$ ($t_2 = 0.6$ ps)

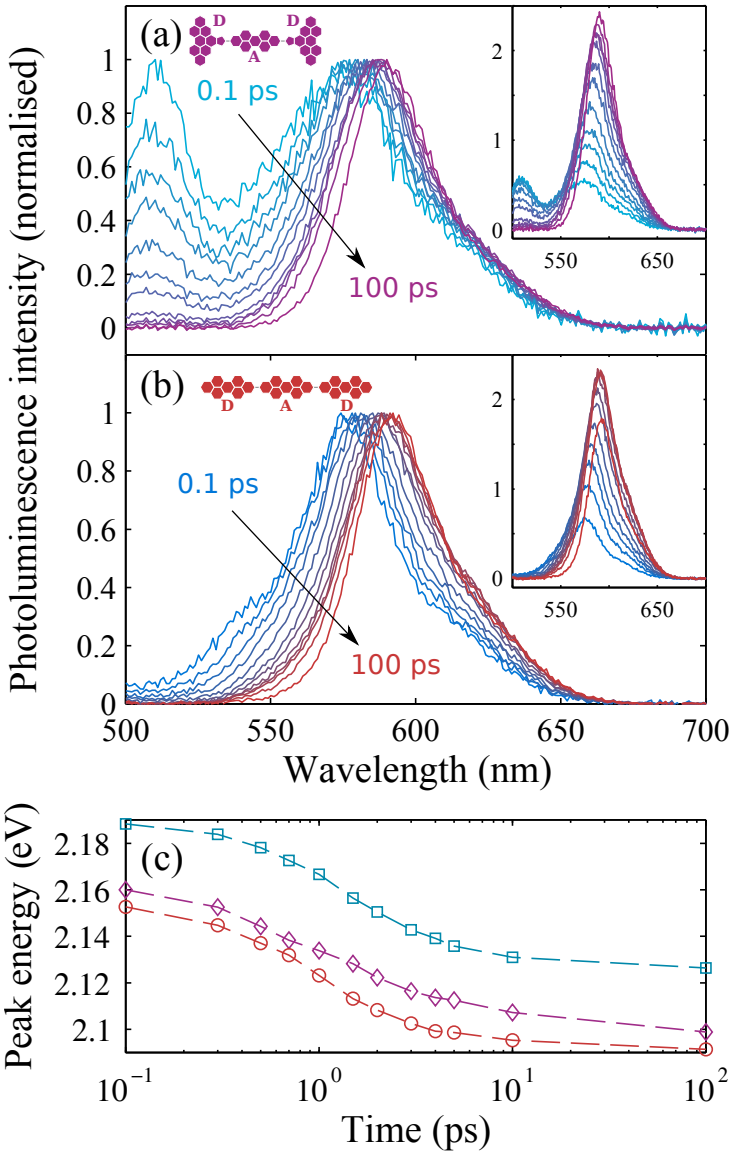

Figure 4.5: (a,b) The time resolved PL spectra of dyes **TH** and **TL** at 4×10^{-4} M in $CHCl_3$ at short times (0.1 to 100 ps) after excitation. The main plot shows the normalised time resolved PL, while the insets show the raw data. Each spectrum was corrected for the spectral response of the system. (c) Peak emission energy as a function of time after excitation for triad dyes **TH** (diamonds) and **TL** (circles), and **A** (squares) as a reference. The normalised and raw PL upconversion spectra for **A** are shown in the Figure 4.6.

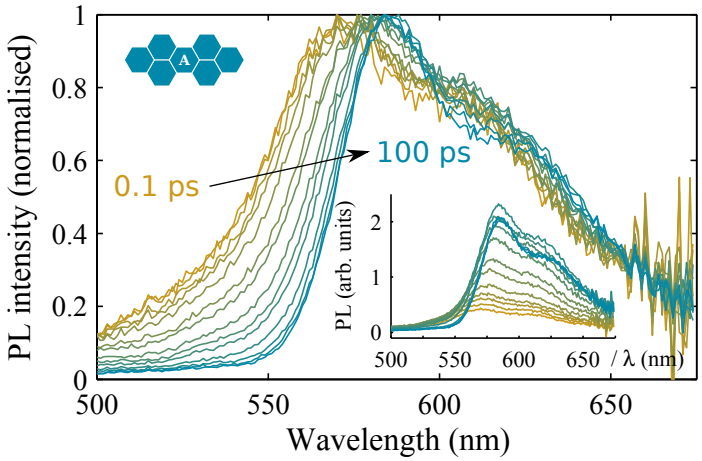

Figure 4.6: (a,b) The time resolved PL spectra of the acceptor dye **A** at 4×10^{-4} M in $CHCl_3$ at short times (0.1 to 100 ps) after excitation. The main plot shows the normalised time resolved PL, while the inset show the raw data. Each spectrum was corrected for the spectral response of the system.

for **TL**. These values were extracted by fitting the data with a mono exponential decay convoluted with the instrument response function taking into account the spatial excitation profile in the cuvette.

To investigate whether such ultrafast energy transfer induces a change in the direction of the oscillator dipole moment, the transients of the emission intensity with polarization parallel ($I_{\parallel}$) and perpendicular ($I_{\perp}$) to the polarization of the excitation beam were recorded separately. From these data, the time-dependent PL anisotropy r can be derived as usual, using $r = (I_{\parallel} - I_{\perp})/(I_{\parallel} + 2I_{\perp})$, with the result displayed in Figure 4.8b. The use of a polarized excitation beam will result in preferential excitation of only those molecules with absorption transition moment collinear with the polarization.[219] For a system of randomly oriented molecules with perfectly aligned absorption and emission dipole moments, an initial PL anisotropy of 0.4 is expected as a result.[219;175] However, for a system in which all emission dipole moments are perpendicular to the molecular absorption moments, an anisotropy of -0.2 is to be observed.[219] Hence for the linear PBI triad **TL**, excitation of solely the donor, followed by complete energy transfer to the acceptor, is expected to yield a value of close to $r = 0.4$ for perfect alignment of the coupled donor and acceptor dipole moments. On the other hand, a value of $r = -0.2$ would be associated with a polarization flip by 90° on transfer. However, these values may in reality be modified by the presence of direct acceptor absorption and imperfect dipole alignment.

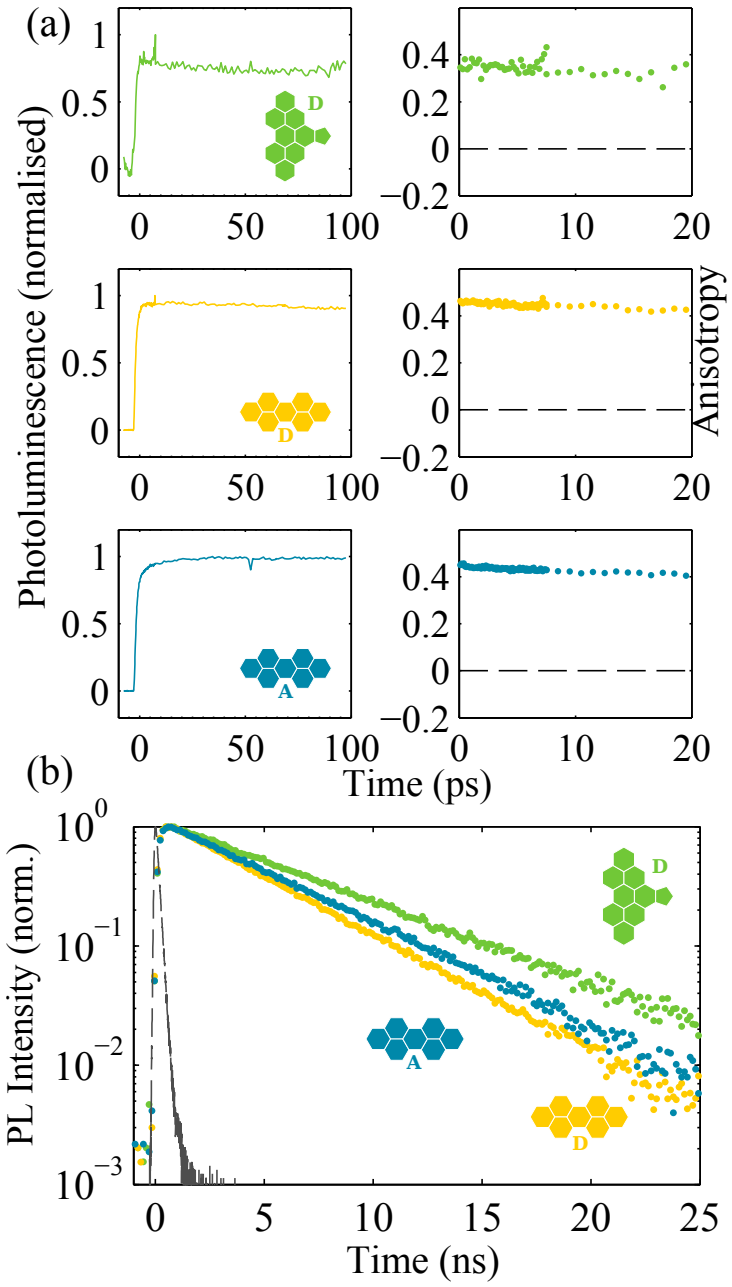

Figure 4.7: (a) Time resolved photoluminescence measured by PL upconversion at 530 (**DH** and **DL**), and 620 nm (A), along with the calculated PL anisotropies for each of the 3 individual donor and acceptor units. (b) Time resolved photoluminescence transients measured by TCSPC for donor and acceptor reference dyes **DH**, **DL**, and **A**. The instrument response function is also included for reference (grey dashed line). All samples were measured in $CHCl_3$ solution. The pump beam was vertically polarized and the polariser in the detection beam path was set to the magic angle (54.7°).

For the H-shaped triad **TH**, the PL anisotropy of the acceptor emission rapidly falls to a stable value of -0.05, indicating a significant rotation of polarization between absorption and emission dipole moments (Fig. 4.8b). If a perfect 90° angle was held between the transition dipoles of the donor and acceptor subunits, a final anisotropy of -0.10 would be expected when taking into account the fraction of direct acceptor excitation derived from the relative absorptivity of the subunits at 450 nm. The observed value of -0.05 is higher than this, and would be commensurate with an angle of 72° between dipole moments,[219] suggesting that the long axes of adjacent PBI units in **TH** may not be perfectly perpendicular.

The PL anisotropy of the linear triad **TL** has a starting value of 0.4 at time $t = 0$, partly influenced by some direct excitation of the acceptor, then decays to a stable value of 0.32 upon EET. These data demonstrate that the emission dipoles of the subunits in this dye are aligned and polarization is mostly retained on EET, although as is the case with **TH** this alignment appears to be slightly imperfect.

Dye	τ_d (ps)[a]	τ_a (ps)[b]	PLQY [c]
TH	1.96[†] (510)	4260 (590)	0.66 (460)
			0.75 (515)
			0.8 (525)
TL	1.05[†] (510)	4220 (590)	0.52 (450)
			0.62 (490)
			0.67 (525)
DH	6300 (510)	–	0.20
DL	4400 (580)	–	0.86
A	–	5000 (580)	0.72

Table 4.1: [a,b]Decay constants as determined by fitting a monoexponential decay to the tail of the PL spectra of each of the 5 dyes as measured by TCSPC. The short and long wavelengths correspond to emission detected from the donor and acceptor subunits respectively. Values in parentheses are the detection wavelengths in nm of the PL trace from which each PL lifetime was extracted. [†]The approximate timescale of energy transfer from donor to acceptor as determined by fitting a bi-exponential decay model to the short lived PL with wavelength of 510 nm. [c]PLQY determined from solutions of each dye in $CHCl_3$ with an accuracy of ± 0.05. Values in parentheses are the excitation wavelength in nm.

This is in sharp contrast to the polarisation anisotropy of the three reference dyes **DH**, **DL**, and **A**, all of which are ≈ 0.4 and remain high over the time scale of the measurement, as can be seen in Figure 4.7a. This is consistent with excitation and emission along a single transition dipole. The recorded value of > 0.4 for the linear donor and acceptor materials is due to a systematic errors of the measurement. The

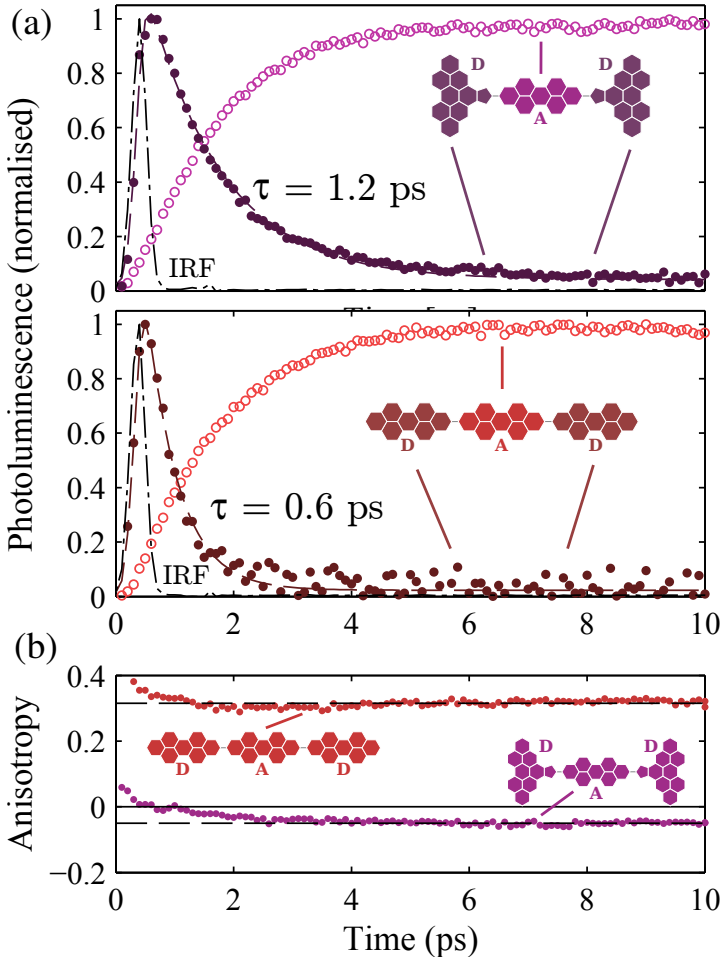

Figure 4.8: (a) Total PL intensity and (b) PL anisotropy as a function of time after excitation for the triads **TH** and **TL** in $CHCl_3$. In each case, the solid (empty) circles show the PL and anisotropy measured at 510 nm (620 nm). The dashed lines are lifetime fits with a monoexponential decay, convoluted with the instrument response function (dot-dash line). Lifetimes of $\tau = 1.2$ ps and $\tau = 0.6$ ps were determined for **TH** and **TL** respectively. The point of $t = 0$ for the PL anisotropy was defined as the time at which the normalised PL intensity was unity. The excitation wavelength for both measurements was 450 nm and the dyes were at a concentration of 4×10^{-4} M in $CHCl_3$.

absolute PL intensity measured is sensitive to alignment, which must be re-optimised between measurements of the emission polarised perpendicular and parallel to the excitation polarisation.

4.3.4 Energy Transfer Modelling

From the perspective of Förster EET theory[76;75] the ultrafast energy transfer observed for **TH** is highly surprising, given that the transition dipoles for emission and absorption of the donor and acceptor units are expected to be fairly orthogonal. In Förster's model, energy transfer is mediated by a Coulombic interaction between transition dipole moments on the donor and acceptors at a rate k, given by:

$$k = \frac{9000(\ln 10)\kappa^2 \Phi_D J_{DA}}{128\pi^5 n^4 N_A \tau_D |\mathbf{R}_{DA}|^6}, \tag{4.1}$$

where Φ_D is the fluorescence quantum yield of the donor, τ_D is the radiative lifetime of the donor emission, N_A is Avogadro's constant, n is the refractive index of the medium ($n = 1.446$ for $CHCl_3$), and $|\mathbf{R}_{DA}|$ is the distance between the donor and acceptor point dipoles associated with the transitions. The orientation factor, κ is given by

$$\kappa = \boldsymbol{\mu}_A.\boldsymbol{\mu}_D - 3(\boldsymbol{\mu}_A.\mathbf{R}_{DA})(\boldsymbol{\mu}_D.\mathbf{R}_{DA}), \tag{4.2}$$

where $\boldsymbol{\mu}_A$ and $\boldsymbol{\mu}_D$ are the unit vectors of the transition dipole moments on the donor and acceptor respectively, and $\mathbf{R}_{DA}$ is the unit vector along the line connecting the two. J_{DA} describes the degree of overlap between the normalised donor emission and acceptor extinction coefficient as

$$J_{DA} = \int_0^\infty F_D(\lambda)\varepsilon_A(\lambda)\lambda^4 d\lambda. \tag{4.3}$$

For a system in which the transition dipoles of the donor and acceptor are orthogonal to each other and to the vector connecting them, a value of $\kappa = 0$ is obtained, and hence energy transfer is absent. One key assumption is that the transition dipoles on the two units involved in EET can be modelled as point dipoles, that is, they are small compared to the separation between them. In dyes such as the triads investigated here this is obviously not the case, as both the length of the perylene bisimides and the separation between them are on the order of 1–2 nm.

To assess whether such electronic wavefunction delocalisation can account for the observed ultrafast energy transfer in **TH** it is useful to compare experimentally extracted rates to a suitably modified version of Förster theory. There are several

methods of accounting for the comparable length scales of separation and transition density extension, including the line-dipole,[229] distributed-monopole,[97] and transition density cube[125] models. These models are applicable to cases with very-weak coupling between chromophores such as **TH**, in which there is no shift of the donor S_1 peak positions despite the close proximity of donor and acceptor.[142] Here a two-dimensional variation of the line-dipole model was used, in which coupling between local transition densities in the plane of the donor and acceptor molecules is considered. The transition density on the donor and acceptor was approximated as the ground state of a 2-D particle in a box, and split into N_i and N_j subunits μ_i and μ_j as depicted schematically in Figure 4.9a. A sum over the interaction between each element of the total dipole moments was incorporated into the EET model such that the transfer rate k_{2D} is given by[21;229;188]

$$k_{2D} = \frac{9000(\ln 10)\Phi_D J_{DA}}{128\pi^5 n^4 N_A \tau_D} \left[\sum_{i,j}^{N_i,N_j} \left| \frac{\mu_i \mu_j \kappa_{ij}}{|\mathbf{R}_{ij}|^3} \right| \right]^2 , \tag{4.4}$$

where μ_i and μ_j are the transition dipole moment elements, κ_{ij} is the orientational factor between subunits, as given in Eqn. 4.2, and $\mathbf{R}_{ij}$ the distance between the midpoints of the interacting elements.

The calculated energy transfer rates are shown in Figure 4.9b for **TH** (top) and **TL** (bottom).

The energy transfer rate (k_{FRET}) as a function of the number of elements along the long and short axes of the donor unit (N_i) are plotted for each with dashed lines included as a guide to the eye

For a value of $N_i = 1$, Equation 4.4 reduces to the simple Förster model – here, an energy transfer of identically zero is obtained for dye **TH** assuming orthogonal transition dipole moments. For any number of elements $N_i > 1$ however, rapid energy transfer on the order of $(20\ \mathrm{ps})^{-1}$ for **TH** and $(0.15\ \mathrm{ps})^{-1}$ for **TL** are predicted, highlighting the importance of taking the spatial extent of the transition dipoles into account.

For the linear triad, **TL**, the model predicts an energy transfer rate of $(0.15\,\mathrm{ps})^{-1}$, which is comparable to the experimentally determined transfer rate of $(0.6\,\mathrm{ps})^{-1}$. For the H-shaped triad, **TH** however, the predicted value of $(26\,\mathrm{ps})^{-1}$ is more than an order of magnitude slower than the experimental value of $(1.2\,\mathrm{ps})^{-1}$. PL anisotropy measurements discussed above indicated that the angle between donor and acceptor transition dipole moments on **TL** (**TH**) may have not be fully aligned (orthogonal).

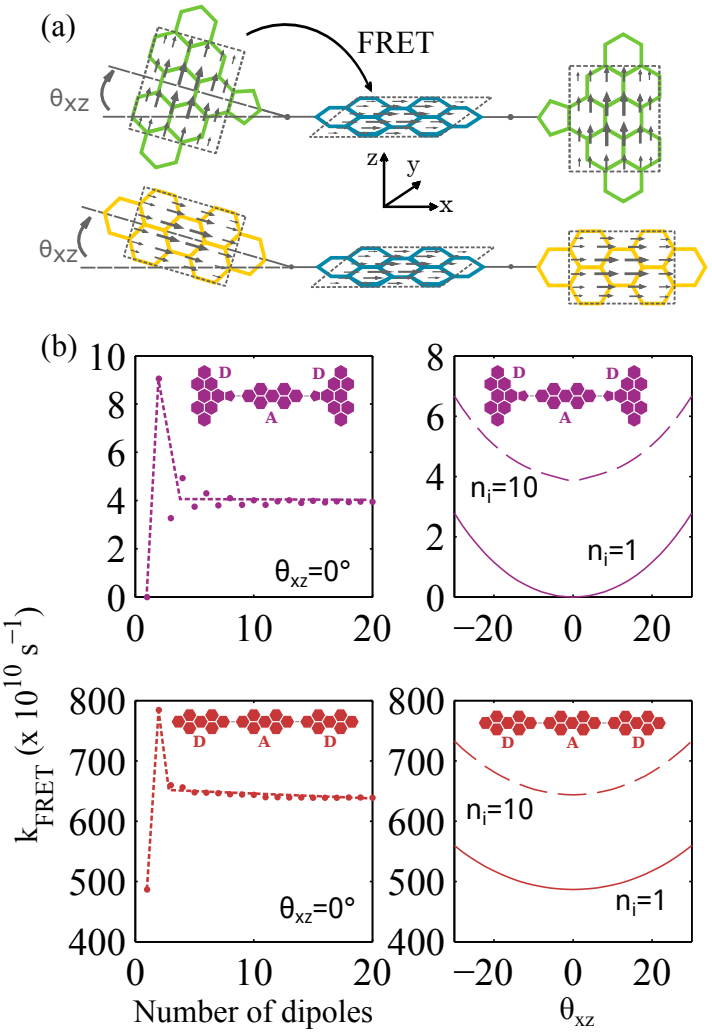

Figure 4.9: (a) Schematic representation of the FRET model of energy transfer between Donor and Acceptor in dyes **TH** and **TL**. Dipole transition moments within each chromophore were those from a 2D PIB model, and bending in the D-A bond was introduced by pivoting about the bond mid-point in the x-z plane. (b) The calculated energy transfer rate (x $10^{10}\,s^{-1}$) as a function of the number of dipoles included along the long-axis (left) and the bending angle (right). The dashed lines in the left hand-side plots are included as a guide to the eye.

The impact on energy transfer of torsions and bending around the N–N bond were therefore also investigated. The energy transfer rate was calculated as a function of the bending angle θ_z of this bond (Fig 4.9b, right hand side). Here, the number of elements along the long axis of the perylene unit was set to $N_i = 10$ in order to allow a compromise between the adequate representation of the continuously distributed wavefunction and the limitations imposed by computational speed. For **TH**, even a relatively large bending angle of 20° between donor and acceptor units only increases the energy transfer rate very slightly up to $(24\ \text{ps})^{-1}$, which is still far slower than the experimentally observed value. Therefore, while electronic wavefunction delocalisation and bond bending may account for a large extent of unusually fast energy transfer in the H-shaped triad, a significant discrepancy remains that cannot be accounted for by simple through-space dipole-dipole coupling or by a Frenkel-exciton/vibronic model.[164]

It is proposed therefore that through-bond energy transfer between the strongly electronically coupled donor and acceptor units has a significant contribution to the overall EET in the H-shaped triad. Energy transfer in covalently bound donor–acceptor systems has been studied extensively,[76;75;112;60;141;191;199;98;129;164;187;225;237] and both through-space contributions mediated by electronic multipole coupling,[76;75] and through-bond mechanisms which depend on orbital overlap between the two units[60] have been shown to play a role. For perylene monoimides and bisimides, the location through which donor and acceptor units are linked has a strong impact on the degree of through-bond electronic coupling which can occur.[225;237] When linked through the 9-position of the perylene, extensive conjugation throughout the entire molecule and an absorption spectrum strongly different to those of the constituent chromophores were observed.[225] In contrast, when the PBI unit was linked to the same acceptors through the imide nitrogen the two units were found to be electronically independent of each other.[237] This difference in behaviour has been attributed to the presence of nodes in the frontier molecular orbitals centred on the nitrogen atom in PBI.[128]

The H-shaped triad **TH** investigated here also has donor and acceptor units connected at the imide nitrogens, however there are several pieces of evidence pointing towards through-bond electronic coupling making a contribution to the unexpectedly rapid energy transfer. First, there is a significant deviation between models based on through-space EET and the observed transfer rates, even when the short sepa-

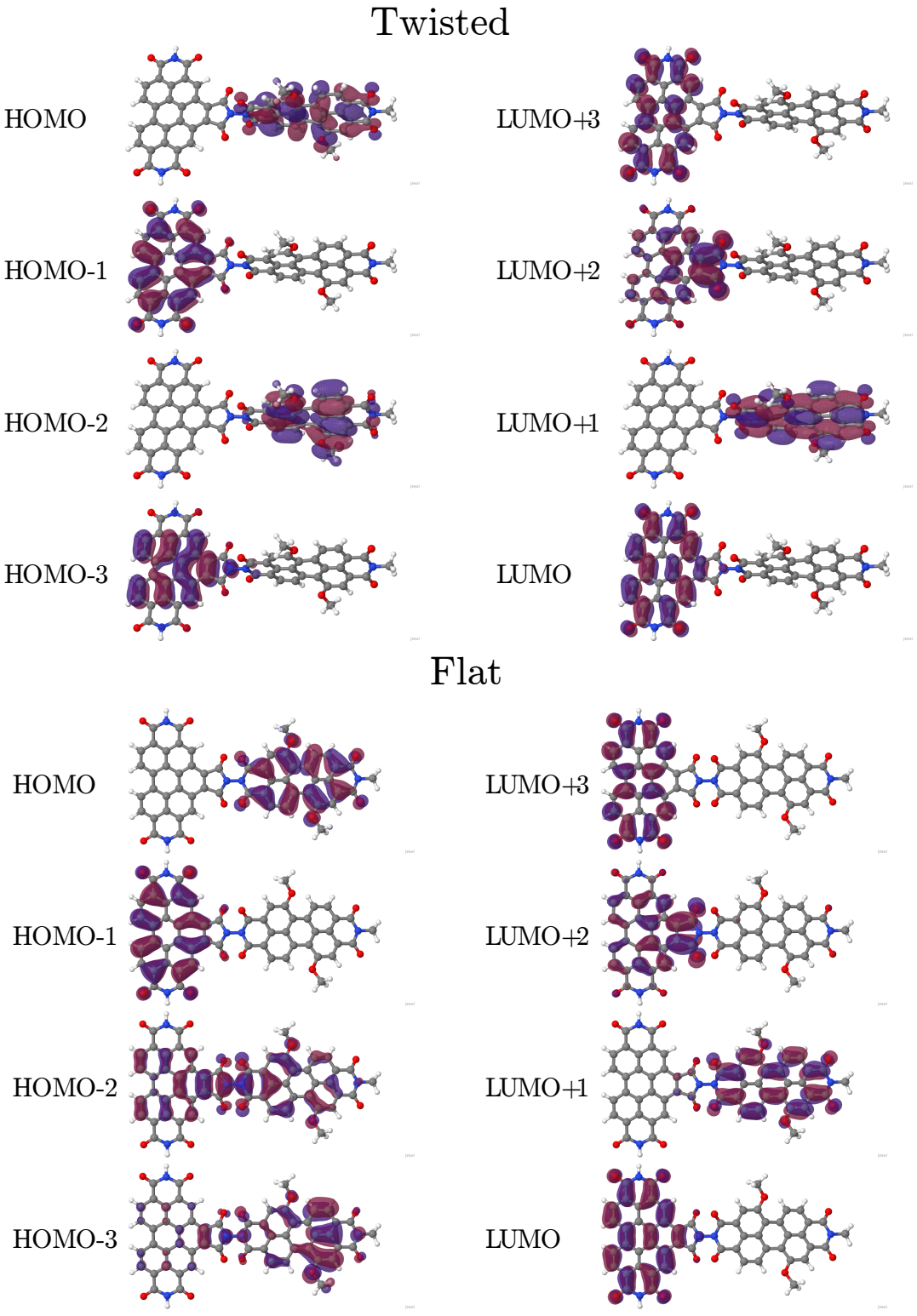

Figure 4.10: Frontier molecular orbitals for the HOMO-3 to LUMO+3 energy levels in flat and twisted D-A dyads. The geometry of both the flat and twisted conformers were optimised at the 6-31G*/BLYP level.

ration between donor and acceptor units is taken into account. Second, the strong bathochromic shift of the donor $S_{2\leftarrow 0}$ and acceptor $S_{1\leftarrow 0}$ transitions of the triad relative to the isolated donor and acceptor dyes, as evident from absorption and emission spectra (see Figure 4.3). If the interaction between the two states on the donor and acceptor components were solely excitonic, as in a hetero J-dimer, a blue-shift in donor transition energy and a decrease in the absorption strength of the transition would be expected, along with an increase in the strength and decrease in the energy of the acceptor transition,[9;113] however both a red shift and increase in transition strength is observed for both the donor and acceptor transitions. Third, although the acceptor is linked through the imide nitrogen at the end of the perylene subunit, the donor unit is not. For a coplanar configuration of the donor and acceptor subunits therefore there is some delocalisation across the entire molecule in several of the orbitals involved in optical transitions (see molecular orbitals from DFT calculations.[220] Figure 4.10). Direct electronic coupling may therefore be enabled by torsions about the N–N linking bond.[101;98] Hence a combination of through-space energy transfer facilitated by electronic wavefunction delocalisation, supplemented by through-bond energy transfer, allows for an ultrafast energy transfer in **TH** that is accompanied by a switch in polarization.

4.4 Conclusion

In conclusion, the dynamics of energy transfer and polarization switching for two compound perylene bisimide triad dyes have been investigated, and these dyes show excellent potential for use in luminescent solar concentrator devices. For both triad dyes, highly efficient energy transfer from donor to acceptor moieties is shown to occur within less than 2 ps. For the orthogonally arranged H-shaped triad, the observed rates are in sharp contrast with the Förster point-dipole model which predicts an absence of energy transfer in this geometry. The observed fast rates are shown to arise from a combination of through-space energy transfer between delocalised electronic electronic states, and through-bond energy transfer, mediated by bond-bending and torsions. In each of the triad dyes, there is an effective energy downshift which reduces self-absorption, while giving excellent control over emission polarization. Embedding such triads in a liquid crystal host should result in efficient, switchable LSC devices with low self-absorption and surface losses.

Chapter 5

Effect of Nanocrystalline Domains on Benzodithiophene Based Donor-Acceptor Co-Polymers

5.1 Introduction

Organic photovoltaic devices have high potential as a low-cost, renewable energy source[122] and have attracted wide-spread research interest in recent years, as they are lightweight, flexible, and can be processed from solution. Devices typically incorporate mixtures of electron-accepting and -donating materials in order to induce the separation of the initially generated charge-neutral state (molecular exciton) at the interface between the two materials.[213] Since this model was reported, a large number of OPV devices incorporating type-II heterojunction systems have been produced,[213] and rapid advances in power conversion efficiencies have been achieved. Devices based on thin films processed directly from solution mixtures (so-called bulk heterojunction films, BHJ[240]) of π-conjugated polymers and fullerene derivatives now reach power conversion efficiencies of up to 10%.[92] In these polymer:fullerene systems, high device efficiencies are only obtained after extensive optimization of fabrication conditions, which strongly affect the morphology of the BHJ films.[246] On the one hand, intimate mixing of donor and acceptor materials promotes efficient exciton diffusion to the donor-acceptor interface at which charge transfer can occur. On the other hand, extended crystalline networks are beneficial for efficient charge dissociation[88] and collection.[47] Forming an ideal BHJ requires careful balancing of these processes, and hence small variations in molecular structure, molecular weight, polydispersity, and processing conditions can have significant effects on the overall

efficiency.[246] Such effects have been particularly well documented for the benchmark system of poly-3-hexylthiophene (P3HT) blended with the fullerene derivative phenyl-C_{61}-butyric-acid-methyl-ester (PCBM), for which high power conversion efficiencies (PCE) of 6%[132] have been reached in photovoltaic devices. However, P3HT in many ways represents a highly special case as in its regio-regular form it has the strong tendency to form extended crystalline structures of π-stacked polymer chains.[117] Such crystalline domains result in a high PCE immediately after device fabrication, but extended thermal annealing and/or illumination under full solar conditions (AM1.5) results in phase segregation of the polymer and fullerene components.[231] This process can be minimized somewhat by using P3HT with lower regio-regularity, which has a lower tendency to crystallize.[64] Likewise, the formation of crystalline PCBM needles on extended thermal annealing causes similar drops in device efficiency which can be mitigated by using modified fullerenes with bulkier substituents than PCBM.[244]

In the quest for higher photovoltaic device efficiencies, donor-acceptor (D-A) copolymers have increasingly been employed as hole transporters.[138] Here, the conjugated coupling of electron-donating and accepting units on the same chain allows a lowering of the band gap energy and therefore an increase in light absorption and photocurrent.[32] Several of the recently developed D-A copolymers show that the lessons learnt from the case of P3HT are not necessarily applicable to all polymer:fullerene solar cells. For example, blends of PCDTBT (carbazole/dithieno-benzothiadiazole co-polymer) and PCBM result in devices with maximum PCE immediately after deposition, without any further processing. Any thermal annealing of these devices results in a decrease in chain ordering and a reduction in PCE.[22] Another study demonstrated that in a series of thiophene/quinoxaline copolymers, the highest fill factors and PCEs were associated with polymers with the most disordered and twisted backbone that showed the lowest tendency to crystallize.[224] In addition, a fluorinated polymer PBnDT-FTAZ (benzodithiophene/5,6-difluoro-2,1,3-benzothiadiazole copolymer) with low crystallinity was found to yield photovoltaic devices in which the short-circuit current (J_{SC}) and fill-factor were insensitive to a doubling of the polymer and fullerene domain sizes.[215] The discrepancy in the trend between device efficiency and crystallinity between P3HT and the more recently developed D-A copolymer materials may be partly understood given that P3HT allows the formation of particularly extended ordered domains or pure polymer when blended with PCBM,[117] along with regions of pure PCBM and regions of mixed polymer:PCBM.

While large crystallite formation may aid charge mobility in some polymer systems relative to the amorphous polymer phase, the formation of many small ordered regions may prove detrimental because the increasing surface area of the domain boundaries between crystalline and amorphous polymer regions can act as a barrier to charge transfer and promote charge trapping and recombination.[200] Whether device efficiencies increase or decrease with overall film crystallinity should therefore depend on whether the in-domain charge-extraction enhancement or trapping at the domain boundaries is dominant, which in turn is influenced by the crystallite surface-area to volume ratio.

This chapter presents results of a study into the interplay between crystallite domain formation and performance in photovoltaic BHJ thin-film devices for a series of donor-acceptor copolymers based on benzodithiophene (BDT) donor and benzothiadiazole (BT) acceptor groups. Thin-film morphology and inter-chain interactions were examined using wide-angle X-ray scattering, atomic force microscopy and absorption/emission spectroscopy. It was found that increased crystallinity of the neat polymer film is associated with lower photovoltaic device efficiencies in BHJ films with $PC_{60}BM$, in agreement with the notion that domain boundaries are impeding performance in this system. The exciton diffusion length in neat films of the polymers was determined by measuring the diffusive quenching of excitons at an interface acting as an electron acceptor, in this case compact TiO_2. For the polymer exhibiting the highest degree of crystallinity diffusion lengths of 7.4 nm were observed, while for a polymer film with low crystallinity, a value of only 4.0 nm was recorded. However, measurements of the photoluminescence quenching in polymer:PCBM films indicate that the majority of excitons reach a charge-dissociating interface within about 1 ps after light absorption for all polymers examined. Therefore, exciton diffusion to and dissociation at the BHJ interface does not appear to be a limiting factor in these systems, suggesting that the observed differences in crystallinity predominantly derive from the subsequent steps of charge transport and recombination. It can be seen that for the polymers exhibiting thin films with high crystallinity, chain aggregation is already evident prior to casting, for solution at temperatures below ∼60 °C. For D-A copolymers with moderate to low solubility, casting conditions from solution and the subsequent crystallite formation are hence likely to have a substantial impact on photovoltaic device performance.

5.2 Experimental Methods

UV-vis absorbance spectra of polymer films and solutions were measured with a Perkin-Elmer Lambda 9 UV-Vis Spectrophotometer. Wide Angle X-ray Scattering (WAXS) patterns were taken using a Panalytical XPert Pro, with Cu anode (K_α= 0.154 nm). Atomic Force Microscopy (AFM) images were used to assess the surface topography and surface roughness of the polymer films. All measurements were performed with a Veeco Dimension Icon AFM in tapping mode. Photoluminescence (PL) spectroscopy was carried out both in time-resolved and time-integrated (TI) mode. Samples were excited by the frequency-doubled output of a Ti:Sapphire oscillator with 80 MHz repetition rate and 100 fs pulse duration. For measurements with sub-picosecond (∼350 fs) time resolution, the PL up-conversion (PLUC) method was employed, while time-correlated single photon counting (TCSPC) was used for higher-sensitivity, lower-resolution measurements as described in Chapter 3.

For temperature-dependent solution measurements, polymer solutions were held in a quartz cuvette on a home-built temperature controlled stage. For thin-film measurements, samples were held in a dynamic vacuum below 10^{-5} mbar to avoid photodegradation. Excitation pulse fluences of 3 µJ cm^{-2}, 0.3 µJ cm^{-2} and 0.03 µJ cm^{-2} were used for the solid state PLUC, solid state TCSPC and solution phase TCSPC measurements respectively. *The polymers used in this study were synthesised by S. Tierney of Merck Chemicals.*

5.3 Sample Preparation

As doctor-blading is impractical on the small quartz substrates used for the PL and WAXS measurements, drop-casting was used to prepare samples with as similar a film morphology to the final devices as possible. The drop-cast films were prepared of either neat polymer, by heating 10 mg ml^{-1} solutions, or of polymer:PCBM blends, by heating solutions containing 10 mg ml^{-1} of polymer and 20 mg ml^{-1} PCBM, in ortho-dichlorobenzene (*o*-DCB) to 100°C for 12 hours to ensure full dissolution of the polymer. The substrates used were z-cut quartz discs, cleaned by 10 minutes of Ar plasma etch, followed by 3 rounds of ultrasonication for 3 minutes each in isopropanol, acetone and distilled water. A small volume of the polymer(:PCBM) solution (30 µL) was drop-cast directly onto the cleaned substrates, preheated to 100°C on a hotplate, and left to dry and anneal for 5 minutes.

For exciton diffusion length measurements, steady state UV-vis absorption, and TIPL, spin-coated neat polymer films were prepared by heating a 20 mg ml^{-1} solution of polymer in *o*-DCB to 100°C overnight. To prepare polymer films of different thickness, a 50 µL aliquot of the solution was removed 20 minutes before the film was spun, and added to a second vial containing pure *o*-DCB which was also preheated to 100°C to make solutions of 1, 2, 5 and 10 mg ml^{-1} concentration. A small volume of each of these (25 µL) was dropped and spun on substrates for 5 s at 800 rpm, then 45 s at 2000 rpm after which samples were annealed for 2 minutes at 100°C. For steady state UV-vis absorption and TIPL, quartz substrates were used which were cleaned in the same manner as those used for the drop-cast films.

For exciton diffusion length measurements, substrates with a compact TiO_2 quencher layer were prepared by RF sputtering a layer of TiO_2 to 80 nm thickness, followed by an annealing step at 451°C for 2 minutes under Argon. This gave thin films with a surface roughness of approximately 2 nm as determined by AFM (*sputtering and characterisation of TiO_2 films was performed by Ian McKerracher of the Australian National University*). Before polymer deposition these substrates were cleaned with compressed air only. The film thickness of each of the polymer films on quartz was determined by use of a Dektak Surface profiler.

Solutions for temperature-dependent TCSPC and TIPL measurements were prepared by heating 10 mg ml^{-1} of polymer in *o*-DCB to 100°C for 12 hours and diluting down to 0.05 and 5 mg ml^{-1} without filtering. The solutions were heated to 90°C for 30 minutes to ensure dissolution of the polymer before cooling to 10°C to begin measurement.

Photovoltaic device data was supplied by P. Tiwana of Merck Chemicals. Devices with the standard glass/ITO/PEDOT:PSS/polymer:PCBM/Ca/Al structure were prepared as follows: 1(1+1) ITO coated glass substrates were cleaned by ultrasonication in acetone, isopropanol and distilled water, and layer (20 nm) of poly(3,4-ethylenedioxythiophene)-poly(styrenesulfonate) (PEDOT/PSS, Clevios VP AI 4083, H.C. Starck) was deposited by spin coating and then dried for 30 minutes at 130°C in a nitrogen filled glovebox.

A 40 mg ml^{-1} solution of either $PC_{60}BM$ (phenyl-C61-butyric-acid-methyl-ester) or $PC_{70}BM$ (phenyl-C71-butyric-acid-methyl-ester) in *o*-DCB and additional *o*-DCB (both by volume) were added to the polymer material to make a final solution of

polymer:$PC_{60}BM$ (1:2) with total solid concentration of $30\,mg\,ml^{-1}$ in *o*-DCB. This solution was heated to dissolve the solids and then held at 70°C.

The active layer was deposited on top of the PEDOT:PSS coated substrates by doctor blading on an Erichsen Coatmaster 509MC, using the following parameters: coating temperature, 70°C; blade speed, $40\,mm\,s^{-1}$; screw gap, 0.03 mm; coating volume, 40 µL. The coated films were left to anneal for 2 min on a 70°C hotplate. Top Ca/Al cathodes were deposited by thermal evaporation. Current-density-voltage characteristics were taken with a Keithley 2420 Digital SourceMeter under standard 1 sun (AM1.5G) conditions, which were checked with a K5 filtered calibrated silicon reference diode.

5.4 Diffusion Length Measurements - Method and Model

In order to measure the diffusion length of excitons in polymer films, the time resolved photoluminescence from thin films of polymer with and without a thin layer of an electron acceptor material are compared. For each of the polymer materials studied in this chapter, two films of two different thicknesses are deposited on one plain quartz substrate, and on a substrate coated with a sputtered layer of TiO_2 (i.e. 4 samples per polymer studied).

When the samples are excited with a short laser pulse, excitons are generated in the film, with density proportional to the light intensity. In the absence of any reflections of the pump beam, this is given by Beer's law,

$$I(x) = I_0.10^{-\alpha x} \tag{5.1}$$

where I_0 is the intensity of the excitation pulse, α is the thin film absorption coefficient and x is the distance from the point of entry into the film, in this case measured from the glass/polymer interface to the polymer/quencher interface.

The generated excitons begin to diffuse through the film which, as a result of the relatively short diffusion lengths commonly observed in polymer films, must be prepared to be less than 30 nm in thickness in order to observe any PL quenching. Since the initially generated exciton density is greatest at the glass/polymer interface, this results in a net migration of excitons toward the quencher. Some excitons reach the polymer-quencher interface where electron transfer (ET) occurs. When an electron is removed by the TiO_2 acceptor, it can no longer recombine radiatively with the

hole left behind in the polymer film. As the PL intensity is linearly proportional to the number of excitons at low exciton densities, the ET manifests as a faster decay of the total photoluminescence when an acceptor layer is present, that is, the photoluminescence is partially quenched. This is described graphically in Figure 5.1.

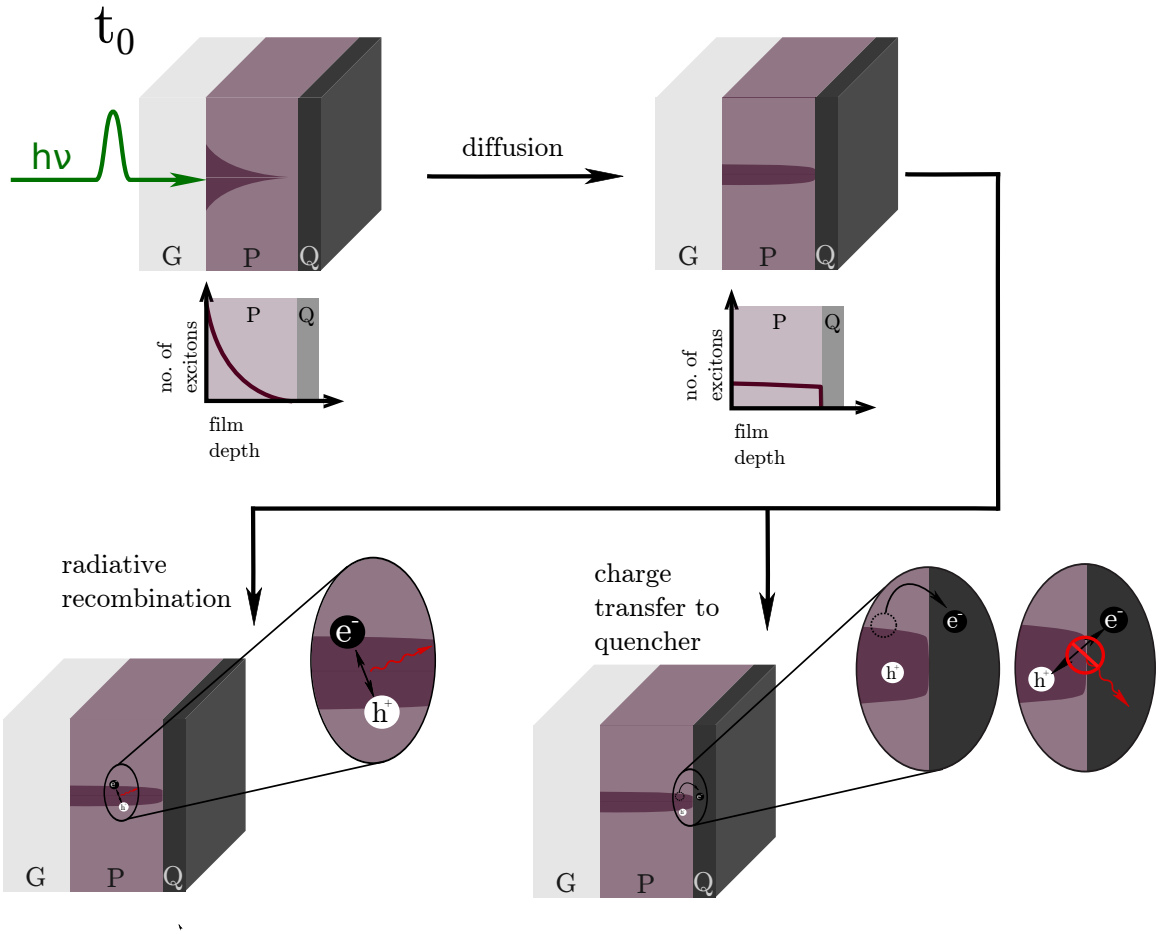

Figure 5.1: Schematic description of the diffusion length measurement experiment. Initially a short ($\sim$ 100 ps) laser pulse excites the sample from the substrate side, away from the quencher material. Excitons are generated through the film proportional to the light intensity at point x, which is determined by the absorption coefficient of the material at the excitation wavelength. As there is a gradient with respect to the excitation density in the film, diffusion from high to low density, toward the quencher material occurs. Recombination processes intrinsic to the polymer can occur during transit but when an exciton approaches the TiO2 quencher, charge transfer from polymer to quencher occurs and subsequent radiative recombination is no longer possible. By comparing the rate of PL quenching with and without this extra decay pathway, the diffusion coefficient and thus the diffusion length can be measured.

The distribution of excitons throughout the film can be described by a 1D diffusion

equation of the form

$$\frac{\partial n(x,t)}{\partial t} = D\frac{\partial^2 n}{\partial x^2} - k(t)n(x,t) \tag{5.2}$$

where $n(x,t)$ is the number of excitons as a function of time and position, D is the diffusion coefficient and $k(t)$ is the observed PL decay rate in the absence of any quencher material.[193] In the neat polymer films, the PL decay rate is well described by a simple monoexponential decay, and hence the reference PL is fit with a single exponential function

$$I(t) = I_0 \exp(-(t/\tau)), \tag{5.3}$$

where τ is the PL lifetime. The total PL decay rate in Equation 5.2, is then given by

$$k_s(t) = k_f + k_{nr} = \tau^{-1}$$

where k_f is the rate of decay from the excited state by fluorescence, and k_{nr} is the non-radiative decay rate.

5.4.1 Finite Difference Method

Approximate solutions to equation 5.2 are determined by a finite difference method. The complete solution to the equation is represented by points on a discretised grid with each point representing the exciton density $n(x,t)$ at various time and position points t and x (see Figure 5.2). The derivatives in the equation are approximated by finite differences between the grid points. As the initial distribution of excitons throughout the film, $n(x,t_0)$, and the boundary conditions are known, the density at any point on the grid can be calculated.

Labelling each gridpoint n_j^m, where m is the number of time steps Δt away from the initial time t_0, and j is the spatial index, the partial derivative with respect to time at any position x_j is approximated as

$$\left(\frac{\partial n}{\partial t}\right)_j \approx \frac{n_j^{m+1} - n_j^m}{\Delta t}. \tag{5.4}$$

In the Crank-Nicolson method[51] the second derivative with respect to the spatial component at a given time index m is given by

$$\left(\frac{\partial^2 n}{\partial x^2}\right)^m \approx \frac{1}{2}\left[\left(\frac{\partial^2 n}{\partial x^2}\right)^{m+1} + \left(\frac{\partial^2 n}{\partial x^2}\right)^m\right] \tag{5.5}$$

$$\approx \frac{1}{2}\left[\frac{n_{j+1}^{m+1} + n_{j-1}^{m+1} - 2n_j^{m+1}}{\Delta x^2} + \frac{n_{j+1}^m + n_{j-1}^m - 2n_j^m}{\Delta x^2}\right] \tag{5.6}$$

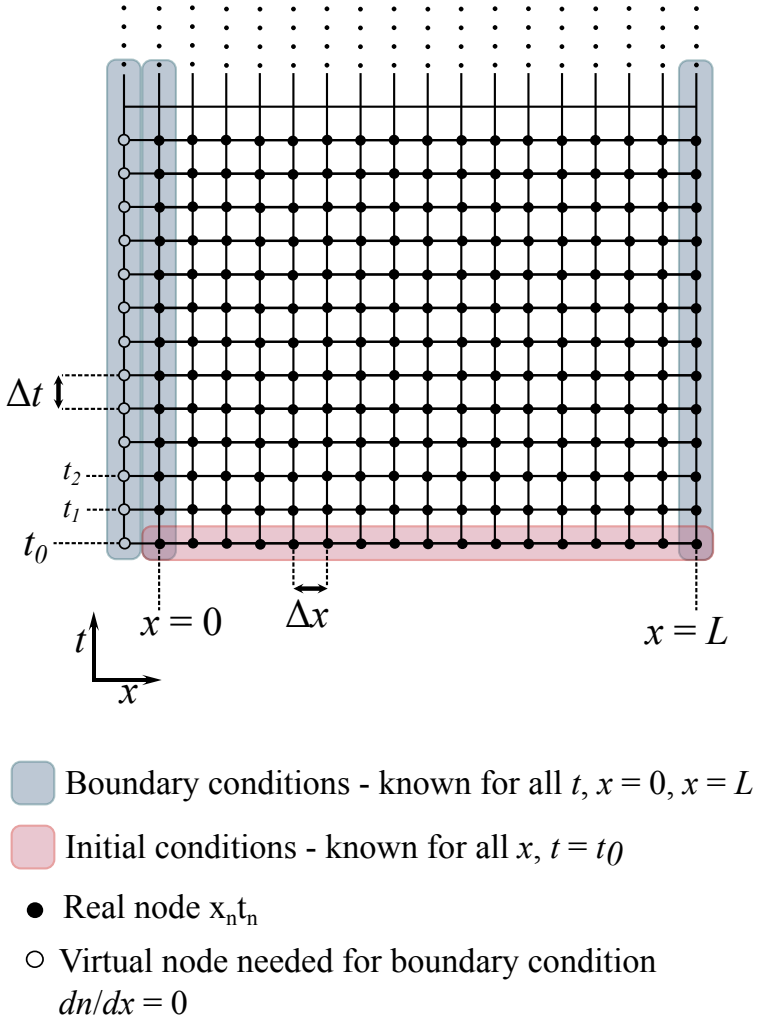

Figure 5.2: Representation of the discretised grid comprising the solutions of Equation 5.2. The entire solution is split up into a grid of size $m+1 \times j+2$, where $m+1$ is the number of temporal points and $j+1$ is the number of real spatial points. The values at the bottom of the grid shaded in pink are defined by the initial condition, and the edge values are defined by the boundary conditions (see 5.4.2). As the boundary condition at the substrate/polymer interface $x = 0$ is defined by the derivative $dx/dn = 0$, an extra virtual point must be included in the grid. As the values on three sides of each row are known, subsequent rows can be calculated iteratively. This is repeated until there are enough data points to compare with experimental data.

and the value of n_j^m is approximated by

$$n_j^m \approx \frac{1}{2}\left[n_j^{m+1} + n_j^m\right] \tag{5.7}$$

Substituting these back into (5.2), gives

$$\frac{n_j^{m+1} - n_j^m}{\Delta t} = \frac{D}{2}\left[\frac{n_{j+1}^{m+1} + n_{j-1}^{m+1} - 2n_j^{m+1}}{\Delta x^2} + \frac{n_{j+1}^m + n_{j-1}^m - 2n_j^m}{\Delta x^2}\right] - \frac{k_s}{2}\left[n_j^{m+1} + n_j^m\right] \tag{5.8}$$

If a new parameter μ is defined, such that

$$\mu = \frac{D\Delta t}{\Delta x^2}, \tag{5.9}$$

collecting all the terms for the row $m+1$,

$$-\mu n_{j+1}^{m+1} + (2 + 2\mu + k_s\Delta t)n_j^{m+1} - \mu n_{j-1}^{m+1} = \mu n_j^m - 1 + (2 - 2\mu - k_s\Delta t)n_j^m + \mu n_{j-1}^m \tag{5.10}$$

gives a set of linear equations of the form

$$\mathbf{J} \cdot \mathbf{N} = \mathbf{R}, \tag{5.11}$$

where $\mathbf{N}$ is a vector describing the exciton density at each spatial point for the time $m+1$. Multiplying both sides by the inverse of matrix $\mathbf{J}$ gives the solution

$$\mathbf{N} = \mathbf{J}^{-1}\mathbf{R}. \tag{5.12}$$

This is repeated until the grid covers the time-period of interest after excitation.

5.4.2 Boundary Conditions

The precise forms of the matrices $\mathbf{J}$ and $\mathbf{R}$ depend on the boundary conditions imposed on the model. In the polymer film, the exciton density at the polymer:TiO_2 interface is zero at all times as electron transfer to/from the quencher is assumed to occur with unit efficiency for all excitons reaching this interface, thus removing them from the system. This is a Dirichlet boundary condition of $n(t, d) = 0$. It may be however, that the quenching process does not occur with unit efficiency in reality, in which case the values determined by the model will be an underestimate of the true diffusion length. At the other side of the film, there is no such quenching at the glass and polymer interface (any non-radiative recombination by defects at this surface are included in $k_s = k_f + k_{nr}$ which is determined by measuring the PL from the reference sample), and there can be no exciton flow out of the polymer into the glass. This is represented by a Neumann condition $dn/dx = 0$ for all times $t \geq t_0$.

Solving the set of linear equations for all time-steps gives the discretised grid $n(x, t)$ represented in Figure 5.2, which is then summed along each column to give

the total exciton density in the film at each time step $n(t)$. This is convoluted with the measured instrument response as described in Section 3.5 and compared with the measured data from the quenched sample. The value of D is optimised with a non-linear least squares regression analysis by varying D, recalculating the function $n(t)$ and convoluting it with the IRF for each iteration until a good fit is achieved.

5.5 Results and Discussion

Figure 5.3 introduces the materials used in this study, which form a series of related low-bandgap polymers with active donor-acceptor units comprising 2,6-[benzodithiophene] acceptors and 2,5-thiophene-*co*-4,7-[5,6-dialkoxybenzothiadiazole]-*co*-2,5-thiophene (BDT) donors. The general structure of the donor and acceptor units is shown in Figure 5.3a and Figure 5.3b gives a representative current-density-voltage curve under solar simulator conditions for the best performing material (P5), for which a PCE value of 5.42% was observed. Details of the different alkyl side chains attached to the BDT unit, along with the number-average molecular weight, energy levels and band gap energy of each of the polymers, along with average measured PV parameters for polymer:$PC_{60}BM$ solar cell fabricated as described in the Experimental Section (5.2) are summarized in Table 5.1.

Small changes in alkyl chain length have a large effect (up to a factor of 2) on power conversion efficiency but the values do not vary systematically. Polymers P1–3 overall tend to exhibit lower photovoltaic efficiencies than polymers P4 and P5, with the trend dominated by the higher J_{SC} of devices containing these materials. As shown below, such differences correlate with changes in the extent to which crystallite domains form in the films, as discussed below.

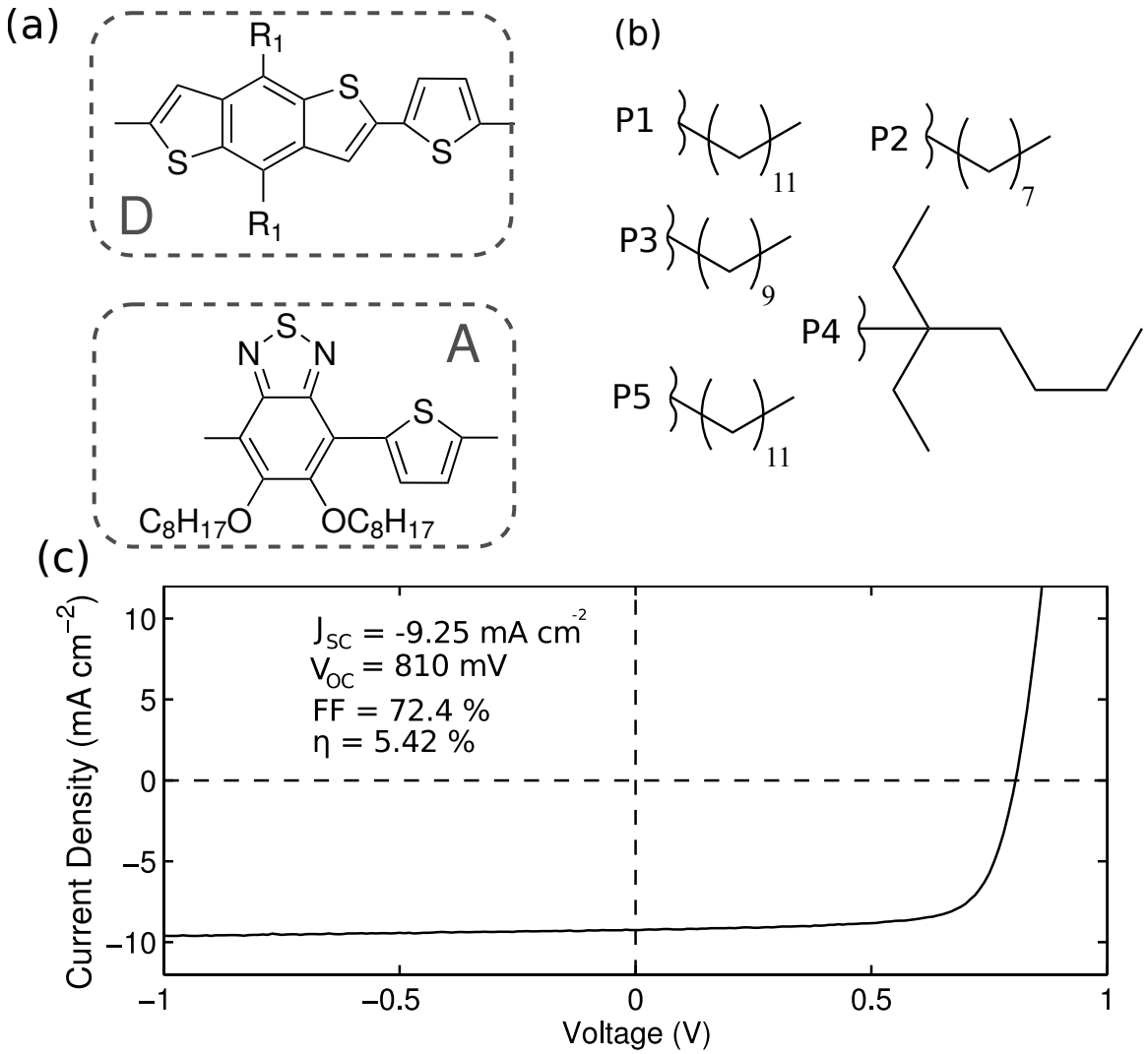

Figure 5.3: (a) Donor and acceptor moieties of which the materials used in this study are comprised. All polymers have the same benzothiadiazole acceptor group and different alkyl side chains (R_1) on the benzodithiophene donor unit as described in Table 5.1. (b) Drawing of the different alkyl side chains (R_1) attached to the central backbone of polymers P1–5. (c) Representative current density–voltage curve obtained from a device incorporating P5 blended with $PC_{60}BM$ as described in the Experimental Methods section (5.2). Each reported value is the mean value obtained from 10 individual photovoltaic cells on a single substrate. *Polymers supplied by Merck Chemicals. Device fabrication and characterisation data by P. Tiwana of Merck Chemicals.*

Polymer	Type	R_1 group	M_n (kDa)	HOMO (eV)	LUMO (eV)	E_g (eV)	V_{OC} (mV)	J_{SC} ($mA\,cm^{-2}$)	FF	PCE (%)
P1	LE	$C_{12}H_{25}$	21.6	-5.15	-3.33	1.82	667	5.33	55.7	1.98
P2	LE	C_8H_{17}	22.6	-5.3	-3.53	1.77	680	9.58	65.8	4.28
P3	LE	$C_{10}H_{21}$	15.3	–	–	–	697	5.34	33.1	1.23
P4	HE	$CH_2CH(C_2H_5)C_4H_9$	29.7	-5.33	-3.56	1.77	867	12.04	43.9	4.58
							(840)	(12.3)	(52.7)	(5.44)
P5	HE	$C_{12}H_{25}$	28.4	-5.34	-3.58	1.76	810	9.25	72.4	5.42
							(785)	(10.97)	(69.7)	(6.00)

Table 5.1: The polymer type refers to the two different approaches used in the chemical synthesis; the first approach yielding a system with LOW chain entropy (P1 to P3) while the second resulted in systems with HIGH chain entropy (P4 and P5). The number average molecular mass (M_n) along with the highest occupied molecular orbital (HOMO), lowest unoccupied molecular orbital (LUMO), and band gap (E_g) energies as determined from cyclic voltammetry measurements on thin film are also given. The photovoltaic properties are the open circuit voltage, V_{OC}; short circuit current, J_{SC}; fill factor, FF; and power conversion efficiency, PCE. Devices were prepared as described in the Sample Preparation section, with $PC_{60}BM$ as the electron acceptor. Values in parentheses were recorded when $PC_{70}BM$ was used instead. Devices were tested with 10—11 cells on a single substrate (cell area 4.5 mm^2 each), showing a typical standard deviation of $\pm 0.25\%$ to $\pm 0.5\%$ about the mean PCE values reported in the table.

5.5.1 Steady-State Absorption and Photoluminescence

Figure 5.4 shows steady-state absorption and emission spectra of the five polymers in dilute solution (a) and thin film (b). The absorption onset shows a red shift, broadening and increase in vibronic structure on thin film formation, indicating increased interchain interactions,[17] with this effect being most pronounced in P1 and least in P4 and P5. Time integrated PL of the solutions shows a strong red-shift in the emission spectrum of P1 compared to that of the other polymers, indicating that for this polymer, aggregation and interchain interactions are present even in dilute solutions. As with the absorption, a red-shift and increase in vibrational structure is observed in the PL following thin film formation, with the exception of polymer P1, in which the peak emission is unchanged between solution and thin film. This observation confirms that polymer P1 forms extended aggregate domains comparable to those in thin film, even when in dilute solutions at room temperature.

5.5.2 Film Morphology – Wide Angle X-ray Scattering and AFM

In order to investigate the nature of aggregate domains in the polymer solid, wide angle X-ray scattering measurements were performed on drop-cast polymer films. The deposition method used to prepare polymer thin films can affect the resulting morphology, with large differences observed between films prepared by spin-casting, in which solvent evaporates rapidly from the solution during spinning, and those prepared by doctor-blading, in which solvent evaporation occurs on a longer time scale.[154] In order to allow films to form with slower solvent evaporation, yet avoid difficulties associated with doctor-blading on small substrates, drop-casting was used to prepare the samples for WAXS and direct PL quenching measurements in polymer:fullerene blends. In Figure 5.5, the measured WAXS patterns show large differences between polymers P1–3 and P4–5, with the former exhibiting a far higher degree of crystallinity while the latter two are almost entirely amorphous. Polymer P1 is found to display the highest degree of crystallinity, in agreement with the above analysis of its UV-vis absorption and PL spectra. The three more crystalline materials exhibit a peak with a d-spacing of 2.11 nm in P1 and 1.78 nm in P2 and P3, which has been assigned to the (100) inter-lamellar spacing in similar materials.[117] The absence of a discernible peak corresponding to a (010) plane π-stacking distance implies the more crystalline polymers forming π-stacked crystallites parallel to the

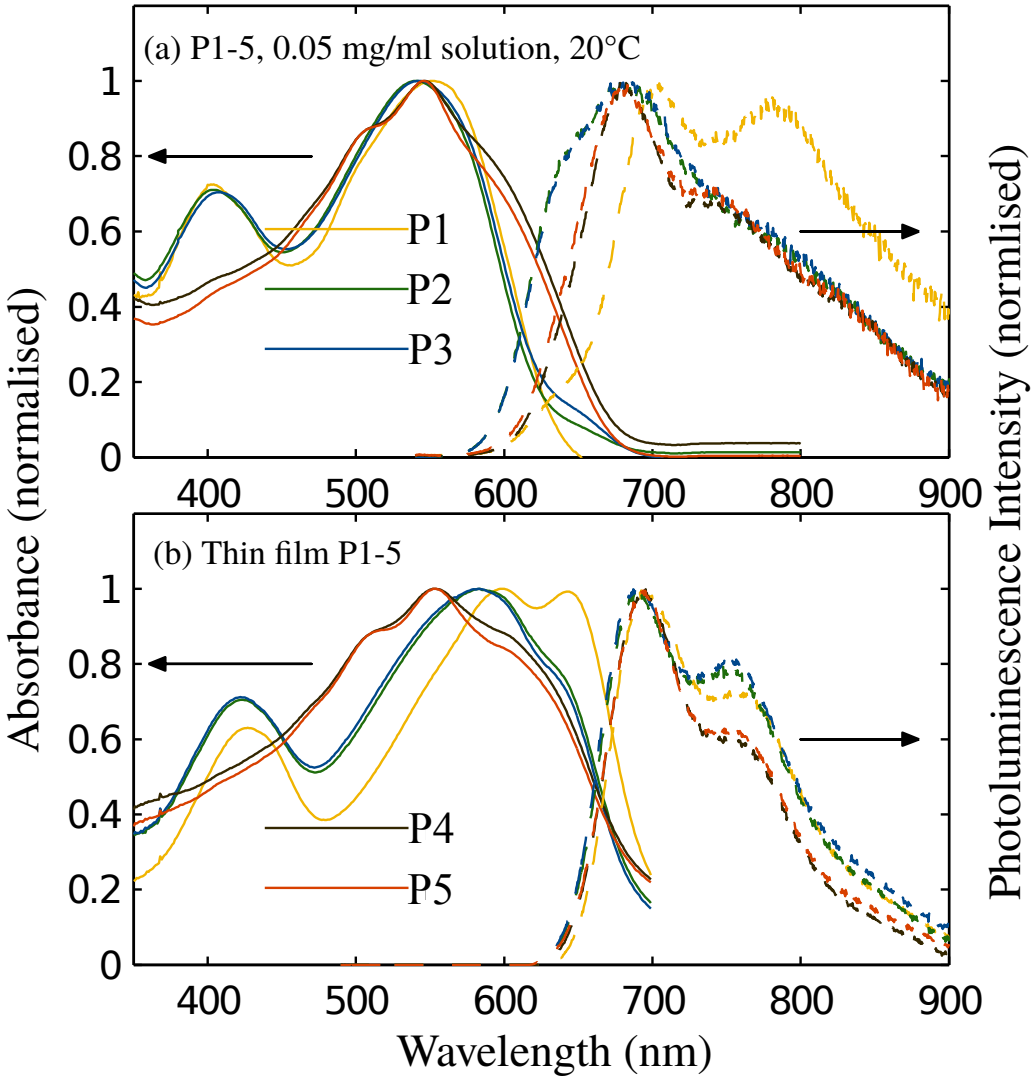

Figure 5.4: Steady-state absorbance and time-integrated photoluminescence spectra for all five polymers (a) in dilute (0.05 mg mL^{-1}) solution and (b) for thin (spin-cast) films at room temperature. For the PL spectra, samples were excited at 450 nm.

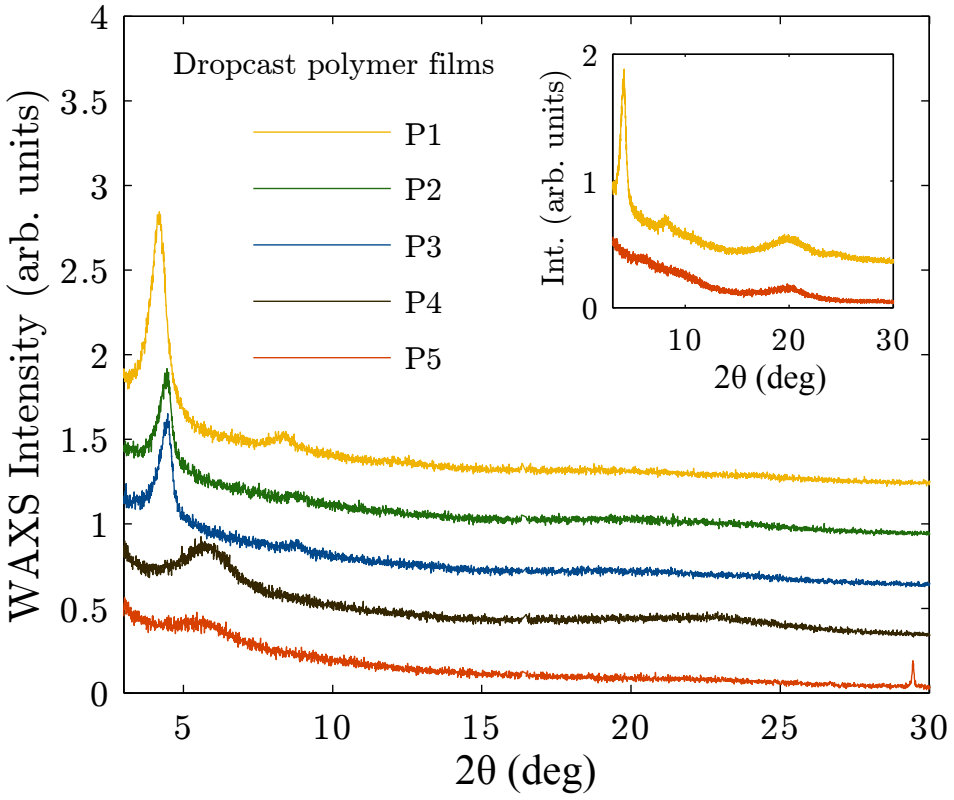

Figure 5.5: Wide-angle X-ray diffraction patterns for drop-cast neat polymer films with curves offset from one another for clarity. The polymers P1, P2, and P3 show a far higher degree of crystallinity than the relatively amorphous P4 and P5, with P1 being the most crystalline of all the materials studied. The strong peak at $2\theta = 4°$corresponding to a repeat unit distance of approximately 2 nm is assigned to the distance between parallel polymer chains in the (100) plane, with the small peak at $2\theta = 8°$assigned to the second-order diffraction from the same plane. The inset shows WAXS patterns of P1:PCBM and P5:PCBM blend films prepared as described in section 5.3.

substrate surface.[68] The higher intensity of the (100) peak in P1 indicates a higher density of these crystalline domains in films of this material, with a lower degree of crystallization shown by P2 and P3, and mostly amorphous morphology for P4 and P5. The inset to Figure 5.5 displays the effect of adding PCBM to the polymer with one example shown for each of the two types of polymer, the most crystalline P1 and the mostly amorphous P5. The WAXS patterns of polymer:PCBM films show little difference to those of the corresponding neat polymer films, i.e. blending with PCBM seems to have little effect on the degree or size of polymer crystallites formed. The additional broad peak at $2\theta = 20°$(d = 3 Å) is attributed to the formation of PCBM crystallites in the film.[154]

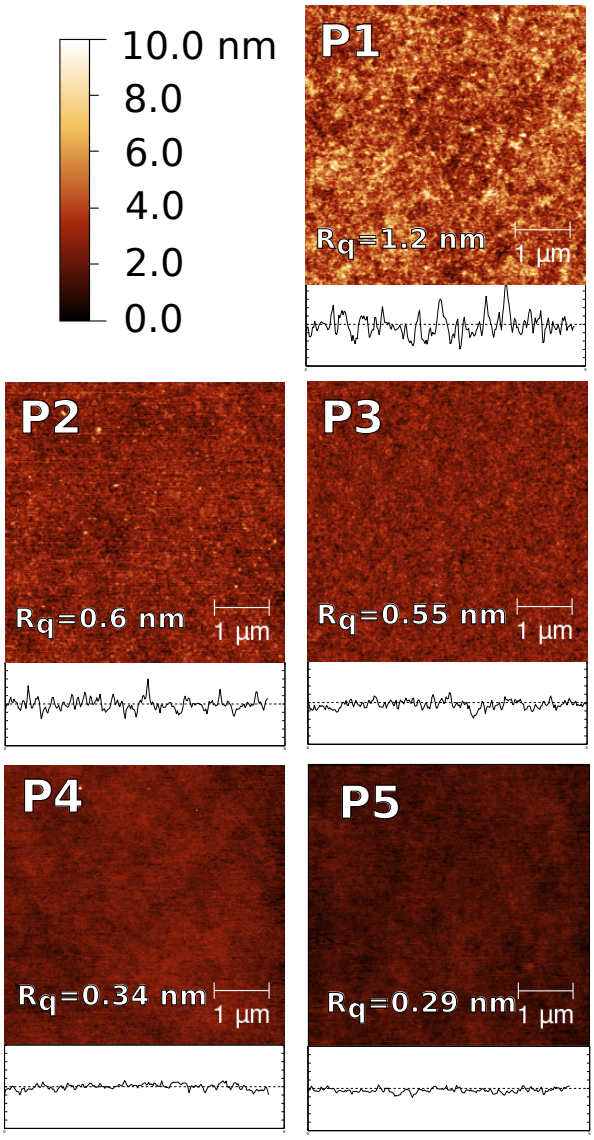

Figure 5.6: Topography images obtained by atomic force microscopy for neat films of all polymers. The black solid lines below each image show a typical height variation across the film from which the surface roughness R_q was determined for each film as shown on the respective AFM images.

The trends observed in WAXS patterns have a clear correspondence with surface topology of thin spin-cast films of the neat polymers. Figure 5.6 shows atomic force microscopy images obtained for thin films of the five polymers, with a typical height variation contour shown below each image. The mean square surface roughness of the most crystalline polymer P1 was determined to be 1.2 nm, which is followed by a value of ∼0.6 nm for the less crystalline P2 and P3, and a roughness of 0.3 nm for the mostly amorphous polymers P4 and P5. Enhanced surface roughness has in the past been associated with the presence of chain aggregates in the polymer film, as such domains may extend and protrude beyond the surface.[26] The clear correlation between crystallinity observed in WAXS patterns and surface roughness seen in AFM suggests that the formation of nanosized crystallites is also a prominent factor for these materials. The polymer with the highest prevalence for crystallite domain formation (P1) was found to show the poorest performance in photovoltaic devices, while the polymer that is most amorphous and displays least surface roughness (P5) has the highest photovoltaic power conversion efficiency in the series.

5.5.3 Diffusion Length Measurement

In order to unravel the reasons for the correlation between photovoltaic device performance and polymer film morphology, the processes of exciton diffusion and interfacial dissociation in this material system were investigated. The presence of crystalline domains may affect the diffusion of excitons through the polymer, which may either be enhanced through the high order within a domain, or impeded by the energetic barriers presented by additional interfaces at domain boundaries. The transfer of photo-generated excitation to the polymer-fullerene interface is a vital step in BHJ devices, and radiative recombination of excitons before they reach an interface and dissociate can potentially be a large source of loss. In order to minimize this, the average distance over which excitons migrate before recombining should be equal or greater to the polymer domain size.[155]

Various methods have been developed to determine the mean exciton diffusion length.[140;155;90] Here, the time-resolved PL quenching method described in Section 5.4 was used to investigate the influence of film crystallinity on the value of this parameter.[150] The PL quencher layer used in this case was an 80 nm thick layer of TiO_2 deposited on quartz by RF sputtering. This thickness was chosen in order to minimise reflection of the 450 nm pump pulse used in the experiment, allowing the

initial distribution of excitons in the film to be described by a simple exponential depth profile.

Observation of the charge transfer step and free charge yields across organic semiconductor-TiO_x interfaces have been reported and range from relatively efficient (95% CT, 45% exciton to free charge conversion rate with terthiophene[95]) to highly inefficient (< 1% free charge yield with P3PBT[192]). The values observed therefore are a minimum possible diffusion length, as in systems with less than perfect charge-transfer at the interface a longer diffusion length would be required to produce the same rate of PL quenching. Figure 5.7 shows PL decay transients measured for thin films of the most and least crystalline polymers P1 and P5 deposited on quartz substrates with and without the TiO_2 quencher for film thicknesses of approximately and 13 and 25 nm (P1), and 5 and 15 nm (P5). The solid light-blue or light green lines in Figure 5.7 are the solutions of the diffusion equation (Equation 5.2), integrated over the film thickness and convoluted with the instrument response function (IRF) as described in Section 5.4. Here, solely the diffusion constant was varied in order to obtain best fits to the observed PL transients in the presence of the TiO_2 quencher. The procedure was carried out for both film thicknesses, which yielded good agreement, and values extracted for the diffusion coefficient and diffusion length, L_D, are given in Table 5.2 together with the PL decay lifetime. The more crystalline P1 exhibits an exciton diffusion coefficient that is approximately three times higher than that of the more amorphous P5. When taking into account the differing exciton lifetimes, the exciton diffusion length in P1 is found to be about 85% higher than that in thin films of P5. These discrepancies may in part be accounted for by the enhanced overlap between P1 absorption and emission spectra (see Figure 5.4) which arise from the strong aggregation feature near the band edge of P1. According to Förster Theory,[75] such spectral overlap will enhance exciton transfer between chromophores of the polymer leading to faster exciton diffusion.

Differences in exciton diffusion lengths may have a strong impact on photovoltaic device efficiencies because they can, depending on the degree of phase segregation, affect the fraction of excitons reaching an interface in BHJ films. In order to ascertain whether this step in device operation is the limiting step, the rates at which excitons are quenched was examined directly[87] in spin-coated BHJ films containing blends of polymer and PCBM in a 1:2 weight ratio. As a reference measurement, Figure 5.8a shows the measured PL transients for all five polymers in neat films (no PCBM).

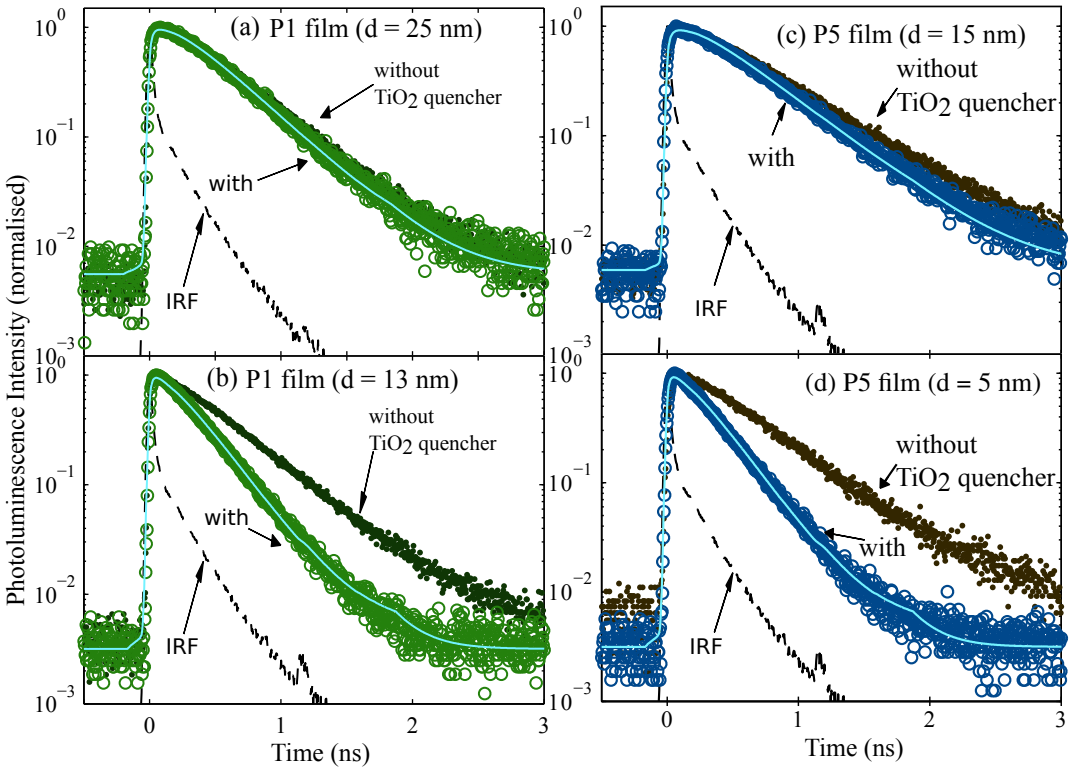

Figure 5.7: Photoluminescence decay transients measured for polymers P1 (left, green curves) and P5 (right, blue curves). In each case the light open circles and dark solid dots are the PL traces with and without the 80 nm thick layer of sputtered TiO_2. Data were taken with the TCSPC technique using a small-area silicon avalanche photodiode; the dashed line is the instrument response function (IRF) with 35 ps FWHM. The solid light-green (light-blue) line is the one-dimensional exciton diffusion model fit to the data by iterative reconvolution with the IRF, as described in the Section 5.4. The sole fitting parameter was D, the diffusion coefficient. For each polymer, curves are shown for two different polymer film thicknesses: P1 – (a) 25 nm and (b) 13 nm, P5 – (c) 15 nm and (d) 5 nm. In each case, samples were excited from the front with pulses of 100 fs duration and 450 nm wavelength. The PL detection wavelength was 690 nm. The parameters extracted from fits to the curves are summarized in Table 5.2.

polymer	τ (ps)	D (10^{-3} cm^{2}s^{-1})	L_D (nm)
P1	350 ± 10	1.0 ± 0.3	7.4 ± 2.5
P5	250 ± 10	0.31 ± 0.3	4.0 ± 1.0

Table 5.2: Lifetimes determined from monoexponential fits to the PL transients in the absence of the quencher layer; exciton diffusion constant D extracted from modelling PL transients in the presence of a TiO_2 compact quencher layer; exciton diffusion length $L_D = \sqrt{\tau D}$. The main source of the ~30% error in the values for D is caused by inherent difficulties in determining the polymer film thickness.

Interestingly, a clear difference between the mainly amorphous (P4, P5) and more crystalline (P1–3) polymers can be seen, with the former displaying lifetimes of around 450 ps and the later 350 ps. These differences do not depend on the wavelength at which the films are excited: the inset to Figure 5.8a shows the PL lifetime, τ, obtained from convoluted monoexponential fits to the PL transients obtained for thin films of polymers P1 (crystalline) and P4 (amorphous) following excitation at wavelengths between 370 nm and 650 nm. The difference between the lifetimes measured for the two polymers is maintained across this range and the lifetime appears to be largely independent of pump energy. For strongly aggregated polymer chains, a lengthening of the PL emission lifetimes would normally be expected, as the electronic coupling between molecules in H-aggregate conformation is known to reduce the oscillator strength of the coupled system.[167] However, in thin polymer films, excitons will rapidly diffuse to the most strongly aggregated regions because these have the lowest associated potential energy. As excitons reach such sites, their emissivity is gradually reduced, which appears as a rapid PL quenching that is mostly representative of the exciton diffusion rate to weakly emissive sites.

5.5.4 PL Quenching in BHJ Film

To assess the exciton quenching rate in polymer:PCBM BHJ films, PL transients were measured with high (350 fs) time resolution, as shown in Figure 5.8b. For all five polymers, the initial PL decay is rapid, with lifetimes of the order of 1 ps. To examine the possible presence of residual slower decay components, lower-resolution (230 ps) longer-time PL decay curves were acquired using TCSPC, as shown in the inset of Figure 5.8b. There is a small amount of residual PL in blend films containing polymers P1 and P4 at longer times, however, the PL transients from the other films, P2, P3 and P5, follows the instrument response, indicating that all PL is quenched within ∼200 ps after excitation. There is no clear correlation between the presence of such residuals and performance of the polymer in photovoltaics devices (see Table 5.1). This is not surprising given that for all polymers, the majority ($> 90\%$) of excitons generated in BHJ films with PCBM reach an interface and are quenched within 5 ps after excitation. Such rapid quenching also means that the differences in exciton diffusion lengths observed for neat polymer films (Table 5.2) cannot have any significant influence on the efficiency of charge generation in the polymer blend with PCBM. These measurements therefore suggest that these DA-copolymer:PCBM

blends must exhibit a large volume fraction (> 90%) for which the length scale of phase segregation falls significantly below the measured diffusion lengths (4–7.5 nm). The tendency of the polymer to form crystalline domains hence appears to have little effect on the initial exciton dissociation, and must rather influence the remaining subsequent charge recombination and extraction steps.

5.5.5 Aggregate Formation – Temperature Dependent PL

Finally, the extent to which aggregate domains in thin polymer films may be precipitated by agglomerations already present in solution prior to casting was investigated. There have been previous reports of polymer chain aggregates forming in solution which then persist into the cast film.[234] For such systems, the final film morphology may be particularly sensitive to solution temperature and casting conditions. In order to investigate such effects, the evolution of the emission spectra and transients of the five polymers in solution were measured with temperature varied between 10°C and 90°C. The data for all five polymers are give in Figures 5.9 and 5.11.

Figure 5.9 shows the time-resolved PL decay for P1 and P5, recorded for emission wavelengths ranging from 600 nm to 850 nm, at low (10°C) and high (90°C, inset) solution temperature. The low-temperature (10°C) dynamics are markedly different for the two polymers: P1 displays a mono-exponential PL decay at short wavelength, but exhibits a second, short-lived (τ_1 = 408 ps) contribution at longer wavelengths. The relative contributions of the two terms are extracted through global fitting of two mono-exponentials to the data set and are plotted in Figure 5.10 as a function of emission wavelength. It appears that for P1 in *o*-DCB solution, two types of emitting species are present. Once the solution has been heated to 90°C (inset to Fig.5.9a) however, only mono-exponential decay dynamics are observed at all detection wavelengths. The short-lived component therefore can be assigned to the emission from chain aggregate clusters in solution, noting that their emission lifetime (408 ps) is only slightly longer than that for the thin film of the same polymer (340 ps) – see Table 5.3. These observations imply that some of the crystalline domains found in P1 films begin to form early during the casting process and are caused by an increased propensity of P1 to aggregate in solution. All of the other polymers instead exhibit very different behaviour, as shown in Figure 5.9. Mono-exponential PL decays are observed at all solution temperatures with lifetimes τ_2 ranging between 1.45 – 1.75 ns (see Table 5.3). The observed additional slow PL rise at longer emission wavelengths

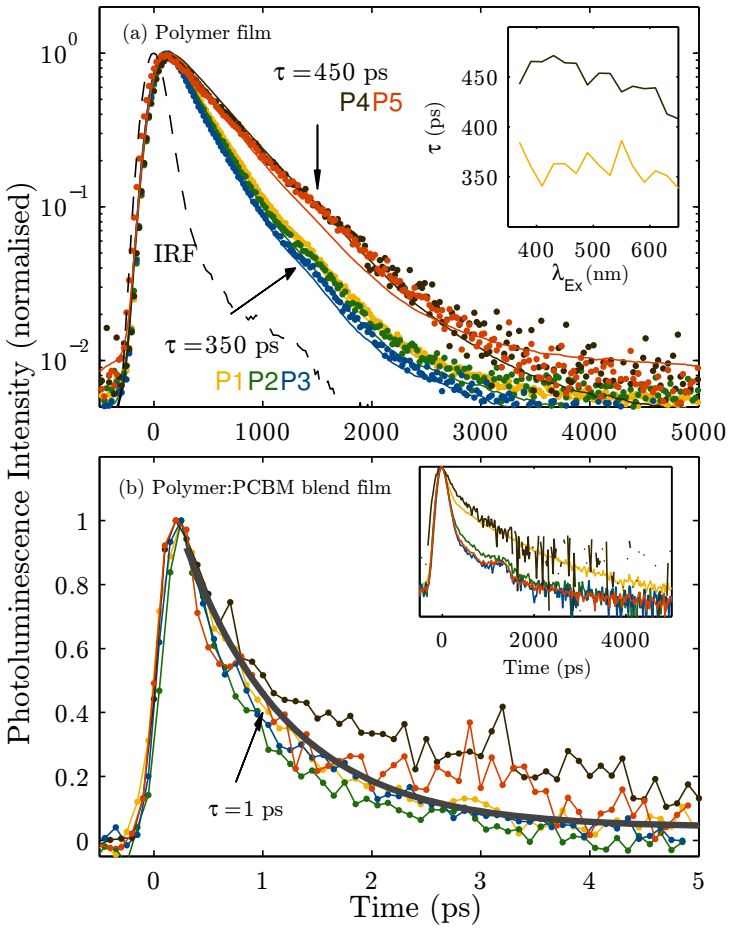

Figure 5.8: (a) Time-resolved photoluminescence transients on spin-cast films of neat polymer measured by TCPSC with excitation wavelength of 450 nm and detection wavelength set to 690 nm. The dashed line is the instrument response function (IRF) of the photomultiplier tube used for detection, showing 230 ps FWHM. The thin films of more crystalline (P1–P3) exhibit characteristic PL decay times of approximately 350 ps, whereas the amorphous polymers (P4, P5) show longer lifetimes of approximately 450 ps. The inset shows the PL lifetime extracted from response-convoluted monoexponential fits to the PL transients for P4 and P1 polymer films, as a function of the excitation wavelength. (b) Time-resolved PL transients of thin BHJ films of polymer:PCBM blends in a 1:2 ratio measured by PLUC with 350 fs time resolution (main figure) and TCSPC with 230 ps resolution (inset). The bold grey curve is a monoexponential decay with 1 ps lifetime included as a guide to the eye. As can be seen from the inset figure, there is some residual, longer-lived PL in the blend films with P1 and P4 at longer times, whereas decay curves for P2, P3, and P5 all follow the instrument response.

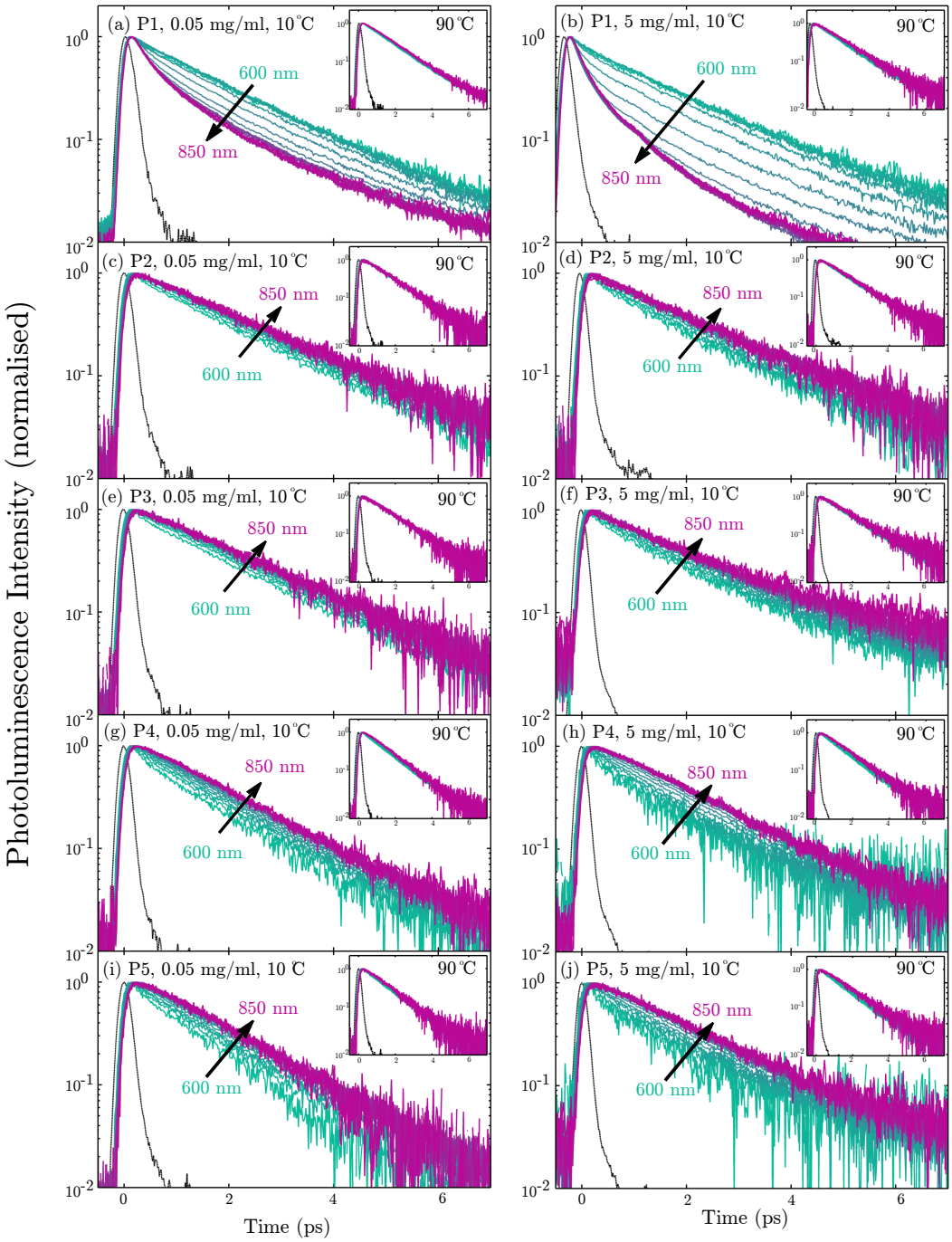

Figure 5.9: Photoluminescence decay transients for the polymers (a, b) P1, (c, d) P2, (e, f) P3, (g, h) P4 and (i, j) P5 solutions in *o*-DCB at 10°C (main figure) and 90°C (inset). Decay transients on the left (a, c, e, g, i) were measured from dilute solutions ($0.05\,\mathrm{mg\,mL^{-1}}$) of each polymer, while transients on the right (b, d, f, h, j) were measured from concentrated ($5\,\mathrm{mg\,mL^{-1}}$) solutions. In each case, the excitation wavelength was held constant at 450 nm, and the time-resolved PL intensity measured at emission wavelengths ranging from 600 nm (green) to 850 nm (purple) in 10 nm steps.

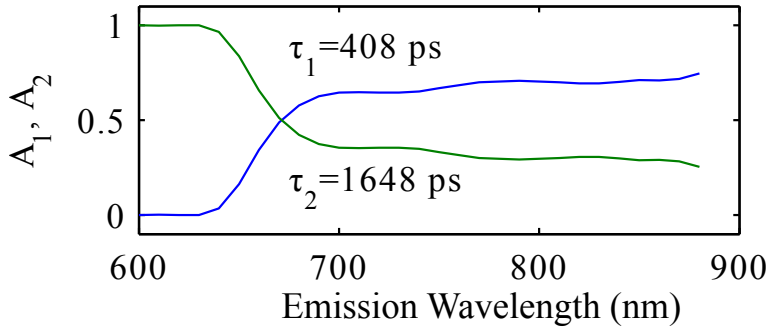

Figure 5.10: The relative contributions of the short (A_1, τ_1 = 408 ps) and long (A_2, τ_2 = 1648 ps) lifetimes as a function of the emission wavelength from polymer P1 extracted by global fitting of decay traces taken at multiple wavelengths with a bi-exponential. The solution concentration was 0.05 mg/ml in *o*-DCB, held at 10°C and the samples were excited at 450 nm.

is attributed to exciton relaxation to lower energy sites, possibly within chain clusters that do not exhibit the strong interchain electronic coupling exhibited by polymer P1. At high temperatures (inset), all polymers are completely dissolved and there is no migration to aggregate or lower-energy sites in the ensemble.

	Solution		Thin Film
polymer	τ_1 (ps)	τ_2 (ps)	τ_{film} (ps)
P1	408	1648	340
P2	—	1757	321
P3	—	1765	299
P4	—	1474	502
P5	—	1456	443

Table 5.3: PL Lifetimes extracted from monoexponential fitting to PL transients recorded for polymers P1–P5 in solution (0.05 mg ml^{-1}) at 10°C and for drop-cast polymer films. For solutions, polymer P1 is the only polymer to show contributions from two subspecies, exhibiting an additional short decay component τ_1 that is similar to τ_{film}.

The time integrated PL spectra for dilute (main figure) and concentrated (inset) polymer solutions at temperatures ranging from 10°C to 90°C (Figure 5.11) were measured in order to examine the effects upon polymer dissolution with increasing solvent temperature. There is an overall broadening and loss in vibronic structure along with a blue shift of the peak emission observed with increasing temperature. Such features may be related to a variety of effects, such as temperature-dependent changes in the dielectric constant, population of vibrational modes and solvation effects. In

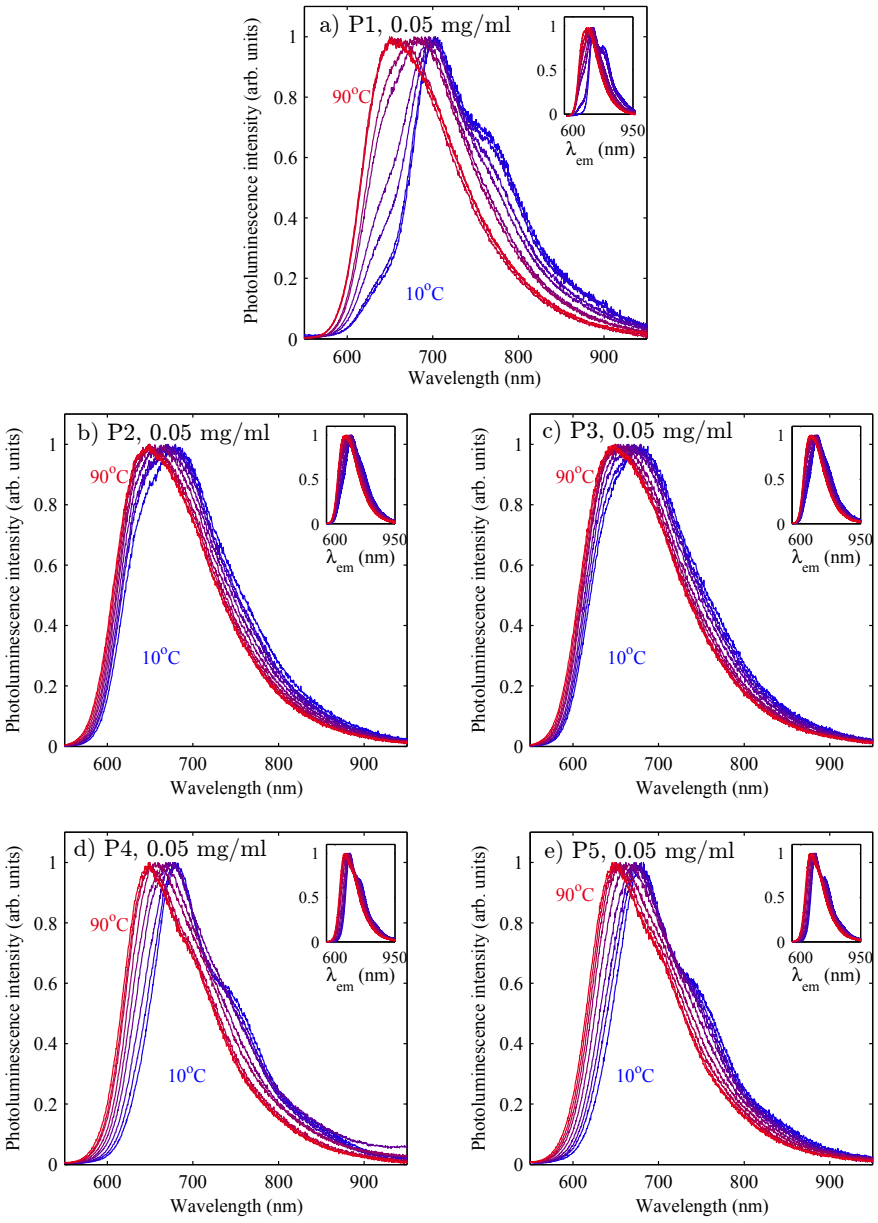

Figure 5.11: Time-integrated photoluminescence spectra for the polymers (a) P1, (b) P2, (c) P3, (d) P4 and (e) P5 solutions in *o*-DCB at concentrations of 0.05 mg mL^{-1} (main figure) and 5 mg mL^{-1} (inset). Spectra were measured after heating/cooling and allowing the temperature of the solution to stabilise at temperatures varying from 10°C (blue) to 90°C (red) in 10 ± 2°C steps. The solutions were excited at a wavelength of 450 nm. The suppressed shoulder at ∼ 620 nm, which increases in intensity on increasing temperature (complete dissolution of the polymer), is indicative of H-aggregate formation of P1 at low solution temperature. No such behaviour is evident in solutions of the P4 and P5, which form largely amorphous polymer films.

addition, those materials forming more crystalline polymer films, in particular P1 (Figure 5.11a) and to a lesser extent P2 (Fig. 5.11b) and P3 (Fig. 5.11c), exhibit a decrease in the relative intensity of the high-energy shoulder (620 nm) with decreasing solution temperature. Such deviations from spectra that can be modelled as standard Franck-Condon progressions are indicative of H-aggregate formation.[174] These effects are absent in solutions of P4 and P5, in agreement with the amorphous nature of thin films as evidenced by WAXS and AFM measurements.

These examinations show that the way in which emission transients and spectra of polymer solutions evolve with temperature is an accurate predictor of the resulting morphology in the cast thin films. Thin films with high surface roughness and a large degree of crystallinity are cast for polymers such as P1 that already in solution exhibit emission features and dynamics associated with chain aggregate formation. For polymers that form near-amorphous films (P4 and P5) such features are entirely absent in solution. Polymers P2 and P3 are found to be intermediate cases, show enhanced crystallinity and surface roughness in thin films, and some non-Condon progressions in solution spectra. These findings suggest that for this type of polymer, film morphology (and the related efficiency of photovoltaic devices) are intimately linked with clustering in solution prior to casting. Attaining control over polymer solubility is therefore an important goal to achieve for this class of polymer.

5.6 Conclusions

In summary, the effects of thin-film morphology on factors affecting photovoltaic performance for a series of donor-acceptor co-polymers comprising benzodithiophene and benzothiadiazole units have been investigated. It was found that the highest-performing polymers in photovoltaic devices based on polymer:$PC_{60}BM$ blends are those showing the least degree of crystallinity in X-ray diffraction patterns and a corresponding lowest surface roughness in thin films. The existence of such crystalline domains in thin polymer films correlates well with polymer chain aggregates being present already in solution prior to casting of the film. Polymer solubility and casting conditions therefore appear to be crucial factors for the development of photovoltaic devices with enhanced efficiencies. To examine why the presence of crystallite domains appears to hamper photovoltaic performance, exciton diffusion lengths were measured by modelling the observed migration of excitons through a thin polymer film deposited on a PL quencher layer of TiO_2. The observed diffusion lengths in

these materials are usual for low-bandgap polymers (4–7.5 nm) and show some variation between the different materials. However, ultrafast (1 ps) quenching of the PL from polymer:PCBM blends indicates that the vast majority of excitons created in polymer domains is not prevented from reaching an interface with PCBM and hence exciton diffusion does not represent a limiting factor. These observations suggest that the subsequent charge extraction and lifetimes must be adversely affected by the presence of crystalline domains. It should be noted that although extended crystalline polymer networks promote high hole mobilities within such domains,[15] the interfacial regions between well-ordered and amorphous polymer domains may act as energy barriers to charge transfer, forming sites at which charge trapping and recombination may occur with higher frequency.[200] The effect of the total polymer film crystallinity on the overall charge mobility is therefore a trade-off between these two factors. In materials such as P3HT[117] and some similar low-bandgap polymers[150] in which the polymer forms extended crystalline networks, the effect of in-domain charge mobility improvement will dominate and an increase in total crystallinity will enhance device efficiency. However, for polymers prone to the formation of small crystallites, an increase in total film crystallinity will increase the concentration of domain boundaries and hence lead to a reduction in overall charge mobility. The donor- acceptor polymers studied here clearly fall into the latter category and, as a result, polymers in this series appear to be the better suited for use in photovoltaic devices the more amorphous they are in the solid films. These results have important implications for the design of such donor-acceptor co-polymers for photovoltaics, suggesting that synthesis efforts may focus on creating polymers which exhibit sufficiently high inherent entropy.

Chapter 6

Electron and Hole Diffusion Lengths in Methylammonium Lead Halide Perovskites

6.1 Introduction

6.1.1 Background

Photovoltaic cells using an organic-inorganic hybrid perovskite material have become a vibrant field of study in renewable photovoltaics. In just a few short years since the first reported PV device incorporating these materials, power conversion efficiencies have rapidly increased from 3.8%[121] to 19.3%[248] and the number of reports in the literature concerning perovskites for use in photovoltaics has increased dramatically, from less than 10 in 2012 to nearly 700 in 2014. [1]

The first report by Kojima *et al.* in 2009 described a photovoltaic cell in which nanoparticles of $CH_3NH_3PbI_3$ were deposited on a mesoporous TiO_2 framework and embedded in a liquid electrolyte solution. This is a direct analogue of the device reported by Grätzel *et al.* in 1991,[172] a seminal paper which paved the way for the well established technology of dye sensitised solar cells (DSSC).

The general mechanism of operation for this device and DSSC in general is shown in Figure 6.1. Photon absorption and exciton formation in the sensitizer dye occurs initially (step 1), followed by ultrafast electron transfer to the conduction band of the ETM/metal oxide scaffold (step 2). Electron transport then takes place through this material to the electrode (step 3). In order to sustain electron injection into the metal oxide, regeneration of the oxidised sensitiser is required. This is achieved by redox

[1] As determined by a search for `"perovskite* AND solar"` in Web of Knowledge.

reaction between either a redox couple in solution (steps 4 and 5) or hole injection from a solid state hole tranport material (ssHTM). Finally, the oxidised member of the redox couple (or HTM) is reduced at the counter-electrode (step 6).[63]

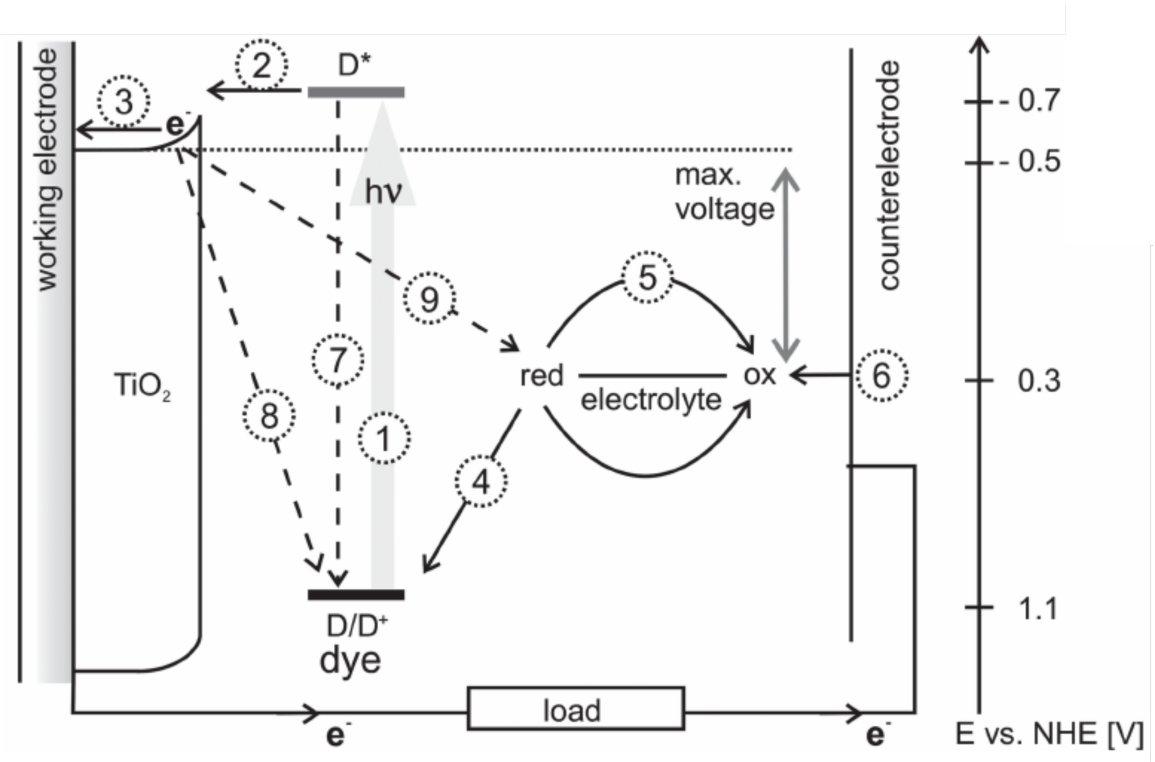

Figure 6.1: Energy level diagram of a DSSC with the fundamental processes labelled. Solid arrows are steps beneficial to charge production while dashed arrows are competing recombination processes: 1 - Photon absorption and exciton formation in the sensitizer dye; 2 - ultrafast electron transfer to the conduction band of the ETM/metal oxide scaffold; 3 - Electron transport through the ETM to the electrode; 4 - Regeneration of the oxidised sensitiser by electron transfer from the redox couple; 5 - hole transport or diffusion of the oxidised donor to the electrode; 6 - Regeneration of the HTM or redox donor at the electrode. Loss processes are: 7 - Decay of the dye excited state; 8 - Back transfer of the electron to the oxidised dye; 9 - Recombination of electrons in the ETM with the redox medium. (Taken from: Docampo et al., 2014)

Since the 7.2% power conversion efficiency reported in 1991,[172] the vast number of sensitizer dyes,[218;148;137;157;104;179] framework materials and geometries,[243;84;242] redox couples, and hole transport materials[169;241;48;232] have been the subject of numerous reviews. Through continuous research efforts, peak power conversion efficiencies have been steadily increasing, reaching 12.75%[239] and 7.2%[35] for liquid and solid state DSSC respectively.

Stability issues related to solvent evaporation and leakage, corrosion associated with the commonly used I^-/I_3^- redox couple, and diffusion limited rates of sensitiser regeneration with Co^{2+}/Co^{3+} couple[165] are major issues with the liquid electrolyte systems.

Although devices incorporating solid state hole transporters do not suffer from these same issues, the hole transport materials, in particular high molecular-weight polymers, are difficult to incorporate in the mesoporous metal-oxide structure with high volume fraction, although good charge extraction with *rr*-P3HT (regio-regular poly(3-hexyl thiophene)) has been reported.[1] Spiro-OMeTAD is an amorphous solid and is to date the best performing HTM.[35] It is more easily incorporated into the mesoporous structure than polymer HTMs, but has a low hole mobility unless charge carriers are added by doping. Excessive doping of spiro-OMeTAD however is detrimental to the device[35] as parasitic absorption occurs. The oxidised species absorbs strongly across the visible part of the spectrum and this reduces the amount of light that can be absorbed by the sensitiser material.

The optimum mesoporous layer thickness is then determined by trade off between pore filling and the light absorption by the sensitizer. With many organic dyes, the wavelength range over which absorption occurs is somewhat limited, and in general does not extend out to the near-infrared, so many of the incident photons are not absorbed. In addition, coverage is restricted to a monolayer in order to minimise the formation of H-aggregates which can reduce the efficiency of electron injection.[100]

Organic-inorganic perovskite materials do not suffer from these limitations however – high sensitizer loading can be achieved without any loss in electron injection efficiency,[103] and they have a stronger absorption across a wider spectral range than organic or Ruthenium based dyes.[121;103] This allows for a high photocurrent density in devices with even very thin mesostructured films.[116]

6.1.2 Perovskite Materials

The chemical formula of a perovskite material is ABX_3, and the structure can be described as a three dimensional network of corner sharing BX_6 octahedra with A ions occupying the cuboctahedral spaces as shown in Figure 6.2a. In the organic-inorganic hybrid materials, A^+ is a monovalent organic cation, B^{2+} is a divalent cation, usually Pb^{2+} or Sn^{2+}, and X^- are halide ions (Cl^-, Br^-, I^-). The range of cation sizes which will fit in these sites without much disturbing the PbI_6 network is described by the

tolerance factor, t, according to the equation $R_A + R_X = t\sqrt{2}(R_B + R_X)$, where R_A, R_B, and R_X are the ionic radii of the organic cation, metal cation and halide anions respectively. A value of t in the range $0.8 \geq t \geq 0.9$ is generally found for cubic perovskites.[83] As such, only very small cations with one or two carbon atoms can form 3D perovskites, by far the most commonly reported of which are methylammonium ($CH_3NH_3^+$)[212;121;103] and formamidinium ($CH_3(NH_2)_2^+$).[67;119;130] Much larger cations ($t > 1$) result in the formation of a 2D layered materials, with layers of MX_6 octahedra separated by a bilayer of organic cations as shown in Figure 6.2b.[158]

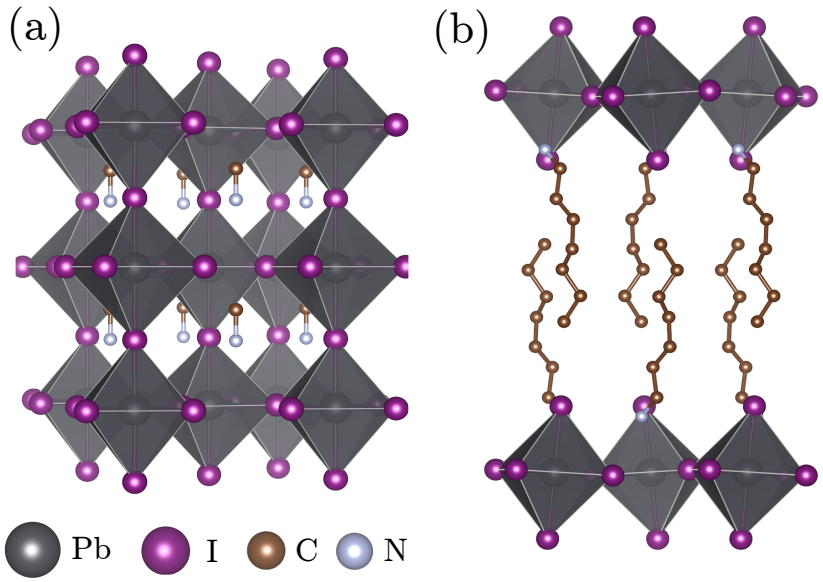

Figure 6.2: (a) 3D perovskite $CH_3NH_3PbI_3$ with a tetragonal structure at 293 K (β-phase structural data from ref[202]). There is a phase transition to a cubic structure at around 330 K. (b) 2D layered perovskite $(C_7H_{15}NH_3)_2PbI_4$ at 298 K with staggered $[PbI_4]^{2-}$ layers. The hydrogen atoms on the organic cations are not shown. (Structural data from: Lemmerer and Billing, 2012)

The optical properties of the 3D perovskites are determined by the choice of halide, metal ion and organic cation. Electronic structure calculations on $CH_3NH_3PbBr_3$ and $CH_3NH_3PbI_3$ show that states at the conduction band minimum are composed primarily of Pb-6*p*–halide-*np* (n=4 for Br, 5 for I) orbitals, while states at the valence band maximum are Pb-6*s*–halide-*np* in character.[40;216] The organic cation does not contribute directly to the CBM and VBM characteristics, but changing the A^+ cation can alter the bandgap indirectly by distortion of the lattice.[40]

One major benefit of these materials is the ease with which thin-films can be prepared. Methylammonium iodide and lead(II) iodide dissolve easily in many common

laboratory solvents, including acetone, N,N-dimethyl formamide, and acetonitrile. Spin-coating or drop-coating a solution containing a mixture of lead(II) iodide and methylammonium iodide, followed by a short annealing step will form the perovskite material of high enough quality to give 10% efficient solar cells.[121;103] More advanced procedures including a two-step deposition method, in which a solution of methylammoinum iodide is spin-coated on top of a pre-deposited lead(II) iodide film,[36] thermal evaporation,[143] and vapour-annealing techniques[42] have also been reported.

The first reported perovskite devices used simple spin-coating to form $CH_3NH_3PbX_3$ (X = Br or I) perovskite nanoparticles on the surface of a mesoporous TiO_2 scaffold and were direct analogues of the common DSSC structure with a solution of the $X^-/X_3{}^-$ was used as the redox couple. These early devices achieved power conversion efficiencies of 3.81%[121] and 6.5%[103] but were unstable for more than a few minutes as the perovskite was dissolved by the electrolyte.

Replacing the liquid electrolyte with a solid state hole-transporting material (ssHTM) in $CH_3NH_3PbI_3$ nanoparticle sensitized solar cells increased the cell stability and pushed the measured power conversion efficiency up to 9.7%.[116] This finding is in sharp contrast to previous reports on DSSC, for which liquid electrolytes have consistently out-performed ssHTM.[195;63;232] That perovskite solar cell operation can fundamentally differ from DSSC was reinforced when a device without any HTM[69] was shown to operate with 7.3% PCE as determined by fast I-V scans. Loading a mixed halide perovskite onto an electronically inert Al_2O_3 scaffold improved the PCE compared to an electron accepting TiO_2 scaffold by forcing the perovskite material to act as both an absorber and electron conductor,[131] and planar devices,[131;143] in which TiO_2 and spiro-OMeTAD only act as hole and electron blocking layers respectively. This shows that the perovskite material can act not only as a sensitizer, but can also conduct either electrons, holes, or both electrons and holes to the electrodes with low recombination losses. However, in the absence of HTM or ETM layers which act as electron or hole blocking layers respectively, the power conversion efficiency drops sharply when the device is held at the maximum power point. This effect is reduced when both a hole and electron blocking layer are present.[245]

The planar device geometry is of particular interest, as devices without a mesoporous structure are more easily prepared by low cost, large-scale, thin-film roll-to-roll printing methods.[124;123] One major advantage of planar structures is that the high-temperature (500 °C) sintering steps commonly used to prepare the mesoporous

layer[121;66] are no longer required. Such processing conditions are incompatible with the flexible substrates needed for roll-to-roll methods, although it should be noted that progress has recently been made on this front with the development of efficient meso-structure devices prepared entirely at low ($\leq$ 150°C) temperatures.[226;230] Removing the mesoporous layer also avoids issues associated with incomplete pore filling by the perovskite material which is associated with increased recombination losses[133] in meso-structured devices.

In order for solar cell devices to work efficiently, charges must be able to migrate through the perovskite material and reach the electrodes with high efficiency whether they are bound as an exciton or free-charge carriers. In this chapter, the method for measuring exciton diffusion lengths described in Chapter 5 is applied in to determine the average electron and hole diffusion lengths in films of two different methylammonium lead halide perovskite materials, the triiodide perovskite $CH_3NH_3PbI_3$, and the mixed halide perovskite $CH_3NH_3PbI_{3-x}Cl_x$. Materials in which the charge carriers have long diffusion lengths can be expected to perform well as part of a planar heterojunction device.

6.2 Experimental

6.2.1 Diffusion Length Measurements

In order to measure the electron and hole diffusion lengths in the perovskite films, the one-dimensional diffusion model described in Chapter 5 was applied to three thin film samples. In this case, the reference sample was coated with an insulating polymer to prevent degradation of the perovskite film in ambient atmosphere. The other two samples were coated with a layer of either a hole acceptor (spiro-OMeTAD), or an electron acceptor (Phenyl-C_{61}-butyric acid methyl ester, PCBM) material. Full details of the sample preparation methods are described in the following section, 6.2.2.

In this experiment, when the samples are excited with a short laser pulse the generated excitons begin to diffuse through the film which, in the case of the triiodide perovskite materials, was around 180 nm thick, while the mixed halide perovskite films were 250 nm thick. Since the initially generated exciton density is greatest at the glass/perovskite interface, net migration of excitons is toward the quencher layer. When some excitons reach the perovskite-quencher interface, charge transfer from the perovskite material to the quencher occurs. With the removal of an electron

(hole) from the perovskite film into the PCBM (spiro-OMeTAD) acceptor, there is no longer any chance for the removed charge to recombine radiatively with the hole (electron) left in the perovskite film. As the PL intensity is linearly proportional to the number of electron-hole pairs at low excitation densities, a faster decay of the total photoluminescence is observed when an acceptor layer is present, that is, the photoluminescence is partially quenched.

As the PL decay from the perovskite films could not be well described by a simple monoexponental decay for the perovskite materials measured, the reference PL was fit with a stretched exponential function

$$I(t) = I_0 \exp(-(t/\tau_s)^{\beta_s}), \tag{6.1}$$

where τ_s is the PL lifetime and β_s is the stretched exponent. A stretched exponential function was used in order to parametrise the decay rate in the absence of any quencher. This was required in order to accurately reproduce the "pure" perovskite PL decay rate in the model when calculating the electron and hole diffusion lengths and was not used to gain any insight into the radiative and non-radiative processes occurring. The total PL decay rate in Equation 5.2, was then given by

$$k_s(t) = k_f + k_{nr} = \beta_s \tau_s^{-\beta_s} t^{\beta_s - 1},$$

where as before, k_f is the rate of decay from the excited state by fluorescence, and k_{nr} is the non-radiative decay rate.

6.2.2 Sample Preparation

Films of $CH_3NH_3PbI_3$, $CH_3NH_3PbI_{3-x}Cl_x$ were prepared by S. Stranks as follows: A precursor solution was prepared by dissolving methylammonium iodide (MAI) and lead (II) iodide (or a mixture of lead (II) chloride and lead (II) iodide for the mixed halide perovskite) in anhydrous N,N-dimethylformamide, in a 3:1 ratio of MAI to PbX2. The final concentrations of lead halide and methylammonium iodide were 0.88 M and 2.64 M respectively.

To form the mixed halide film, the solution was spin-coated onto a onto a cleaned glass substrate (z-cut quartz, 13 mm diameter) at 2000 rpm in air, while the triiodide film was prepared by spin-coating a diluted version of the stock solution (1:1 in DMF) at 2000 rpm in air. The mixed halide films were annealed at 150°C for 15 minutes and the tri-iodide films were annealed at 100°C for 45 minutes. The final film thickness of

the mixed halide perovskite films were 250 ± 40 nm (PMMA capped film, see below) and 270 ± 40 nm (PCBM and spiro capped films, see below), and 180 ± 35 nm for the mixed halide.

Layers of capping materials were deposited on top of the perovskite material by spin coating solutions of either poly methylmethacrylate (PMMA, 10 mg/ml in chlorobenzene, spin coated at 1000 rpm), PCBM (30 mg/ml in chlorobenzene, spin coated at 1000 rpm) or spiro-OMeTAD (0.46 M in chlorobenzene, spin coated at 2000 rpm) on to one each of the mixed halide and tri-iodide films. Chlorobenzene was chosen as a solvent for the capping layers as the perovskite material is minimally soluble in this solvent, while the organic materials used here are dissolve easily. As such, it is assumed that there is no dissolution of the perovskite layer at the perovskite/quencher interface, and that there is no diffusion of the quencher material into the perovskite film. This is an important consideration for the calculation of electron hole diffusion lengths in these materials, as any diffusion of electron or hole acceptor materials into the perovskite film will result in a faster PL quenching and therefore overestimate of the diffusion length. The thickness of the perovskite film is an important parameter required in the model and was measured on a Veeco Dektak surface profilometer. UV-Vis absorption spectra of the films were recorded on a Varian Cary 300 spectrophotometer. Sample preparation and thin film characterisation were carried out by S. Stranks.

6.2.3 Time-Resolved Photoluminescence Measurements

The time-resolved photoluminescence measurements were measured using a FluoTime 300 time-correlated single photon counting setup by PicoQuant GmbH. Film samples were held at a 45° angle to the pulsed output of a 510 nm diode laser (LDH-P-C-510) powered by a picosecond pulsed diode laser driver (PDL 820). The pump beam was incident on the back (glass) face, and photoluminescence was measured at 90° from the same face. The photoluminescence was collected and monochromated with a FluoTime 300 spectrometer and detected with a PMA Hybrid 40 photomultiplier. The repetition rate of the pulsed source was varied between 0.3 and 10 MHz in order to observe the long lifetimes of the PMMA coated samples, without any wrap-around artefacts. The fluence incident on the samples was approximately 30 nJ/cm^2 and the pulse duration (FWHM) was 117 ps. The time resolved photoluminescence spectra, absorption spectra and stead-state PL spectra of the $CH_3NH_3PbI_3$ and CH_3NH_3

$PbI_{3-x}Cl_x$ films were recorded by S. Stranks. The IRF was measured by replacing the sample with a blank quartz slide and setting the detector to the pump wavelength of 510 nm.

6.3 Results and Discussion

The steady state absorption and photoluminescence spectra of the mixed halide and tri-iodide perovskite layers (PMMA capped) are plotted in the top parts of Figures 6.3 and 6.4 respectively. The absorption profile of each is broad with a sharp onset of absorption at around 770 nm, characteristic of the mixed organic-inorganic lead halide perovskites. The PL is narrow and centred at 770 nm for both the mixed halide and triiodide perovskites with very small shift in position relative to the absorption onset.

The bottom graph in Figures 6.3 and 6.4 are the time-resolved photoluminescence decays for the PMMA capped (grey squares), spiro-OMeTAD capped (blue circles), and PCBM capped (red diamonds). The result of the fitting routine is shown as a solid line with lighter colour (light blue for spiro, orange for PCBM) on top of the raw data. In each case, the sample was excited with pulses of wavelength $\lambda_{ex} = 510\,\text{nm}$ and the emission was detected at a wavelength of $\lambda_{em} = 770\,\text{nm}$. In the absence of any quencher, the observed fluorescence lifetime τ_e of the mixed halide perovskite is 273 ns, reducing to 5.1 (6.1) ns when capped with the electron (hole) acceptor, indicating diffusion through the film and quenching at the interface strongly competes with radiative recombination. The offsets observed in the curves measured from the spiro and PCBM capped layers at times $> 40\,\text{ps}$ are due to the background noise of the experiment and are not associated with any long-lived radiative species. Fitting with the single-particle diffusion model described previously, yielded values for the diffusion coefficients of 0.042 and $0.054\,\text{cm}^2\text{s}^{-1}$ for electrons and holes respectively. When combined with the fluorescence lifetime of 272 ns, a diffusion length of 1069 and 1213 nm are obtained. These are extremely long diffusion lengths when compared to those of organic solution processed materials which are usually on the order of $\approx$ 10 nm for disordered organic materials,[90;150;193;149] and are closer to the macroscopic diffusion lengths ($\approx 7\,\mu\text{m}$) of long lived triplet excitons that have been observed in pristine, single crystal organic solids.[163]

Photoluminescence from the triiodide perovskite in the absence of any quencher decays with a lifetime τ_e of 9.6 ns, much shorter than PL from the mixed-halide material. There is still rapid quenching of the PL when the PCBM or spiro acceptor

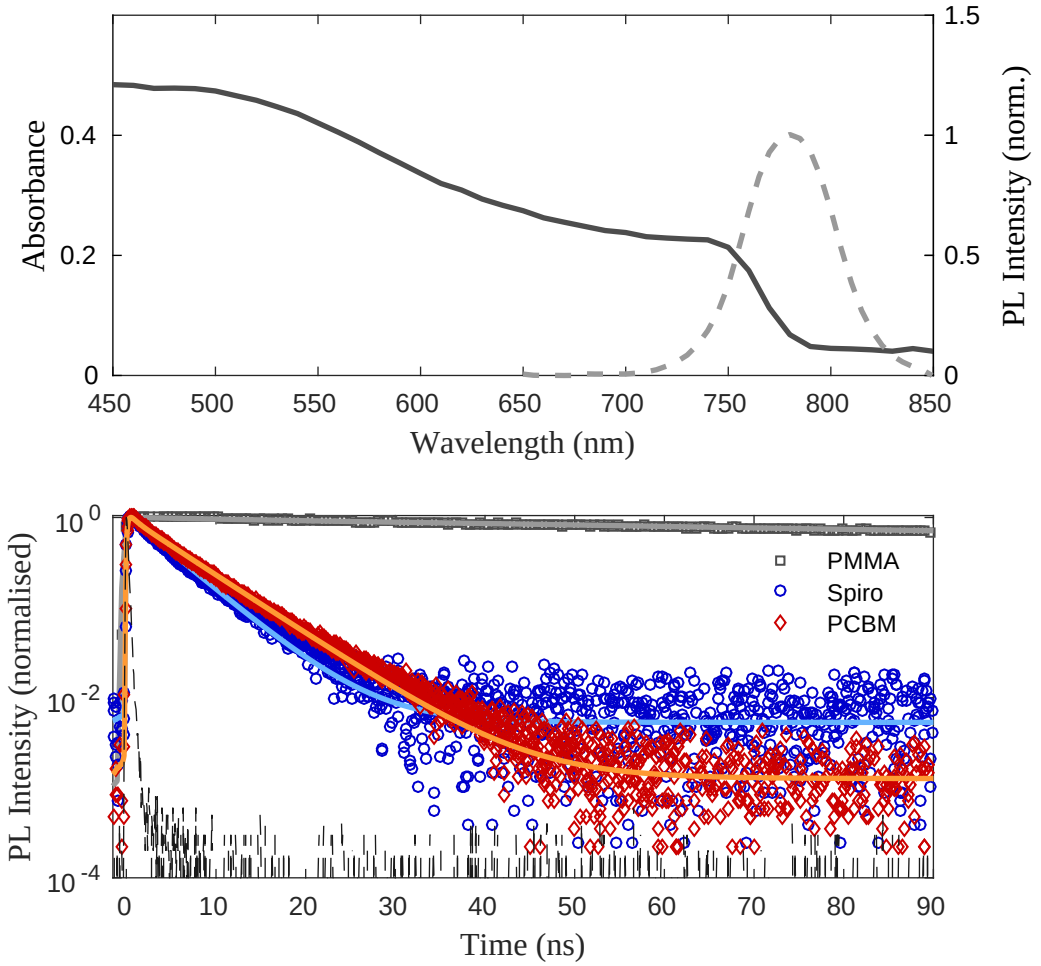

Quencher	$D\,(\mathrm{cm^2 s^{-1}})$	$\tau_e\,(\mathrm{ns})$	$L_D\,(\mathrm{nm})$	β_s	$\tau_s\,(\mathrm{ns})$
PMMA	-	272.65 ± 6.95	–	0.83 ± 0.03	285.7 ± 11.7
PCBM	0.042 ± 0.016	6.18 ± 0.10	1069 ± 204	-	-
Spiro-OMeTAD	0.054 ± 0.022	5.12 ± 0.06	1213 ± 243	-	-

Figure 6.3: Top: steady state absorption and photoluminescence from the PMMA capped mixed-halide perovskite, $CH_3NH_3PbI_{3-x}Cl_x$. The thickness of the perovskite material in the PMMA capped sample was 250 ± 40 nm, while the PCBM and spiro capped samples layers had a perovskite layer 270 ± 40 nm thick. Middle: Time-resolved photoluminescence decays from perovskite films capped with PMMA (grey squares), spiro-OMeTAD (blue circles), and PCBM (red diamonds). The fits for each sample obtained from the diffusion model are the lighter coloured solid lines. Each sample was excited through the glass substrate with a 510 nm wavelength and energy of 30 nJ/pulse. The instrument response function is included as a dashed black line. Offsets in the quenched sample curves are the noise floor of the experiment. Table: Parameters from the model described above. D the diffusion coefficient, τ_e the PL lifetime, L_D, mean diffusion length for electrons (with PCBM) and holes (with spiro-OMeTAD). τ_s and β_s are the lifetime and exponent defining the stretched exponential decay fit of the reference (PMMA capped) PL decay. *Experimental data measured by S. Stranks*

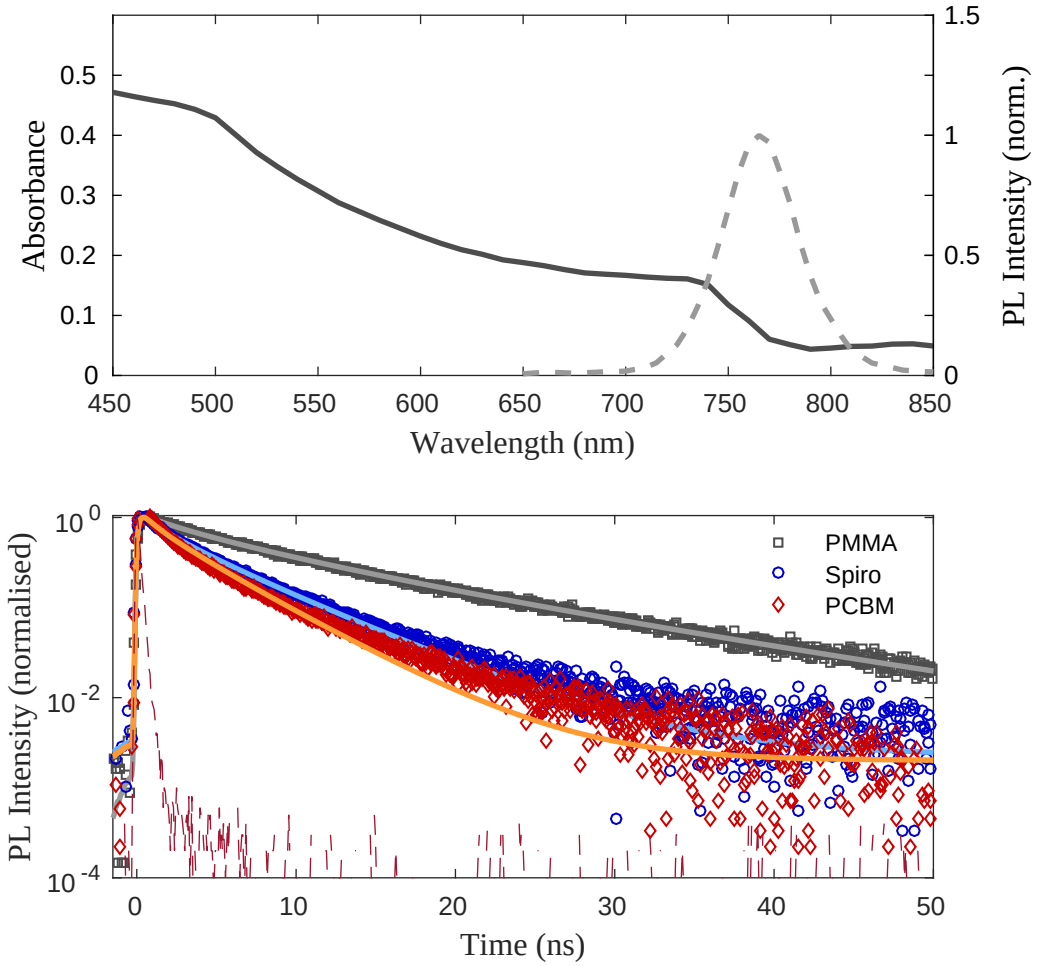

Quencher	D ($\mathrm{cm^2 s^{-1}}$)	τ_e (ns)	L_D (nm)	β_s	τ_s (ns)
PMMA	-	9.6 ± 0.26	-	0.77 ± 0.03	8.0 ± 0.32
PCBM	0.017 ± 0.011	3.17 ± 0.03	129 ± 41	-	-
Spiro-OMeTAD	0.011 ± 0.007	4.22 ± 0.06	105 ± 32	-	-

Figure 6.4: Top: steady state absorption and photoluminescence from the PMMA capped triiodide perovskite, $CH_3NH_3PbI_3$. The thickness of the perovskite material in each sample was 180 ± 35 nm. Middle: Time-resolved photoluminescence decays from perovskite films capped with PMMA (grey squares), PCBM (red diamonds) and spiro-OMeTAD (blue circles). The fits for each sample obtained from the diffusion model are the lighter coloured solid lines. Each sample was excited through the glass substrate with a 510 nm wavelength and energy of 30 nJ/pulse. The instrument response function is included as a dashed black line. Offsets in the quenched sample curves are the noise floor of the experiment. Table: Parameters from the model described above. D the diffusion coefficient, τ_e the PL lifetime, L_D, mean diffusion length for electrons (with PCBM) and holes (with spiro-OMeTAD). τ_s and β_s are the lifetime and exponent defining the stretched exponential decay fit of the reference (PMMA capped) PL decay. *Experimental data measured by S. Stranks*

layers are present, with the PL lifetimes reduced to 3.17 and 4.2 ns respectively. These correspond to diffusion coefficients of 0.017 and 0.011 cm^2s^{-1} for electrons and holes respectively resulting in exciton diffusion lengths of 129 and 105 nm when combined with the intrinsic PL lifetime from the reference sample. These values are an order of magnitude smaller than those observed in the mixed-halide perovskites. The mixed-halide electron and hole diffusion coefficients of 0.054 and 0.042 cm^2s^{-1} are approximately 3 times those of the triiodide, however the major difference between L_D values in the two materials arises from the difference in intrinsic PL lifetimes, as PL in the mixed-halide takes nearly 30 times longer than in the triiodide to reach $1/e$ of the initial intensity.

Perovskite	L (nm)	J_{SC} (mA cm^{-2})	V_{OC} (V)	Fill Factor	PCE (%)
$CH_3NH_3PbI_{3-x}Cl_x$	500	13.1 ± 4.3	0.89 ± 0.1	0.59 ± 0.14	7.8 ± 4.0
		17.9	**0.97**	**0.7**	**12.2**
$CH_3NH_3PbI_3$	140	7.7 ± 3.4	0.72 ± 0.08	0.44 ± 0.09	2.3 ± 1.3
		13.2	**0.71**	**0.45**	**4.2**

Table 6.1: Photovoltaic device characteristics, optimum perovskite thickness, L, short-circuit current, J_{SC}, open-circuit voltage, V_{OC}, fill factor, and power conversion efficiency of the mixed-halide and triiodide perovskite devices. The mean value for each property and the standard deviation for the whole batch are listed. The values in bold correspond to the best performing cell from each batch. *Devices prepared and characterised by G. Eperon.*

This large difference in diffusion lengths is reflected in the device characteristics of PV cells made from the two materials and the perovskite thickness in optimized solar cells. These are summarised in Table 6.1. The optimum thickness for the mixed-halide perovskite solar cells was around 500 nm compared to 140 nm for the triiodide.[203] This limitation is primarily imposed by the much shorter electron-hole diffusion length. Due to the high attenuation coefficient (α in Equation 5.1) in perovskite materials, most of the incident photons are absorbed within a few hundred nanometres. If the film thickness is much longer than the diffusion length for electrons and holes in these materials, a high percentage of generated charges will decay before reaching the electrodes of the solar cell. Figure 6.5 shows the extraction efficiency as a function of perovskite layer thickness, with extraction efficiency defined as the number of charges reaching the far edge of the perovskite film divided by the total number of photons absorbed. For the triiodide, with attenuation coefficient $\alpha = 27000$ cm^{-1}, only 50% of the absorbed photons will result in photogenerated charges reaching the

top edge of a 160 nm thick perovskite film when the diffusion length is 100 nm. For the mixed-halide material with diffusion length longer than 1000 nm, there are no such constraints on the maximum film thickness. This allows for thicker films in optimised mixed-halide perovskite devices with higher total photon absorption and therefore higher short-circuit currents than in the thinner triiodide cells.

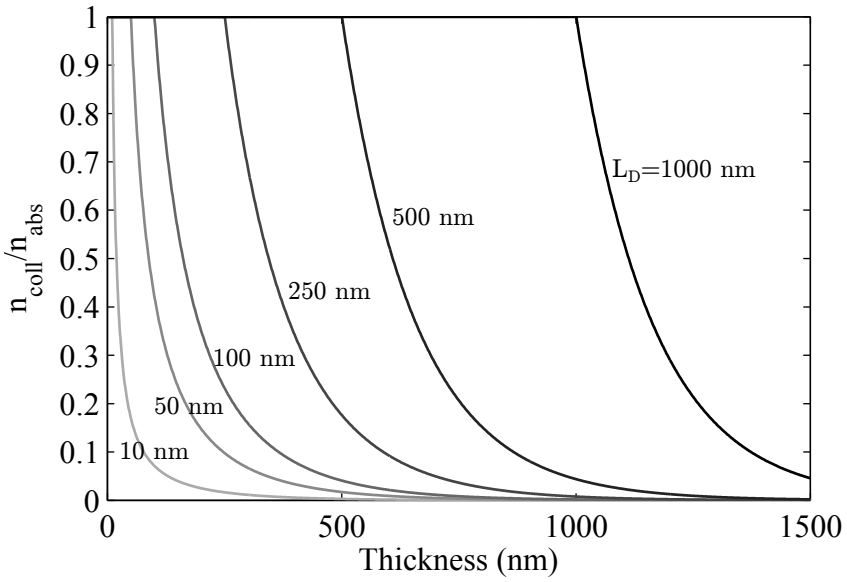

Figure 6.5: Simulated collection efficiency n_{coll}/n_{abs} as a function of total film thickness and diffusion length for a film with attenuation coefficient $\alpha = 27000\,\mathrm{cm}^{-1}$, comparable to that of the triiodide perovskite at 510 nm.

As the materials spiro-OMeTAD and PCBM are used regularly by many PV research groups, and the TCSPC technique is commonly used, measurement of the the electron and hole diffusion lengths in a given perovskite material is a simple and useful indicator as to whether this material is suitable for use in planar devices, circumventing the need to fabricate and test multiple cells of varying perovskite thickness.

In the model, the population of only one single mobile species is considered but the use of quenchers which are selective to either electrons or holes allows for the diffusion coefficient and diffusion length of each to be obtained. As the electron and hole diffusion coefficients are similar in both perovskite materials, it is not possible to determine whether transport through the film takes place as a bound exciton or free charges. The difference between the $0.042\,\mathrm{cm}^2\mathrm{s}^{-1}$, 1069 nm and $0.054\,\mathrm{cm}^2\mathrm{s}^{-1}$, 1213 nm for the electron and hole diffusion coefficients and diffusion lengths could be due to a real difference in mobility in the film between the two charges if they travel

independently of each other, or could be due to a difference in quenching efficiency between the PCBM and spiro-OMeTAD, both of which were assumed to be unity.

Whether the major charge carrier species in these perovskite films are bound excitons or free charges has been the subject of discussion in the literature [204;233;207;62]. The exciton binding energy in the triiodide material has been reported as ranging between 19 and 55 meV, [107;212;208;62] depending on the measurement technique used. These values are all comparable to $k_BT \approx 25$ meV at room temperature, and correspond to between 50 and 90% of the generated electron-hole pairs remaining bound as excitons according to the Boltzmann distribution. As the splitting of excitons into free charges is an equilibrium between species rather than just a distribution amongst different energy states, D'Innocenzo *et al.* applied the Saha-Langmuir equation to calculate the ratio of free charges to excitons as a function of temperature, population density and exciton binding energy. They found that under standard device operation conditions, electrons and holes exist almost entirely as free charges and not as weakly bound excitons. [62] This agrees with the finding that PL arises solely from free charge recombination by Yamada *et al.* [233] and is likely the reason for the absence of any discernible exciton peak in absorption spectra of the perovskite films at room temperature.

Accurate values for the diffusion coefficient can be obtained providing the decay rate for the charge carrier as determined by fitting the reference sample PL decay is still applicable to the PL films in contact with the quencher. This is the case for the mixed halide sample, as the 30 nJ/pulse excitation power used in the TCSPC measurement corresponds to $\sim 10^{15}$ cm^{-3} excitation density, a level at which recombination is predominantly mono-molecular [228]. For the triiodide material, the bimolecular recombination mechanism begins to make a larger contribution at these fluences [228;233]. As such, the reference PL parameters may not adequately describe electron and hole densities leading to the slight discrepancy between the fit and data in the 20–35 ns window for the spiro-OMeTAD sample. In general however, the quality of the fits is high and allows for confident determination of the electron and hole diffusion lengths in these materials.

6.4 Conclusion

A simple method of determining the diffusion length of electrons (holes) by comparing photoluminescence decays with and without an electron (hole) acceptor layer has

been applied to methylammonium halide perovskite films. Diffusion coefficients of 4.2×10^{-2} and $5.4 \times 10^{-2}\,\mathrm{cm^2 s^{-1}}$ were found for electrons and holes respectively in a film of the mixed-halide perovskite, $CH_3NH_3PbI_{3-x}Cl_x$, and values of 1.1×10^{-2} and $1.7 \times 10^{-2}\,\mathrm{cm^2 s^{-1}}$ for the triiodide $CH_3NH_3PbI_3$, approximately one order of magnitude larger than the $\sim 1 \times 10^{-3}\,\mathrm{cm^2 s^{-1}}$ values observed in other solution processable materials. Due to the long radiative lifetimes of $\sim 9\,\mathrm{ns}$ and $\sim 270\,\mathrm{ns}$ for the triiodide and mixed halide matierals, electron-hole diffusion lengths exceed 100 nm in the triiodide and 1 µm in the mixed halide. This method is therefore a useful tool to determine the suitability of a given perovskite material for use in planar solar cells since it is the diffusion length which limits the number of generated electron-hole pairs that can reach the electrodes and hence the maximum film thickness and amount of incident light that can be absorbed in planar devices.

Chapter 7

Conclusions

Through the experiments described in this thesis, the key energy transport processes in hybrid organic-inorganic perovskites, a series of conjugated low-bandgap polymers, and two donor-acceptor-donor triad dyes have been investigated. Each of these material classes show promise for use in solar energy conversion, either as the active layer of photovoltaic cells or as the luminophore in solar concentrator devices. Efficient energy transfer is crucial for the efficient operation of each of these devices, whether it be migration of excitons to the heterojunction in an organic photovoltaic device in order to form free charges, long range transport through a flat perovskite film to the ETM/HTM in perovskite photovoltaics, or intramolecular energy transfer in triad dyes to minimise escape and self-absorption losses in luminescence solar concentrators. Ultrafast photoluminescence spectroscopy has been shown to be well suited to measuring these energy transport processes by monitoring the photoluminescence decay in the presence of quencher materials, or monitoring transient PL originating in different chromophores within a single molecule.

The results of the experiments described in this thesis are briefly summarised, and suggestions for further work are given below.

In Chapter 4, the rate of intramolecular energy transfer in two donor-acceptor-donor triad dyes was measured by monitoring the photoluminescence decay dynamics at wavelengths specific to emission from the donor and acceptor units on the dye, as well as by monitoring the evolution of the emission spectrum at short times after excitation. It was observed that rapid energy transfer takes place in less than 2 ps in both the dye in which the transition dipole moments of the donor and acceptor units are collinear, and the triad in which the acceptor transition dipole moment is orthogonal to those of the two donor units. Such rapid energy transfer is expected

for the linear triad by Förster's point-dipole model, however energy transfer in the orthogonal case is expected to be zero by this model.

A distributed-dipole model was used to explore the effect of the breakdown in the point-dipole model due to the close proximity of the donor and acceptor units, along with the possible effect of a break in orthogonality between the dipole moments by bending about the bond linking the two. While this modified Förster model was able to predict the rapid energy transfer rate in the linear triad, it severely underestimates it for the orthogonal case. The observed rapid rates were found to be due to a combination of through-space and through-bond energy transfer involving direct interaction between the subunits. Measurement of the PL anisotropy showed that the rapid and efficient energy transfer allows for control of the emission polarisation relative to the polarisation of absorbed light by through control of the relative orientation of the donor and acceptor units during synthesis. These are essential features of dyes for use in luminescent solar concentrators which have low self-absorption and surface losses.

In Chapter 5, the influence of thin-film morphology on energy transfer and the overall photovoltaic performance for a series of low-bandgap conjugated polymers containing benzodithiophene and benzothiadiazole donor and acceptor subunits was investigated. It was found that the polymers which yielded devices with the highest power conversion efficiencies when blended with $PC_{60}BM$ from the series were those which formed the most amorphous films with very low surface roughness as determined by wide-angle x-ray scattering and atomic force microscopy. The formation of crystalline domains in films of the low-performance polymers correlates well with the observation of aggregate formation in solution at conditions similar to those during device fabrication.

The presence of crystallite domains result in a longer exciton diffusion length (7.5 nm) relative to that observed in the more amorphous films (4 nm), however in both the systems the vast majority of excitons can easily reach a polymer:PCBM interface, which was observed as an ultrafast (< 1 ps) quenching of almost all the polymer photoluminescence. These observations suggest that the observed reduction in device performance for all but the most amorphous films, that is, whenever a sizeable number of crystalline domains are present, arises from losses during the charge-transfer state dissociation and migration to the electrodes. This is likely to be due to charge trapping at the boundary between regions of ordered and amorphous polymer

domains. For this class of bezodithiophene-*co*-benzothiadiazole polymers therefore, synthesis of co-polymers which form amorphous films are beneficial to photovoltaic device performance.

In Chapter 6, the diffusion length of electron and holes in two organic-inorganic perovskite materials, $CH_3NH_3PbI_3$ and $CH_3NH_3PbI_{3-x}Cl_x$, were determined by comparing the rate of photoluminescence quenching in the presence of an electron acceptor (PCBM) or hole acceptor (spiro-OMeTAD) with that of a control sample without the acceptor layer. For the mixed halide perovskite, extremely long diffusion lengths of over 1 micrometre were observed for both electrons (1069 nm) and holes (1213 nm). In contrast, the diffusion lengths in the triiodide material are an order of magnitude shorter, around $\sim$ 100 nm, yet still much greater than those commonly reported in other solution processable materials. These long diffusion lengths arise from a combination of both increased diffusion coefficient and long carrier lifetimes. The distance over which carriers can migrate is vitally important for planar devices lacking the mesoporous scaffold which is a common feature in many perovskite solar cells. Application of this method to determine diffusion lengths can therefore provide a simple means by which to predict whether a given perovskite material is suitable for use in planar devices.

Future Work

Further to the studies of energy transfer in the triad dyes described in Chapter 4, more advanced calculations to determine the degree of through-bond interaction between the donor and acceptor units could be interesting from a fundamental physics viewpoint. From a more applied viewpoint, it would also be useful to determine the efficiency of LSC devices incorporating these triad dyes based on their suitability for such applications as described in this thesis.

In light of recent studies in which electrons and holes were found to predominantly exist as free carriers rather than excitons in the perovskite films,[62;233] refinements to the model described in Chapter 6 could prove to be a useful avenue for future research. In particular, accounting for the populations of electrons and holes individually rather than treating them a single mobile species may result in improved fit quality, especially if diffusion lengths under conditions of higher excitation fluence regimes are of interest. This would require however that the rates of recombination be determined separately and used as parameters in the model, rendering the technique less applicable as a

simple method for determining the suitability of a given material for use in planar PV devices.

References

[1] A. Abrusci, I.-K. Ding, M. Al-Hashimi, T. Segal-Peretz, M. D. McGehee, M. Heeney, G. L. Frey, and H. J. Snaith. Facile Infiltration of Semiconducting Polymer into Mesoporous Electrodes for Hybrid Solar Cells. *Energy & Environmental Science*, 4:3051–3058, 2011.

[2] M. Adachi and Y. Nagao. Design of near-Infrared Dyes Based on π-Conjugation System Extension 2. Theoretical Elucidation of Framework Extended Derivatives of Perylene Chromophore. *Chemistry of Materials*, 13:662–669, 2001.

[3] I. E. Agency. Technology Roadmap. Technical report, 2014.

[4] G. M. Akselrod, P. B. Deotare, N. J. Thompson, J. Lee, W. A. Tisdale, M. A. Baldo, V. M. Menon, and V. Bulović. Visualization of Exciton Transport in Ordered and Disordered Molecular Solids. *Nature Communications*, 5:3646, 2014.

[5] B. Albinsson, M. P. Eng, K. Pettersson, and M. U. Winters. Electron and Energy Transfer in Donor-acceptor Systems with Conjugated Molecular Bridges. *Physical Chemistry Chemical Physics*, 9:5847–64, 2007.

[6] A. J. Alfano, F. E. Lytle, M. S. Showell, and F. K. Fong. Excited Singlet-State Lifetimes of Hydrated Chlorophyll Aggregates. *The Journal of Chemical Physics*, 82:758–764, 1985.

[7] S. Alvarado, P. Seidler, D. Lidzey, and D. Bradley. Direct Determination of the Exciton Binding Energy of Conjugated Polymers Using a Scanning Tunneling Microscope. *Physical Review Letters*, 81:1082–1085, 1998.

[8] Z. An, C. Q. Wu, and X. Sun. Dynamics of Photogenerated Polarons in Conjugated Polymers. *Physical Review Letters*, 93:216407, 2004.

[9] H. Asanuma, T. Fujii, T. Kato, and H. Kashida. Coherent Interactions of Dyes Assembled on DNA. *Journal of Photochemistry and Photobiology C: Photochemistry Reviews*, 13:124–135, 2012.

[10] P. W. Atkins and R. S. Friedman. *Molecular Quantum Mechanics*. Oxford University Press, 3rd edition, 1997.

[11] P. W. Atkins and J. Paula. *Physical Chemistry*. Oxford University Press, 8th edition, 2006.

[12] A. A. Bakulin, A. Rao, V. G. Pavelyev, P. H. M. van Loosdrecht, M. S. Pshenichnikov, D. Niedzialek, J. Cornil, D. Beljonne, and R. H. Friend. The Role of Driving Energy and Delocalized States for Charge Separation in Organic Semiconductors. *Science*, 335:1340–1344, 2012.

[13] B. Balaban, S. Doshay, M. Osborn, Y. Rodriguez, and S. A. Carter. The Role of FRET in Solar Concentrator Efficiency and Color Tunability. *Journal of Luminescence*, 146:256–262, 2014.

[14] N. Banerji, S. Cowan, M. Leclerc, E. Vauthey, and A. J. Heeger. Exciton Formation, Relaxation, and Decay in PCDTBT. *Journal of the American Chemical Society*, 132:17459–70, 2010.

[15] Z. Bao, A. Dodabalapur, and A. J. Lovinger. Soluble and Processable Regioregular Poly (3-hexylthiophene) for Thin Film Field-effect Transistor Applications with High Mobility. *Applied Physics Letters*, 69:4108–4110, 1996.

[16] W. Barford. *Electronic and Optical Properties of Conjugated Polymers*. Oxford University Press, 2005.

[17] M. D. M. Barnes and M. Baghar. Optical Probes of Chain Packing Structure and Exciton Dynamics in Polythiophene Films, Composites, and Nanostructures. *Journal of Polymer Science Part B: Polymer Physics*, 50:1121–1129, 2012.

[18] H. Bässler. Charge Transport in Disordered Organic Photoconductors a Monte Carlo Simulation Study. *Physica Status Solidi (b)*, 175:15–56, 1993.

[19] J. S. Batchelder, A. H. Zewail, and T. Cole. Luminescent Solar Concentrators. 1: Theory of Operation and Techniques for Performance Evaluation. *Applied Optics*, 18:3090–3110, 1979.

[20] W. Becker. *The bh TCSPC Handbook*. Becker & Hickl GmbH, 5th edition edition, 2010.

[21] W. J. D. Beenken and T. Pullerits. Excitonic Coupling in Polythiophenes: Comparison of Different Calculation Methods. *The Journal of Chemical Physics*, 120:2490–2495, 2004.

[22] Z. M. Beiley, E. T. Hoke, R. Noriega, J. Dacuña, G. F. Burkhard, J. A. Bartelt, A. Salleo, M. F. Toney, M. D. McGehee, and J. Dacuna. Morphology-Dependent Trap Formation in High Performance Polymer Bulk Heterojunction Solar Cells. *Advanced Energy Materials*, 1:954–962, 2011.

[23] D. Beljonne, Z. Shuai, G. Pourtois, and J. L. Bredas. Spin–Orbit Coupling and Intersystem Crossing in Conjugated Polymers: A Configuration Interaction Description. *The Journal of Physical Chemistry A*, 105:3899–3907, 2001.

[24] D. Beljonne, G. Pourtois, C. Silva, E. Hennebicq, L. M. Herz, R. H. Friend, G. D. Scholes, S. Setayesh, K. Mullen, and J. L. Bredas. Interchain Vs. Intrachain Energy Transfer in Acceptor-capped Conjugated Polymers. *Proceedings of the National Academy of Sciences of the United States of America*, 99:10982–10987, 2002.

[25] A. R. Bishop, D. K. Campbell, and K. Fesser. Polyacetylene and Relativistic Field Theory Models. *Molecular Crystals and Liquid Crystals*, 77:253–264, 1981.

[26] J. Blatchford, S. Jessen, L. Lin, J. Lih, T. Gustafson, A. Epstein, D. Fu, M. Marsella, T. Swager, A. MacDiarmid, S. Yamaguchi, and H. Hamaguchi. Exciton Dynamics in Poly(p-Pyridyl Vinylene). *Physical Review Letters*, 76: 1513–1516, 1996.

[27] R. W. Boyd. *Nonlinear Optics*. Elsevier, 2003.

[28] C. J. Brabec. Organic Photovoltaics: Technology and Market. *Solar Energy Materials and Solar Cells*, 83:273–292, 2004.

[29] C. J. Brabec, S. Gowrisanker, J. J. M. Halls, D. Laird, S. Jia, and S. P. Williams. Polymer-Fullerene Bulk-heterojunction Solar Cells. *Advanced Materials*, 22: 3839–3856, 2010.

[30] J.-L. Brédas, J. Cornil, and A. J. Heeger. The Exciton Binding Energy in Luminescent Conjugated Polymers. *Advanced Materials*, 8:447–452, 1996.

[31] P. Brown, D. Thomas, A. Köhler, J. Wilson, J.-S. Kim, C. Ramsdale, H. Sirringhaus, and R. Friend. Effect of Interchain Interactions on the Absorption and Emission of Poly(3-hexylthiophene). *Physical Review B*, 67:064203, 2003.

[32] E. Bundgaard and F. C. Krebs. Low Band Gap Polymers for Organic Photovoltaics. *Solar Energy Materials and Solar Cells*, 91:954–985, 2007.

[33] J. H. Burroughes, D. D. C. Bradley, A. R. Brown, R. N. Marks, K. Mackay, R. H. Friend, P. L. Burns, and A. B. Holmes. Light-emitting Diodes Based on Conjugated Polymers. *Nature*, 347:539–541, 1990.

[34] H. D. Burrows, J. Seixas de Melo, C. Serpa, L. G. Arnaut, A. P. Monkman, I. Hamblett, and S. Navaratnam. S_1 to T_1 Intersystem Crossing in π-conjugated Organic Polymers. *The Journal of Chemical Physics*, 115:9601–9606, 2001.

[35] J. Burschka, A. Dualeh, F. Kessler, E. Baranoff, N.-L. Cevey-Ha, C. Yi, M. K. Nazeeruddin, and M. Grätzel. Tris(2-(1H-pyrazol-1-yl)pyridine)cobalt(III) as p-type Dopant for Organic Semiconductors and Its Application in Highly Efficient Solid-State Dye-sensitized Solar Cells. *Journal of the American Chemical Society*, 133:18042–18045, 2011.

[36] J. Burschka, N. Pellet, S.-J. Moon, R. Humphry-Baker, P. Gao, M. K. Nazeeruddin, and M. Grätzel. Sequential Deposition as a Route to High-performance Perovskite-sensitized Solar Cells. *Nature*, 499:316–319, 2013.

[37] M. Chandross and S. Mazumdar. Coulomb Interactions and Linear, Nonlinear, and Triplet Absorption in Poly(para-phenylenevinylene). *Physical Review B*, 55:1497–1504, 1997.

[38] M. Chandross, S. Mazumdar, S. Jeglinski, X. Wei, Z. V. Vardeny, E. W. Kwock, and T. M. Miller. Excitons in Poly(para-phenylenevinylene). *Physical Review B*, 50:14702–14705, 1994.

[39] R. Chang, J. Hsu, W. Fann, K. Liang, C. Chang, M. Hayashi, J. Yu, S. Lin, E. Chang, K. Chuang, and S. Chen. Experimental and Theoretical Investigations of Absorption and Emission Spectra of the Light-emitting Polymer MEH-PPV in Solution. *Chemical Physics Letters*, 317:142–152, 2000.

[40] Y. Chang, C. Park, and K. Matsuishi. First-Principles Study of the Structural and the Electronic Properties of the Lead-Halide-Based Inorganic-Organic Perovskites (CH_3NH_3) PbX_3 and $CsPbX_3$ (X = Cl, Br, I). *Journal of the Korean Physical Society*, 44:889–893, 2004.

[41] D. M. Chapin, C. S. Fuller, and G. L. Pearson. A New Silicon p-n Junction Photocell for Converting Solar Radiation into Electrical Power. *Journal of Applied Physics*, 25:676, 1954.

[42] Q. Chen, H. Zhou, Z. Hong, S. Luo, H.-s. Duan, H.-h. Wang, Y. Liu, G. Li, and Y. Yang. Planar Heterojunction Perovskite Solar Cells Via Vapor-assisted Solution Process. *Journal of the American Chemical Society*, 136:622–5, 2014.

[43] Z. Chen, U. Baumeister, C. Tschierske, and F. Würthner. Effect of Core Twisting on Self-assembly and Optical Properties of Perylene Bisimide Dyes in Solution and Columnar Liquid Crystalline Phases. *Chemistry*, 13:450–65, 2007.

[44] Z. Chen, A. Lohr, C. R. Saha-Möller, and F. Würthner. Self-assembled Pi-stacks of Functional Dyes in Solution: Structural and Thermodynamic Features. *Chemical Society Reviews*, 38:564–84, 2009.

[45] T. M. Clarke and J. R. Durrant. Charge Photogeneration in Organic Solar Cells. *Chemical Reviews*, 110:6736–67, 2010.

[46] R. M. Clegg. *Fret and Flim Techniques*. Elsevier, 2009.

[47] K. M. Coakley, B. S. Srinivasan, J. M. Ziebarth, C. Goh, Y. Liu, and M. D. McGehee. Enhanced Hole Mobility in Regioregular Polythiophene Infiltrated in Straight Nanopores. *Advanced Functional Materials*, 15:1927–1932, 2005.

[48] J. Cong, X. Yang, L. Kloo, and L. Sun. Iodine/iodide-free Redox Shuttles for Liquid Electrolyte-based Dye-sensitized Solar Cells. *Energy & Environmental Science*, 5:9180, 2012.

[49] E. Conwell. Definition of Exciton Binding Energy for Conducting Polymers. *Synthetic Metals*, 83:101–102, 1996.

[50] S. Cook, A. Furube, and R. Katoh. Analysis of the Excited States of Regioregular Polythiophene P3HT. *Energy & Environmental Science*, 1:294–299, 2008.

[51] J. Crank and P. Nicolson. A Practical Method for Numerical Evaluation of Solutions of Partial Differential Equations of the Heat-conduction Type. *Advances in Computational Mathematics*, 6:207–226, 1996.

[52] M. T. Dang, L. Hirsch, G. Wantz, and J. D. Wuest. Controlling the Morphology and Performance of Bulk Heterojunctions in Solar Cells. Lessons Learned from the Benchmark Poly(3-hexylthiophene):[6,6]-Phenyl-C61-butyric Acid Methyl Ester System. *Chemical Reviews*, 113:3734–65, 2013.

[53] D. Dasgupta, A. M. Kendhale, M. G. Debije, J. ter Schiphorst, I. K. Shishmanova, G. Portale, and A. P. H. J. Schenning. Effect of the Ortho Alkylation of Perylene Bisimides on the Alignment and Self-assembly Properties. *ChemistryOpen*, 3:138–41, 2014.

[54] J. C. de Mello, H. F. Wittmann, and R. H. Friend. An Improved Experimental Determination of External Photoluminescence Quantum Efficiency. *Advanced Materials*, 9:230–232, 1997.

[55] M. G. Debije and P. P. C. Verbunt. Thirty Years of Luminescent Solar Concentrator Research: Solar Energy for the Built Environment. *Advanced Energy Materials*, 2:12–35, 2012.

[56] M. G. Debije, P. P. C. Verbunt, B. C. Rowan, B. S. Richards, and T. L. Hoeks. Measured Surface Loss from Luminescent Solar Concentrator Waveguides. *Applied Optics*, 47:6763, 2008.

[57] M. G. Debije, C. Menelaou, L. M. Herz, and A. P. H. J. Schenning. Combining Positive and Negative Dichroic Fluorophores for Advanced Light Management in Luminescent Solar Concentrators. *Advanced Optical Materials*, 2:687–693, 2014.

[58] M. Demokan and A. Nacaroglu. An Analysis of Gain-switched Semiconductor Lasers Generating Pulse-code-modulated Light with a High Bit Rate. *IEEE Journal of Quantum Electronics*, 20:1016–1022, 1984.

[59] W. Demtröder. *Laser Spectroscopy: Vol. 2: Experimental Techniques*. Springer, 2008.

[60] D. L. Dexter. A Theory of Sensitized Luminescence in Solids. *The Journal of Chemical Physics*, 21:836, 1953.

[61] A. Dhanabalan, J. K. J. Van Duren, P. A. Van Hal, J. L. J. Van Dongen, and R. A. J. Janssen. Synthesis and Characterization of a Low Bandgap Conjugated Polymer for Bulk Heterojunction Photovoltaic Cells. *Advanced Functional Materials*, 11:255–262, 2001.

[62] V. D'Innocenzo, G. Grancini, M. J. P. Alcocer, A. R. S. Kandada, S. D. Stranks, M. M. Lee, G. Lanzani, H. J. Snaith, and A. Petrozza. Excitons Versus Free Charges in Organo-lead Tri-halide Perovskites. *Nature Communications*, 5: 3586, 2014.

[63] P. Docampo, S. Guldin, T. Leijtens, N. K. Noel, U. Steiner, and H. J. Snaith. Lessons Learned: from Dye-sensitized Solar Cells to All-Solid-State Hybrid Devices. *Advanced Materials*, 26:4013–30, 2014.

[64] S. Ebadian, B. Gholamkhass, S. Shambayati, S. Holdcroft, and P. Servati. Effects of Annealing and Degradation on Regioregular Polythiophene-based Bulk Heterojunction Organic Photovoltaic Devices. *Solar Energy Materials and Solar Cells*, 94:2258–2264, 2010.

[65] M. P. Eng and B. Albinsson. Non-exponential Distance Dependence of Bridge-mediated Electronic Coupling. *Angewandte Chemie (International Ed. In English)*, 45:5626–9, 2006.

[66] G. E. Eperon, V. M. Burlakov, A. Goriely, and H. J. Snaith. Neutral Color Semitransparent Microstructured Perovskite Solar Cells. *ACS Nano*, 8:591–8, 2014.

[67] G. E. Eperon, S. D. Stranks, C. Menelaou, M. B. Johnston, L. M. Herz, and H. J. Snaith. Formamidinium Lead Trihalide: A Broadly Tunable Perovskite for Efficient Planar Heterojunction Solar Cells. *Energy & Environmental Science*, 7:982, 2014.

[68] T. Erb, U. Zhokhavets, G. Gobsch, S. Raleva, B. Stühn, P. Schilinsky, C. Waldauf, C. J. Brabec, and b. T. Erb. Correlation between Structural and Optical Properties of Composite Polymer/Fullerene Films for Organic Solar Cells. *Advanced Functional Materials*, 15:1193–1196, 2005.

[69] L. Etgar, P. Gao, Z. Xue, Q. Peng, A. K. Chandiran, B. Liu, M. K. Nazeeruddin, and M. Grätzel. Mesoscopic $CH_3NH_3PbI_3/TiO_2$ Heterojunction Solar Cells. *Journal of the American Chemical Society*, 134:17396–9, 2012.

[70] D. Feldman, G. Barbose, R. Margolis, R. Wiser, N. Darghouth, and A. Goodrich. *Photovoltaic (PV) Pricing Trends: Historical, Recent, and Near-Term Projections*. 2012.

[71] K. Fesser, A. R. Bishop, and D. K. Campbell. Optical Absorption from Polarons in a Model of Polyacetylene. *Physical Review B*, 27:4804–4825, 1983.

[72] S. Few, J. M. Frost, and J. Nelson. Models of Charge Pair Generation in Organic Solar Cells. *Physical Chemistry Chemical Physics*, 17:2311–2325, 2014.

[73] S. R. Forrest. The Limits to Organic Photovoltaic Cell Efficiency. *MRS Bulletin*, 30:28–32, 2011.

[74] T. Förster. Zwischenmolekulare Energiewanderung Und Fluoreszenz. *Annalen Der Physik*, 437:55–75, 1948.

[75] T. Förster. 10th Spiers Memorial Lecture. Transfer Mechanisms of Electronic Excitation. *Discussions of the Faraday Society*, 27:7, 1959.

[76] T. Förster and T. Forster. Energiewanderung Und Fluoreszenz. *Naturwissenschaften*, 33:166, 1946.

[77] M. Fox. *Optical Properties of Solids*. Oxford University Press, Oxford, 2001.

[78] Fraunhoffer Institute for Solar Energy Systems. Photovoltaics Report. Technical report, 2012.

[79] F. Gao and O. Inganäs. Charge Generation in Polymer-Fullerene Bulk-heterojunction Solar Cells. *Physical Chemistry Chemical Physics*, 16:20291–304, 2014.

[80] S. Gélinas, O. Pare-Labrosse, C.-n. Brosseau, S. Albert-Seifried, C. R. McNeill, K. R. Kirov, I. A. Howard, R. Leonelli, R. H. Friend, and C. Silva. The Binding Energy of Charge-Transfer Excitons Localized at Polymeric Semiconductor Heterojunctions. *The Journal of Physical Chemistry C*, 115:7114–7119, 2011.

[81] S. Gélinas, A. Rao, A. Kumar, S. L. Smith, A. W. Chin, J. Clark, T. S. van der Poll, G. C. Bazan, and R. H. Friend. Ultrafast Long-Range Charge Separation in Organic Semiconductor Photovoltaic Diodes. *Science*, 343:512–516, 2014.

[82] A. Goetzberger and W. Greube. Solar Energy Conversion with Fluorescent Collectors. *Applied Physics*, 14:123–139, 1977.

[83] V. M. Goldschmidt. Krystallbau Und Chemische Zusammensetzung. *Berichte Der Deutschen Chemischen Gesellschaft (A and B Series)*, 60:1263–1296, 1927.

[84] I. Gonzalez-Valls and M. Lira-Cantu. Vertically-aligned Nanostructures of ZnO for Excitonic Solar Cells: A Review. *Energy & Environmental Science*, 2:19, 2009.

[85] G. Grancini, M. Maiuri, D. Fazzi, A. Petrozza, H.-J. Egelhaaf, D. Brida, G. Cerullo, and G. Lanzani. Hot Exciton Dissociation in Polymer Solar Cells. *Nature Materials*, 12:29–33, 2013.

[86] M. A. Green, K. Emery, Y. Hishikawa, W. Warta, and E. D. Dunlop. Solar Cell Efficiency Tables (Version 45). *Progress in Photovoltaics: Research and Applications*, 23:1–9, 2015.

[87] A. A. Y. Guilbert, L. X. Reynolds, A. Bruno, A. MacLachlan, S. P. King, M. A. Faist, E. Pires, J. E. Macdonald, N. Stingelin, S. A. Haque, and J. Nelson. Effect of Multiple Adduct Fullerenes on Microstructure and Phase Behavior of P3HT:Fullerene Blend Films for Organic Solar Cells. *ACS Nano*, 6:3868–3875, 2012.

[88] J. Guo, H. Ohkita, H. Benten, and S. Ito. Charge Generation and Recombination Dynamics in Poly(3-hexylthiophene)/Fullerene Blend Films with Different Regioregularities and Morphologies. *Journal of the American Chemical Society*, 132:6154–64, 2010.

[89] X. Guo, N. Zhou, S. J. Lou, J. Smith, D. B. Tice, J. W. Hennek, R. P. Ortiz, J. T. L. Navarrete, S. Li, J. Strzalka, L. X. Chen, R. P. H. Chang, A. Facchetti, and T. J. Marks. Polymer Solar Cells with Enhanced Fill Factors. *Nature Photonics*, 7:825–833, 2013.

[90] A. Haugeneder, M. Neges, C. Kallinger, W. Spirkl, U. Lemmer, J. Feldmann, U. Scherf, E. Harth, A. Gügel, and K. Müllen. Exciton Diffusion and Dissociation in Conjugated Polymer/Fullerene Blends and Heterostructures. *Physical Review B*, 59:15346–15351, 1999.

[91] H. Haus. Mode-locking of Lasers. *IEEE Journal of Selected Topics in Quantum Electronics*, 6:1173–1185, 2000.

[92] Z. He, C. Zhong, S. Su, M. Xu, H. Wu, and Y. Cao. Enhanced Power-conversion Efficiency in Polymer Solar Cells Using an Inverted Device Structure. *Nature Photonics*, 6:591–595, 2012.

[93] A. J. Heeger. 25th Anniversary Article: Bulk Heterojunction Solar Cells: Understanding the Mechanism of Operation. *Advanced Materials*, 26:10–27, 2014.

[94] A. J. Heeger, J. R. Schrieffer, and W. P. Su. Solitons in Conducting Polymers. *Reviews of Modern Physics*, 60:781–850, 1988.

[95] M. Helbig, A. Ruseckas, M.-L. Grage, E. Birckner, S. Rentsch, and V. Sundström. Resolving the Radical Cation Formation from the Lowest-Excited Singlet (S1) State of Terthiophene in a TiO_2SiO_2 Hybrid Polymer Matrix. *Chemical Physics Letters*, 302:587–594, 1999.

[96] C. Hellmann, F. Paquin, N. D. Treat, A. Bruno, L. X. Reynolds, S. A. Haque, P. N. Stavrinou, C. Silva, and N. Stingelin. Controlling the Interaction of Light with Polymer Semiconductors. *Advanced Materials*, 25:4906–11, 2013.

[97] E. Hennebicq, G. Pourtois, G. D. Scholes, L. M. Herz, D. M. Russell, C. Silva, S. Setayesh, A. C. Grimsdale, K. Müllen, J.-L. Brédas, and D. Beljonne. Exciton Migration in Rigid-rod Conjugated Polymers: An Improved Förster Model. *Journal of the American Chemical Society*, 127:4744–62, 2005.

[98] D. Holten, D. F. Bocian, and J. S. Lindsey. Probing Electronic Communication in Covalently Linked Multiporphyrin Arrays. A Guide to the Rational Design of Molecular Photonic Devices. *Accounts of Chemical Research*, 35:57–69, 2002.

[99] H. Hoppe and N. S. Sariciftci. Organic Solar Cells: An Overview. *Journal of Materials Research*, 19:1924–1945, 2011.

[100] H. Horiuchi, R. Katoh, K. Hara, M. Yanagida, S. Murata, H. Arakawa, and M. Tachiya. Electron Injection Efficiency from Excited N3 into Nanocrystalline ZnO Films: Effect of (N3-Zn^{2+}) Aggregate Formation. *The Journal of Physical Chemistry B*, 107:2570–2574, 2003.

[101] J.-S. Hsiao, B. P. Krueger, R. W. Wagner, T. E. Johnson, J. K. Delaney, D. C. Mauzerall, G. R. Fleming, J. S. Lindsey, D. F. Bocian, and R. J. Donohoe. Soluble Synthetic Multiporphyrin Arrays. 2. Photodynamics of Energy-Transfer Processes. *Journal of the American Chemical Society*, 118:11181–11193, 1996.

[102] C. A. Hunter and J. K. M. Sanders. The Nature of .pi.-.pi. Interactions. *Journal of the American Chemical Society*, 112:5525–5534, 1990.

[103] J.-H. Im, C.-R. Lee, J.-W. Lee, S.-W. Park, and N.-G. Park. 6.5% Efficient Perovskite Quantum-Dot-Sensitized Solar Cell. *Nanoscale*, 3:4088–93, 2011.

[104] H. Imahori, T. Umeyama, and S. Ito. Large Pi-aromatic Molecules as Potential Sensitizers for Highly Efficient Dye-sensitized Solar Cells. *Accounts of Chemical Research*, 42:1809–18, 2009.

[105] O. Inganäs, W. Salaneck, J.-E. Österholm, and J. Laakso. Thermochromic and Solvatochromic Effects in Poly(3-hexylthiophene). *Synthetic Metals*, 22: 395–406, 1988.

[106] International Energy Agency. *Key World Energy Statistics*. International Energy Agency, 2014.

[107] T. Ishihara. Optical Properties of PbI-based Perovskite Structures. *Journal of Luminescence*, 60-61:269–274, 1994.

[108] R. Jakubiak, C. J. Collison, W. C. Wan, L. J. Rothberg, and B. R. Hsieh. Aggregation Quenching of Luminescence in Electroluminescent Conjugated Polymers. *The Journal of Physical Chemistry A*, 103:2394–2398, 1999.

[109] L. Kador. Stochastic Theory of Inhomogeneous Spectroscopic Line Shapes Reinvestigated. *The Journal of Chemical Physics*, 95:5574, 1991.

[110] S. Karabunarliev and E. R. Bittner. Polaronexcitons and Electronvibrational Band Shapes in Conjugated Polymers. *The Journal of Chemical Physics*, 118: 4291, 2003.

[111] M. Kasha. Relation between Exciton Bands and Conduction Bands in Molecular Lamellar Systems. *Reviews of Modern Physics*, 31:162–169, 1959.

[112] M. Kasha. Energy Transfer Mechanisms and the Molecular Exciton Model for Molecular Aggregates. *Radiation Research*, 20:55, 1963.

[113] M. Kasha, H. R. Rawls, and M. Ashraf El-Bayoumi. The Exciton Model in Molecular Spectroscopy. *Pure and Applied Chemistry*, 11:371–392, 1965.

[114] A. M. Kendhale, A. P. H. J. Schenning, and M. G. Debije. Superior Alignment of Multi-chromophoric Perylenebisimides in Nematic Liquid Crystals and Their Application in Switchable Optical Waveguides. *Journal of Materials Chemistry A*, 1:229, 2013.

[115] A. L. T. Khan, P. Sreearunothai, L. M. Herz, M. J. Banach, and A. Köhler. Morphology-dependent Energy Transfer within Polyfluorene Thin Films. *Physical Review B*, 69:085201, 2004.

[116] H.-S. Kim, C.-R. Lee, J.-H. Im, K.-B. Lee, T. Moehl, A. Marchioro, S.-J. Moon, R. Humphry-Baker, J.-H. Yum, J. E. Moser, M. Grätzel, and N.-G. Park. Lead Iodide Perovskite Sensitized All-Solid-State Submicron Thin Film Mesoscopic Solar Cell with Efficiency Exceeding 9%. *Scientific Reports*, 2:591, 2012.

[117] Y. Kim, S. Cook, S. M. Tuladhar, S. A. Choulis, J. Nelson, J. R. Durrant, D. D. C. Bradley, M. Giles, I. McCulloch, C.-S. Ha, and M. Ree. A Strong

Regioregularity Effect in Self-organizing Conjugated Polymer Films and High-Efficiency Polythiophene:fullerene Solar Cells. *Nature Materials*, 5:197–203, 2006.

[118] M. Knupfer. Exciton Binding Energies in Organic Semiconductors. *Applied Physics A: Materials Science & Processing*, 77:623–626, 2003.

[119] T. M. Koh, K. Fu, Y. Fang, S. Chen, T. C. Sum, N. Mathews, S. G. Mhaisalkar, P. P. Boix, and T. Baikie. Formamidinium-Containing Metal-Halide: An Alternative Material for near-IR Absorption Perovskite Solar Cells. *The Journal of Physical Chemistry C*, 118:16458–16462, 2014.

[120] A. Köhler and H. Bässler. *Electronic Processes in Organic Semiconductors*. Wiley-VCH Verlag GmbH & Co. KGaA, 2015.

[121] A. Kojima, K. Teshima, Y. Shirai, and T. Miyasaka. Organometal Halide Perovskites as Visible-light Sensitizers for Photovoltaic Cells. *Journal of the American Chemical Society*, 131:6050–1, 2009.

[122] P. Kopola, T. Aernouts, R. Sliz, S. Guillerez, M. Ylikunnari, D. Cheyns, M. Välimäki, M. Tuomikoski, J. Hast, G. Jabbour, R. Myllylä, and A. Maaninen. Gravure Printed Flexible Organic Photovoltaic Modules. *Solar Energy Materials and Solar Cells*, 95:1344–1347, 2011.

[123] F. Krebs. *Polymeric Solar Cells: Materials, Design, Manufacture*. DEStech Publications, 2010.

[124] F. C. Krebs, M. Jø Rgensen, K. Norrman, O. Hagemann, J. Alstrup, T. D. Nielsen, J. Fyenbo, K. Larsen, and J. Kristensen. A Complete Process for Production of Flexible Large Area Polymer Solar Cells Entirely Using Screen Printing – First Public Demonstration. *Solar Energy Materials and Solar Cells*, 93:422–441, 2009.

[125] B. P. Krueger, G. D. Scholes, and G. R. Fleming. Calculation of Couplings and Energy-Transfer Pathways between the Pigments of LH2 by the Ab Initio Transition Density Cube Method. *The Journal of Physical Chemistry B*, 102: 5378–5386, 1998.

[126] J. R. Lakowicz. *Principles of Fluorescence Spectroscopy*. Springer-Verlag, 3rd edition, 2008.

[127] H. Langhals and A. Hofer. Chromophores Arranged as "Magnetic Meta Atoms": Building Blocks for Molecular Metamaterials. *The Journal of Organic Chemistry*, 78:5889–97, 2013.

[128] H. Langhals, S. Demmig, and H. Huber. Rotational Barriers in Perylene Fluorescent Dyes. *Spectrochimica Acta Part A: Molecular Spectroscopy*, 44:1189–1193, 1988.

[129] H. Langhals, A. J. Esterbauer, A. Walter, E. Riedle, and I. Pugliesi. Forster Resonant Energy Transfer in Orthogonally Arranged Chromophores. *Journal of the American Chemical Society*, 132:16777–82, 2010.

[130] J.-W. Lee, D.-J. Seol, a.-N. Cho, and N.-G. Park. High-Efficiency Perovskite Solar Cells Based on the Black Polymorph of $HC(NH_2)_2PbI_3$. *Advanced Materials*, 6:4991–4998, 2014.

[131] M. M. Lee, J. Teuscher, T. Miyasaka, T. N. Murakami, and H. J. Snaith. Efficient Hybrid Solar Cells Based on Meso-superstructured Organometal Halide Perovskites. *Science*, 338:643–7, 2012.

[132] S.-H. Lee, D.-H. Kim, J.-H. Kim, G.-S. Lee, and J.-G. Park. Effect of Metal-Reflection and Surface-Roughness Properties on Power-Conversion Efficiency for Polymer Photovoltaic Cells. *The Journal of Physical Chemistry C*, 113: 21915–21920, 2009.

[133] T. Leijtens, B. Lauber, G. E. Eperon, S. D. Stranks, and H. J. Snaith. The Importance of Perovskite Pore Filling in Organometal Mixed Halide Sensitized TiO_2-Based Solar Cells. *The Journal of Physical Chemistry Letters*, 5:1096–1102, 2014.

[134] A. Lemmerer and D. G. Billing. Synthesis, Characterization and Phase Transitions of the Inorganic-organic Layered Perovskite-type Hybrids $[(C_nH_{2n+1}NH_3)_2PbI_4]$, n = 7, 8, 9 and 10. *Dalton Transactions*, 41:1146–57, 2012.

[135] I. N. Levine and P. H. I. Learning. *Quantum Chemistry*. Pearson Prentice Hall, 2009.

[136] J. A. Levitt and W. H. Weber. Materials for Luminescent Greenhouse Solar Collectors. *Applied Optics*, 16:2684–2689, 1977.

[137] C. Li and H. Wonneberger. Perylene Imides for Organic Photovoltaics: Yesterday, Today, and Tomorrow. *Advanced Materials*, 24:613–36, 2012.

[138] Y. Liang, Z. Xu, J. Xia, S.-T. Tsai, Y. Wu, G. Li, C. Ray, and L. Yu. for the Bright Future - Bulk Heterojunction Polymer Solar Cells with Power Conversion Efficiency of 7.4%. *Advanced Materials*, 22:E135–E138, 2010.

[139] J. W. Lichtman and J.-A. Conchello. Fluorescence Microscopy. *Nature Methods*, 2:910–9, 2005.

[140] J. D. A. Lin, O. V. Mikhnenko, J. Chen, Z. Masri, A. Ruseckas, A. Mikhailovsky, R. P. Raab, J. Liu, P. W. M. Blom, M. A. Loi, C. J. García-Cervera, I. D. W. Samuel, and T.-Q. Nguyen. Systematic Study of Exciton Diffusion Length in Organic Semiconductors by Six Experimental Methods. *Materials Horizons*, 1: 280, 2014.

[141] S. Lin, W. Xiao, and W. Dietz. Generalized Förster-Dexter Theory of Photoinduced Intramolecular Energy Transfer. *Physical Review E*, 47:3698–3706, 1993.

[142] M. Lippitz, C. Hübner, T. Christ, H. Eichner, P. Bordat, A. Herrmann, K. Müllen, and T. Basché. Coherent Electronic Coupling Versus Localization in Individual Molecular Dimers. *Physical Review Letters*, 92:103001, 2004.

[143] C.-M. Liu, M.-S. Su, J.-M. Jiang, Y.-W. Su, C.-J. Su, C.-Y. Chen, C.-S. Tsao, and K.-H. Wei. Distribution of Crystalline Polymer and Fullerene Clusters in Both Horizontal and Vertical Directions of High-Efficiency Bulk Heterojunction Solar Cells. *ACS Applied Materials & Interfaces*, 5:5413–22, 2013.

[144] M. Loi, S. Toffanin, M. Muccini, M. Forster, U. Scherf, and M. Scharber. Charge Transfer Excitons in Bulk Heterojunctions of a Polyfluorene Copolymer and a Fullerene Derivative. *Advanced Functional Materials*, 17:2111–2116, 2007.

[145] A. Loiudice, A. Rizzo, G. Latini, C. Nobile, M. de Giorgi, and G. Gigli. Graded Vertical Phase Separation of Donor/Acceptor Species for Polymer Solar Cells. *Solar Energy Materials and Solar Cells*, 100:147–152, 2012.

[146] D. Magde, J. H. Brannon, T. L. Cremers, and J. Olmsted. Absolute Luminescence Yield of Cresyl Violet. A Standard for the Red. *The Journal of Physical Chemistry*, 83:696–699, 1979.

[147] L. Magnani, G. Rumbles, I. Samuel, K. Murray, S. Moratti, A. Holmes, and R. Friend. Photoluminescence Studies of Chain Interactions in Electroluminescent Polymers. *Synthetic Metals*, 84:899–900, 1997.

[148] N. Manfredi, B. Cecconi, and A. Abbotto. Multi-Branched Multi-Anchoring Metal-Free Dyes for Dye-Sensitized Solar Cells. *European Journal of Organic Chemistry*, 2014:7069–7086, 2014.

[149] D. E. Markov, E. Amsterdam, P. W. M. Blom, A. B. Sieval, and J. C. Hummelen. Accurate Measurement of the Exciton Diffusion Length in a Conjugated Polymer Using a Heterostructure with a Side-Chain Cross-Linked Fullerene Layer. *Journal of Physical Chemistry A*, 109:5266–5274, 2005.

[150] D. E. Markov, C. Tanase, P. W. M. Blom, and J. Wildeman. Simultaneous Enhancement of Charge Transport and Exciton Diffusion in Poly(p-phenylene Vinylene) Derivatives. *Physical Review B*, 72:45217, 2005.

[151] S. McDowall, B. L. Johnson, and D. L. Patrick. Simulations of Luminescent Solar Concentrators: Effects of Polarization and Fluorophore Alignment. *Journal of Applied Physics*, 108:053508, 2010.

[152] H. Meier, U. Stalmach, and H. Kolshorn. Effective Conjugation Length and UV/vis Spectra of Oligomers. *Acta Polymerica*, 48:379–384, 1997.

[153] M. Meier, S. Karg, K. Zuleeg, W. Brutting, and M. Schwoerer. Determination of Trapping Parameters in Poly(p-phenylenevinylene) Light-emitting Devices Using Thermally Stimulated Currents. *Journal of Applied Physics*, 84:87, 1998.

[154] R. Mens, S. Chambon, S. Bertho, G. Reggers, B. Ruttens, J. D'Haen, J. Manca, R. Carleer, D. Vanderzande, and P. Adriaensens. Description of the Nanostructured Morphology of [6,6]-phenyl-C61-butyric Acid Methyl Ester (PCBM) by

XRD, DSC and Solid-State NMR. *Magnetic Resonance in Chemistry*, 49:242–247, 2011.

[155] O. V. Mikhnenko, H. Azimi, M. Scharber, M. Morana, P. W. M. Blom, and M. A. Loi. Exciton Diffusion Length in Narrow Bandgap Polymers. *Energy & Environmental Science*, 5:6960, 2012.

[156] P. B. Miranda, D. Moses, and A. J. Heeger. Ultrafast Photogeneration of Charged Polarons in Conjugated Polymers. *Physical Review B*, 64:081201, 2001.

[157] A. Mishra, M. K. R. Fischer, and P. Bäuerle. Metal-free Organic Dyes for Dye-sensitized Solar Cells: from Structure: Property Relationships to Design Rules. *Angewandte Chemie (International Ed. In English)*, 48:2474–99, 2009.

[158] D. B. Mitzi and K. D. Karlin. *Synthesis, Structure, and Properties of Organic-Inorganic Perovskites and Related Materials*. John Wiley & Sons, 1999.

[159] A. C. Morteani, P. Sreearunothai, L. M. Herz, R. H. Friend, and C. Silva. Exciton Regeneration at Polymeric Semiconductor Heterojunctions. *Physical Review Letters*, 92:247402, 2004.

[160] D. Moses, A. Dogariu, and A. J. Heeger. Ultrafast Photoinduced Charge Generation in Conjugated Polymers. *Chemical Physics Letters*, 316:356–360, 2000.

[161] D. Moses, J. Wang, A. Heeger, N. Kirova, and S. Brazovski. Exciton Binding Energy in Poly(phenylene Vinylene). *Synthetic Metals*, 125:93–98, 2001.

[162] C. L. Mulder, P. D. Reusswig, A. M. Velázquez, H. Kim, C. Rotschild, and M. A. Baldo. Dye Alignment in Luminescent Solar Concentrators: I. Vertical Alignment for Improved Waveguide Coupling. *Optics Express*, 18 Suppl 1:A79–90, 2010.

[163] H. Najafov, B. Lee, Q. Zhou, L. C. Feldman, and V. Podzorov. Observation of Long-Range Exciton Diffusion in Highly Ordered Organic Semiconductors. *Nature Materials*, 9:938–43, 2010.

[164] P. Nalbach, I. Pugliesi, H. Langhals, and M. Thorwart. Noise-Induced Förster Resonant Energy Transfer between Orthogonal Dipoles in Photoexcited Molecules. *Physical Review Letters*, 108:218302, 2012.

[165] J. J. Nelson, T. J. Amick, and C. M. Elliott. Mass Transport of Polypyridyl Cobalt Complexes in Dye-Sensitized Solar Cells with Mesoporous TiO 2 Photoanodes. *The Journal of Physical Chemistry C*, 112:18255–18263, 2008.

[166] T.-Q. Nguyen. Control of Energy Transfer in Oriented Conjugated Polymer-Mesoporous Silica Composites. *Science*, 288:652–656, 2000.

[167] T.-Q. Nguyen, V. Doan, and B. J. Schwartz. Conjugated Polymer Aggregates in Solution: Control of Interchain Interactions. *The Journal of Chemical Physics*, 110:4068–4078, 1999.

[168] E. T. Niles, J. D. Roehling, H. Yamagata, A. J. Wise, F. C. Spano, A. J. Moulé, and J. K. Grey. J-Aggregate Behavior in Poly-3-hexylthiophene Nanofibers. *The Journal of Physical Chemistry Letters*, 3:259–263, 2012.

[169] A. F. Nogueira, C. Longo, and M.-A. de Paoli. Polymers in Dye Sensitized Solar Cells: Overview and Perspectives. *Coordination Chemistry Reviews*, 248: 1455–1468, 2004.

[170] H. Ohkita, S. Cook, Y. Astuti, W. Duffy, M. Heeney, S. Tierney, I. McCulloch, D. D. C. Bradley, and J. R. Durrant. Radical Ion Pair Mediated Triplet Formation in Polymer-Fullerene Blend Films. *Chemical Communications*, 100: 3939–41, 2006.

[171] H. Ohkita, S. Cook, Y. Astuti, W. Duffy, S. Tierney, W. Zhang, M. Heeney, I. McCulloch, J. Nelson, D. D. C. Bradley, and J. R. Durrant. Charge Carrier Formation in Polythiophene/Fullerene Blend Films Studied by Transient Absorption Spectroscopy. *Journal of the American Chemical Society*, 130:3030–42, 2008.

[172] B. O'Regan and M. Grätzel. A Low-cost, High-Efficiency Solar Cell Based on Dye-sensitized Colloidal TiO_2 Films. *Nature*, 353:737–740, 1991.

[173] F. Padinger, R. Rittberger, and N. Sariciftci. Effects of Postproduction Treatment on Plastic Solar Cells. *Advanced Functional Materials*, 13:85–88, 2003.

[174] P. Parkinson, C. Müller, N. Stingelin, M. B. Johnston, L. M. Herz, C. Muller, and M. Christian. Role of Ultrafast Torsional Relaxation in the Emission from

Polythiophene Aggregates. *The Journal of Physical Chemistry Letters*, 1:2788–2792, 2010.

[175] P. Parkinson, D. V. Kondratuk, C. Menelaou, J. Q. Gong, H. L. Anderson, and L. M. Herz. Chromophores in Molecular Nanorings: When is a Ring a Ring? *The Journal of Physical Chemistry Letters*, 5:4356–4361, 2014.

[176] C. M. Proctor, M. Kuik, and T.-Q. Nguyen. Charge Carrier Recombination in Organic Solar Cells. *Progress in Polymer Science*, 38:1941–1960, 2013.

[177] U. Rauscher, H. Bässler, D. D. C. Bradley, and M. Hennecke. Exciton Versus Band Description of the Absorption and Luminescence Spectra in Poly(P - phenylenevinylene). *Physical Review B*, 42:9830–9836, 1990.

[178] U. Rösch, S. Yao, R. Wortmann, and F. Würthner. Fluorescent H-aggregates of Merocyanine Dyes. *Angewandte Chemie (International Ed. In English)*, 45: 7026–30, 2006.

[179] S. Rühle, M. Shalom, and A. Zaban. Quantum-dot-sensitized Solar Cells. *Chemphyschem : A European Journal of Chemical Physics and Physical Chemistry*, 11:2290–304, 2010.

[180] A. Ruseckas, M. Theander, M. R. Andersson, M. Svensson, M. Prato, O. Inganäs, and V. Sundström. Ultrafast Photogeneration of Inter-chain Charge Pairs in Polythiophene Films. *Chemical Physics Letters*, 322:136–142, 2000.

[181] A. Ruseckas, E. B. Namdas, M. Theander, M. Svensson, A. Yartsev, D. Zigmantas, M. R. Andersson, O. Inganäs, and V. Sundström. Luminescence Quenching by Inter-chain Aggregates in Substituted Polythiophenes. *Journal of Photochemistry and Photobiology A: Chemistry*, 144:3–12, 2001.

[182] M. Sadrai, L. Hadel, R. R. Sauers, S. Husain, K. Krogh-Jespersen, J. D. Westbrook, and G. R. Bird. Lasing Action in a Family of Perylene Derivatives: Singlet Absorption and Emission Spectra, Triplet Absorption and Oxygen Quenching Constants, and Molecular Mechanics and Semiempirical Molecular Orbital Calculations. *The Journal of Physical Chemistry*, 96:7988–7996, 1992.

[183] N. S. Sariciftci, L. Smilowitz, A. J. Heeger, and F. Wudl. Photoinduced Electron Transfer from a Conducting Polymer to Buckminsterfullerene. *Science*, 258: 1474–6, 1992.

[184] M. C. Scharber, D. Mühlbacher, M. Koppe, P. Denk, C. Waldauf, A. J. Heeger, and C. J. Brabec. Design Rules for Donors in Bulk-Heterojunction Solar Cells – Towards 10 % Energy-Conversion Efficiency. *Advanced Materials*, 18:789–794, 2006.

[185] C. Scharsich, R. H. Lohwasser, M. Sommer, U. Asawapirom, U. Scherf, M. Thelakkat, D. Neher, and A. Köhler. Control of Aggregate Formation in Poly(3-hexylthiophene) by Solvent, Molecular Weight, and Synthetic Method. *Journal of Polymer Science Part B: Polymer Physics*, 50:442–453, 2012.

[186] M. Scheidler, U. Lemmer, R. Kersting, S. Karg, W. Riess, B. Cleve, R. F. Mahrt, H. Kurz, H. Bässler, E. O. Göbel, and P. Thomas. Monte Carlo Study of Picosecond Exciton Relaxation and Dissociation in Poly(phenylenevinylene). *Physical Review B*, 54:5536–5544, 1996.

[187] F. Schlosser, J. Sung, P. Kim, D. Kim, and F. Würthner. Excitation Energy Migration in Covalently Linked Perylene Bisimide Macrocycles. *Chemical Science*, 3:2778, 2012.

[188] S. A. Schmid, R. Abbel, A. P. H. Schenning, E. W. Meijer, R. P. Sijbesma, and L. M. Herz. Analyzing the Molecular Weight Distribution in Supramolecular Polymers. *Journal of the American Chemical Society*, 131:17696–704, 2009.

[189] G. D. Scholes. Long-Range Resonance Energy Transfer in Molecular Systems. *Annual Review of Physical Chemistry*, 54:57–87, 2003.

[190] G. D. Scholes and K. P. Ghiggino. Electronic Interactions and Interchromophore Excitation Transfer. *The Journal of Physical Chemistry*, 98:4580–4590, 1994.

[191] G. D. Scholes, K. P. Ghiggino, A. M. Oliver, and M. N. Paddon-Row. Intramolecular Electronic Energy Transfer between Rigidly Linked Naphthalene and Anthracene Chromophores. *The Journal of Physical Chemistry*, 97:11871–11876, 1993.

[192] T. Segal-Peretz, O. Leman, A. M. Nardes, and G. L. Frey. On the Origin of Charge Generation in Hybrid TiO_x/Conjugated Polymer Photovoltaic Devices. *The Journal of Physical Chemistry C*, 116:2024–2032, 2012.

[193] P. E. Shaw, A. Ruseckas, and I. D. W. Samuel. Exciton Diffusion Measurements in Poly(3-hexylthiophene). *Advanced Materials*, 20:3516–3520, 2008.

[194] M. B. Smith and J. Michl. Singlet Fission. *Chemical Reviews*, 110:6891–936, 2010.

[195] H. Snaith and L. Schmidt-Mende. Advances in Liquid-Electrolyte and Solid-State Dye-Sensitized Solar Cells. *Advanced Materials*, 19:3187–3200, 2007.

[196] F. C. Spano. The Spectral Signatures of Frenkel Polarons in H- and J-aggregates. *Accounts of Chemical Research*, 43:429–39, 2010.

[197] F. C. Spano and C. Silva. H- and J-aggregate Behavior in Polymeric Semiconductors. *Annual Review of Physical Chemistry*, 65:477–500, 2014.

[198] F. C. Spano, J. R. Kuklinski, and S. Mukamel. Cooperative Radiative Dynamics in Molecular Aggregates. *The Journal of Chemical Physics*, 94:7534, 1991.

[199] S. Speiser. Photophysics and Mechanisms of Intramolecular Electronic Energy Transfer in Bichromophoric Molecular Systems: Solution and Supersonic Jet Studies. *Chemical Reviews*, 96:1953–1976, 1996.

[200] D. Spoltore, W. D. Oosterbaan, S. Khelifi, J. N. Clifford, A. Viterisi, E. Palomares, M. Burgelman, L. Lutsen, D. Vanderzande, and J. Manca. Effect of Polymer Crystallinity in P3HT:PCBM Solar Cells on Band Gap Trap States and Apparent Recombination Order. *Advanced Energy Materials*, 3:466–471, 2013.

[201] G. I. Stegeman and R. A. Stegeman. *Nonlinear Optics: Phenomena, Materials and Devices*. John Wiley & Sons, 2012.

[202] C. C. Stoumpos, C. D. Malliakas, and M. G. Kanatzidis. Semiconducting Tin and Lead Iodide Perovskites with Organic Cations: Phase Transitions, High Mobilities, and near-infrared Photoluminescent Properties. *Inorganic Chemistry*, 52:9019–38, 2013.

[203] S. D. Stranks, G. E. Eperon, G. Grancini, C. Menelaou, M. J. P. Alcocer, T. Leijtens, L. M. Herz, A. Petrozza, and H. J. Snaith. Electron-hole Diffusion Lengths Exceeding 1 Micrometer in an Organometal Trihalide Perovskite Absorber. *Science*, 342:341–4, 2013.

[204] S. D. Stranks, V. M. Burlakov, T. Leijtens, J. M. Ball, A. Goriely, and H. J. Snaith. Recombination Kinetics in Organic-Inorganic Perovskites: Excitons, Free Charge, and Subgap States. *Physical Review Applied*, 2:034007, 2014.

[205] W. P. Su and J. R. Schrieffer. Soliton Dynamics in Polyacetylene. *Proceedings of the National Academy of Sciences*, 77:5626–5629, 1980.

[206] W. P. Su, J. R. Schrieffer, and A. J. Heeger. Solitons in Polyacetylene. *Physical Review Letters*, 42:1698–1701, 1979.

[207] T. C. Sum and N. Mathews. Advancements in Perovskite Solar Cells: Photophysics behind the Photovoltaics. *Energy & Environmental Science*, 7:2518–2534, 2014.

[208] S. Sun, T. Salim, N. Mathews, M. Duchamp, C. Boothroyd, G. Xing, T. C. Sum, and Y. M. Lam. The Origin of High Efficiency in Low-temperature Solution-processable Bilayer Organometal Halide Hybrid Solar Cells. *Energy & Environmental Science*, 7:399, 2014.

[209] V. Sundstrom and T. Gillbro. Excited State Dynamics and Photophysics of Aggregated Dye Chromophores in Solution. *The Journal of Chemical Physics*, 83:2733, 1985.

[210] O. Svelto. *Principles of Lasers*. Springer US, 2010.

[211] A. Szabo and N. S. Ostlund. *Modern Quantum Chemistry: Introduction to Advanced Electronic Structure Theory*. Dover Publications, 2012.

[212] K. Tanaka, T. Takahashi, T. Ban, T. Kondo, K. Uchida, and N. Miura. Comparative Study on the Excitons in Lead-halide-based Perovskite-type Crystals $CH_3NH_3PbBr_3$ $CH_3NH_3PbI_3$. *Solid State Communications*, 127:619–623, 2003.

[213] C. W. Tang. Two-layer Organic Photovoltaic Cell. *Applied Physics Letters*, 48: 183–185, 1986.

[214] J. ter Schiphorst, A. M. Kendhale, M. G. Debije, C. Menelaou, L. M. Herz, and A. P. H. J. Schenning. Dichroic Perylene Bisimide Triad Displaying Energy Transfer in Switchable Luminescent Solar Concentrators. *Chemistry of Materials*, 26:3876–3878, 2014.

[215] J. R. Tumbleston, A. C. Stuart, E. Gann, W. You, and H. Ade. Fluorinated Polymer Yields High Organic Solar Cell Performance for a Wide Range of Morphologies. *Advanced Functional Materials*, 23:3463–3470, 2013.

[216] T. Umebayashi, K. Asai, T. Kondo, and A. Nakao. Electronic Structures of Lead Iodide Based Low-dimensional Crystals. *Physical Review B*, 67:155405, 2003.

[217] United Nations Framework Convention on Climate Change. Decision 1/CP.16, Paragraph 4. 2010.

[218] M. Urbani, M. Grätzel, M. K. Nazeeruddin, and T. Torres. Meso-Substituted Porphyrins for Dye-Sensitized Solar Cells. *Chemical Reviews*, 114:12330–12396, 2014.

[219] B. Valeur and M. N. Berberan-Santos. *Molecular Fluorescence: Principles and Applications*. John Wiley & Sons, 2012.

[220] M. Valiev, E. Bylaska, N. Govind, K. Kowalski, T. Straatsma, H. Van Dam, D. Wang, J. Nieplocha, E. Apra, T. Windus, and W. de Jong. NWChem: A Comprehensive and Scalable Open-source Solution for Large Scale Molecular Simulations. *Computer Physics Communications*, 181:1477–1489, 2010.

[221] K. Vandewal, S. Albrecht, E. T. Hoke, K. R. Graham, J. Widmer, J. D. Douglas, M. Schubert, W. R. Mateker, J. T. Bloking, G. F. Burkhard, A. Sellinger, J. M. J. Fréchet, A. Amassian, M. K. Riede, M. D. McGehee, D. Neher, and A. Salleo. Efficient Charge Generation by Relaxed Charge-transfer States at Organic Interfaces. *Nature Materials*, 13:63–8, 2014.

[222] P. P. C. Verbunt, A. Kaiser, K. Hermans, C. W. M. Bastiaansen, D. J. Broer, and M. G. Debije. Controlling Light Emission in Luminescent Solar Concentrators through Use of Dye Molecules Aligned in a Planar Manner by Liquid Crystals. *Advanced Functional Materials*, 19:2714–2719, 2009.

[223] S. Verma, A. Ghosh, A. Das, and H. N. Ghosh. Ultrafast Exciton Dynamics of J- and H-aggregates of the Porphyrin-catechol in Aqueous Solution. *The Journal of Physical Chemistry B*, 114:8327–34, 2010.

[224] E. Wang, J. Bergqvist, K. Vandewal, Z. Ma, L. Hou, A. Lundin, S. Himmelberger, A. Salleo, C. Müller, O. Inganäs, F. Zhang, and M. R. Andersson. Conformational Disorder Enhances Solubility and Photovoltaic Performance of a Thiophene-Quinoxaline Copolymer. *Advanced Energy Materials*, 3:806–814, 2013.

[225] J. Wang, E. Yang, J. R. Diers, D. M. Niedzwiedzki, C. Kirmaier, D. F. Bocian, J. S. Lindsey, and D. Holten. Distinct Photophysical and Electronic Characteristics of Strongly Coupled Dyads Containing a Perylene Accessory Pigment and a Porphyrin, Chlorin, or Bacteriochlorin. *The Journal of Physical Chemistry B*, 117:9288–304, 2013.

[226] J. T.-w. Wang, J. M. Ball, E. M. Barea, A. Abate, J. A. Alexander-Webber, J. Huang, M. Saliba, I. Mora-Sero, J. Bisquert, H. J. Snaith, and R. J. Nicholas. Low-temperature Processed Electron Collection Layers of Graphene/TiO_2 Nanocomposites in Thin Film Perovskite Solar Cells. *Nano Letters*, 14:724–30, 2014.

[227] W. H. Weber and J. Lambe. Luminescent Greenhouse Collector for Solar Radiation. *Applied Optics*, 15:2299–2300, 1976.

[228] C. Wehrenfennig, G. E. Eperon, M. B. Johnston, H. J. Snaith, and L. M. Herz. High Charge Carrier Mobilities and Lifetimes in Organolead Trihalide Perovskites. *Advanced Materials*, 26:1584–1589, 2014.

[229] S. Westenhoff, C. Daniel, R. H. Friend, C. Silva, V. Sundström, and A. Yartsev. Exciton Migration in a Polythiophene: Probing the Spatial and Energy Domain by Line-dipole Forster-type Energy Transfer. *The Journal of Chemical Physics*, 122:094903, 2005.

[230] K. Wojciechowski, M. Saliba, T. Leijtens, A. Abate, and H. J. Snaith. Sub-150°C Processed Meso-superstructured Perovskite Solar Cells with Enhanced Efficiency. *Energy & Environmental Science*, 7:1142, 2014.

[231] C. H. Woo, B. C. Thompson, B. J. Kim, M. F. Toney, and J. M. J. Fréchet. The Influence of Poly(3-hexylthiophene) Regioregularity on Fullerene-Composite Solar Cell Performance. *Journal of the American Chemical Society*, 130:16324–16329, 2008.

[232] J. Wu, Z. Lan, J. Lin, M. Huang, Y. Huang, L. Fan, and G. Luo. Electrolytes in Dye-Sensitized Solar Cells. *Chemical Reviews*, 115:2136–2173, 2015.

[233] Y. Yamada, T. Nakamura, M. Endo, A. Wakamiya, and Y. Kanemitsu. Photocarrier Recombination Dynamics in Perovskite $CH_3NH_3PbI_3$ for Solar Cell Applications. *Journal of the American Chemical Society*, 136:11610–3, 2014.

[234] H. Yamagata and F. C. Spano. Interplay between Intrachain and Interchain Interactions in Semiconducting Polymer Assemblies: The HJ-aggregate Model. *The Journal of Chemical Physics*, 136:184901, 2012.

[235] M. Yan, L. J. Rothberg, F. Papadimitrakopoulos, M. E. Galvin, and T. M. Miller. Defect Quenching of Conjugated Polymer Luminescence. *Physical Review Letters*, 73:744–747, 1994.

[236] M. Yan, L. J. Rothberg, E. W. Kwock, and T. M. Miller. Interchain Excitations in Conjugated Polymers. *Physical Review Letters*, 75:1992–1995, 1995.

[237] E. Yang, J. Wang, J. R. Diers, D. M. Niedzwiedzki, C. Kirmaier, D. F. Bocian, J. S. Lindsey, and D. Holten. Probing Electronic Communication for Efficient Light-harvesting Functionality: Dyads Containing a Common Perylene and a Porphyrin, Chlorin, or Bacteriochlorin. *The Journal of Physical Chemistry B*, 118:1630–1647, 2014.

[238] Y. Yang, Q. Pei, and A. Heeger. Efficient Blue Light-emitting Diodes from a Soluble Poly (para-phenylene) Internal Field Emission Measurement of the Energy Gap in Semiconducting Polymers. *Synthetic Metals*, 78:263–267, 1996.

[239] A. Yella, C.-L. Mai, S. M. Zakeeruddin, S.-N. Chang, C.-H. Hsieh, C.-Y. Yeh, and M. Grätzel. Molecular Engineering of Push-Pull Porphyrin Dyes for Highly Efficient Dye-Sensitized Solar Cells: The Role of Benzene Spacers. *Angewandte Chemie*, 126:3017–3021, 2014.

[240] G. Yu, J. Gao, J. C. Hummelen, F. Wudl, and A. J. Heeger. Polymer Photovoltaic Cells: Enhanced Efficiencies Via a Network of Internal Donor-Acceptor Heterojunctions. *Science*, 270:1789–1791, 1995.

[241] S. M. Zakeeruddin and M. Grätzel. Solvent-Free Ionic Liquid Electrolytes for Mesoscopic Dye-Sensitized Solar Cells. *Advanced Functional Materials*, 19: 2187–2202, 2009.

[242] Q. Zhang and G. Cao. Nanostructured Photoelectrodes for Dye-sensitized Solar Cells. *Nano Today*, 6:91–109, 2011.

[243] Q. Zhang, C. S. Dandeneau, X. Zhou, and G. Cao. ZnO Nanostructures for Dye-Sensitized Solar Cells. *Advanced Materials*, 21:4087–4108, 2009.

[244] Y. Zhang, H.-L. Yip, O. Acton, S. K. Hau, F. Huang, and A. K.-Y. Jen. A Simple and Effective Way of Achieving Highly Efficient and Thermally Stable Bulk-Heterojunction Polymer Solar Cells Using Amorphous Fullerene Derivatives as Electron Acceptor. *Chemistry of Materials*, 21:2598–2600, 2009.

[245] Y. Zhang, M. Liu, G. E. Eperon, T. Leijtens, D. P. McMeekin, M. Saliba, W. Zhang, M. de Bastiani, A. Petrozza, L. Herz, M. B. Johnston, H. Lin, and H. Snaith. Charge Selective Contacts, Mobile Ions and Anomalous Hysteresis in Organic-Inorganic Perovskite Solar Cells. *Materials Horizons*, 2:315–322, 2015.

[246] H. Zhou, L. Yang, S. Stoneking, and W. You. A Weak Donor–Strong Acceptor Strategy to Design Ideal Polymers for Organic Solar Cells. *ACS Applied Materials & Interfaces*, 2:1377–1383, 2010.

[247] H. Zhou, Y. Zhang, J. Seifter, S. D. Collins, C. Luo, G. C. Bazan, T.-Q. Nguyen, and A. J. Heeger. High-Efficiency Polymer Solar Cells Enhanced by Solvent Treatment. *Advanced Materials*, 25:1646–52, 2013.

[248] H. Zhou, Q. Chen, G. Li, S. Luo, T.-b. Song, H.-S. Duan, Z. Hong, J. You, Y. Liu, and Y. Yang. Interface Engineering of Highly Efficient Perovskite Solar Cells. *Science*, 345:542–546, 2014.